ISSN: 1977-5296

ESARDA

European Safeguards Research & Development Association

50TH ANNIVERSARY

The International Journal of Nuclear Safeguards and Non-Proliferation

June 2019 · Bulletin No.58

ISSN: 1977-5296

Number 58
June 2019

European Commission, Joint Research Centre,
Directorate G - Nuclear Safety and Security
Nuclear Security Unit G.II.7
T.P. 800, I-21027 Ispra (VA), Italy
Tel. +39 0332-786182
EC-ESARDA-BULLETIN@ec.europa.eu

ESARDA is an association formed to advance and harmonize research and development for safeguards. The Parties to the association are:

ATI, Austria; CEA, France; CNCAN, Romania; CTE, France; EDF, France; ENEA, Italy; ETC Ltd, Germany; European Commission; FANC, Belgium; FZJ, Germany; HAEA, Hungary; HIP, Finland; IKI, Hungary; IRSN, France; MINETUR, Spain; NNL, UK; NRG, The Netherlands; NRI, Czech Republic; ONR, UK; ORANO, France; PAA, Poland; SCK/CEN, Belgium; Sellafield Ltd, UK; SIEPS, France; SSM, Sweden; STUK, Finland; SUJB, Czech Republic; UKAEA, UK; University of Hamburg, Germany; University of Liege, Belgium; University of Uppsala, Sweden; URENCO, Germany; VATESI, Lithuania; WKK, Germany.

Scientific and technical papers submitted are reviewed by independent authors including members of the Editorial Committee.

Manuscripts are to be sent to the Editor (EC-ESARDA-BULLETIN@ec.europa.eu) following the 'instructions for authors' available on https://esarda.jrc.ec.europa.eu/ where the bulletins can also be viewed and downloaded.

Accepted manuscripts are published free of charge.

N.B. Articles and other material in the ESARDA Bulletin do not necessarily present the views or policies of neither ESARDA nor the European Commission.

ESARDA Bulletin is published jointly by ESARDA and the Joint Research Centre of the European Commission and distributed free of charge to over 1000 registered members, libraries and institutions Worldwide.

Cover designed by Chris Havenga, (EC, JRC, G.II.7, Italy)

Printed by
Bietlot in Belgium

ESARDA
European Safeguards Research and Development Association

Bulletin

Table of Content Issue n° 58

Editorial

Peer Reviewed Articles

Editorial

Elena Stringa

Dear readers,

I am very pleased to provide you with the 58th edition of the ESARDA Bulletin.

As this year marks the 50th anniversary of ESARDA, the Editorial Committee has dedicated the cover of the journal to this important event. Nevertheless, the new cover layout is not the only novelty introduced by the Editorial Committee. In order to stimulate the scientific debate and encourage the information exchange in the ESARDA community, we have also introduced a journal subtitle to emphasize the scientific essence of our publication: *The International Journal of Nuclear Safeguards and Non-Proliferation*.

The ESARDA Bulletin was born in October 1981 as a bulletin dispatching news about ESARDA working group activities and presenting Safeguards relevant technical articles. In time, the section related to articles expanded in quantity and quality, and from February 2006, with the Issue 33, the ESARDA Bulletin contains a section dedicated to scientific peer-reviewed articles. The ESARDA Bulletin content continued to evolve according to the needs of the ESARDA community and the peer-reviewed articles section expanded more and more. Currently, the Bulletin is entirely dedicated to the publication of scientific-peer reviewed articles and has become the scientific journal of ESARDA. Because of that, in January 2019, the Editor, on behalf of the Editorial Committee, has resubmitted to Scopus its request for indexation in their academic database of publications: we should have an answer by the end of the year.

In ESARDA, it is also important that all the members are updated on ESARDA Working group progresses and on news relating to Safeguards and Non-proliferation tools and trainings that cannot be described in a scientific article. The Editorial Committee has then setup a new online publication that aims at reporting news from the ESARDA working groups and technical papers that are relevant for the ESARDA community. The first Issue of the new ESARDA publication is expected for September 2019 and issues will be released every 6 months: in the due time the ESARDA web site will host a section dedicated to the new publication.

On April 1-5, 2019 the Joint Research Centre hosted the 18th edition of the ESARDA Course on Nuclear Safeguards and Non-Proliferation. The course was successfully attended by 50 enthusiastic participants from Europe, America, Asia and Africa. People interested in participating to the 19th ESARDA course, foreseen in spring 2020, is invited to visit the dedicated section in the ESARDA website that will be updated after the summer break.

On May 14-16, 2019 the 41st ESARDA Annual Meeting Symposium on Safeguards and Nuclear Material Management, has been held at the Regina Palace Hotel in Stresa, preceded by the ESARDA working groups meetings. The Symposium, based on about 150 scientific, technical and strategic presentations, was a big success followed by more than 250 participants from all over the world. The proceedings will be published soon in the dedicated section of the ESARDA website.

On behalf of the Editorial Committee, I would like to thank authors and reviewers for the time and energy they have dedicated to write, review and improve the published scientific works, allowing the publishing in the current Bulletin of high quality articles that are of great interest to ESARDA.

I encourage researchers to submit their work any time so that all the ESARDA community can benefit from the latest relevant research novelties. In order to submit a contribution you are kindly asked to follow the instructions reported in the bulletin section of the ESARDA web site at https://esarda.jrc.ec.europa.eu.

Moreover, I would like to encourage volunteering as potential reviewer by sending an e-mail to EC-ESARDA-BULLETIN@ec.europa.eu, specifying one's area of expertise among the following:

- Non-destructive analysis
- Destructive analysis
- Arms control and Nuclear Disarmament Verification
- Geological repositories
- Spent Fuel Verification and Spent Fuel Transfer
- Containment & Surveillance
- Process Monitoring
- Statistical Methodologies
- Implementation of Safeguards
- Safeguards Methodologies
- Nuclear Security
- Export control and Non-Proliferation

I also encourage you to cite works published in the ESARDA Bulletin, in order to increase the visibility and interest on ESARDA activities.

As always, on behalf of the Editorial Committee, I conclude this editorial addressing sincere thanks to Andrea De Luca, web master and essential assistant for the ESARDA publications preparation: thank you very much for your engagement and enthusiasm, for the pertinent suggestions and fruitful ideas in supporting the dissemination of knowledge in the ESARDA community.

Dr. Elena Stringa
Editor of the ESARDA Bulletin - The International Journal of Non-Proliferation and Nuclear Safeguards

https://esarda.jrc.ec.europa.eu/
ec-esarda-bulletin@ec.europa.eu
Elena.Stringa@.ec.europa.eu

Optimal Sampling Plans for Inventory Verification of Spent Fuel Ponds

Thomas Krieger[1], Katharina Aymanns[1], Arnold Rezniczek[2], Irmgard Niemeyer[1]

[1]Forschungszentrum Jülich GmbH, IEK-6, 52425 Jülich, Germany
[2]UBA GmbH, 52134 Herzogenrath, Germany
E-mail: t.krieger@fz-juelich.de, k.aymanns@fz-juelich.de, Rezniczek@uba-gmbh.de, i.niemeyer@fz-juelich.de

Abstract:

Spent fuel unloaded from the reactor core of Light Water Reactors is usually stored in the spent fuel pond of the reactor. The IAEA and EURATOM have a number of different instruments in their verification instrument portfolios to verify spent fuel assemblies in the spent fuel pond. Depending on the situation, e.g., the type of the different fuel assemblies' strata and the accessibility for future re-verification, different requirements for the verification exist.

Once spent fuel has been loaded into dry storage casks for transport and intermediate storage, it becomes difficult-to-access. The IAEA requires that nuclear material prior to its becoming difficult-to-access must be verified using sampling plans that provide a high detection probability for a possible diversion of nuclear material from the spent fuel assemblies.

The paper discusses how to set up optimal sampling plans depending on the verification instruments, the assumed detection capabilities of these verification instruments, and the presumed diversion strategies.

Keywords: sampling plans; detection probability; inventory verification; spent fuel ponds; difficult-to-access;

1. Introduction

Spent fuel assemblies (SFAs) from Light Water Reactors (LWRs) are usually stored in the spent fuel pond of the reactor. Typically, physical inventory verification (PIV), interim inspections or inspections to verify the transfers of spent fuel to dry storage, where the spent fuel is no longer accessible for verification, are carried out. As especially the verification of spent fuel prior to transfers to dry storage require a high detection probability (DP) for possible diversions and therefore also a substantial amount of inspection effort, IAEA and EURATOM aim to optimize the effectiveness and efficiency of these verifications.

The IAEA and EURATOM have a set of instruments that can be used for the verification of spent fuel assemblies. In this paper we focus on the following three instruments: The Improved Cerenkov Viewing Device (ICVD), the Digital Cerenkov Viewing Device (DCVD), and the Passive Gamma Emission Tomography System (PGET). Each of these verification instruments has an associated detection capability and specific time to perform a measurement. Depending on different diversion assumptions and nuclear material strata, optimal sampling plans can be set up based on the different characteristics of the verification instruments.

The paper is structured as follows: Section 2 introduces the verification instruments together with their detection capabilities and the types of LWR assemblies considered in this paper. Also, the estimated net measurement time to carry out the measurements for an experienced and inexperienced inspector for any of the three instruments is given. Section 3 deals with the probabilistic aspects for finding optimal sampling plans where approaches from [1], [2] and [3] are modified and tailored to the situation discussed here. In section 4 optimal sampling plans are determined for four examples where two types of LWR assemblies and two different required detection probabilities are assumed. Section 5 deals with non-equal diversion scenarios which are usually not addressed in common safeguards literature. It is shown that the achieved DP depends on the order the sampling is performed. In section 6 the case of two classes of SFAs in one spent fuel pond is treated and issues in finding optimal sampling plans are discussed. Section 7 contains the derivations of the DP formula and section 8 points to future research activities and gives an outlook.

2. Instruments for verification of spent fuel assemblies

In this paper we assume that the inventory of the spent fuel pond does not increase, which would be, e.g., the case after the final shutdown of the reactor. In this situation we consider applying the ICVD, the DCVD or the PGET to verify the content of the spent fuel pond. This section describes briefly the function and use of the three measurement instruments.

2.1 ICVD and DCVD

Both the ICVD and DCVD are inspector tools imaging the Cerenkov light emitted from irradiated nuclear fuel assemblies in spent fuel ponds as described in [4], [5], [6].

The ICVD and DCVD systems have been approved by the IAEA for gross defect verification in order to verify the presence of spent fuel. They both observe the Cerenkov light glow from above a storage pool. They are optimized for ultraviolet radiation and are capable of operating with facility lights turned on. When aligned vertically above the tops of fuel assemblies the verification instruments can distinguish irradiated fuel items from non-fuel items.

The ICVD is used for the qualitative verification (Yes/No decision) of irradiated nuclear fuel stored under water. It allows the inspectors to conclude that the observed object is an irradiated fuel assembly. ICVD does not allow recording the measurement results for further investigation. In case of inconclusiveness of the measurement results the measurement has to be repeated on-site.

The DCVD is further approved by the IAEA to detect partial defects. The camera is connected to a computer that uses specialized software to analyse the image. To carry out the measurements of SFAs stored in a pond the DCVD has to be placed at the fuel assembly-loading machine. Based on experiences a DCVD measurement campaign of spent fuel assemblies stored underwater may take up to one week depending on the number of SFAs to be verified.

In general, ICVD and DCVD have a minor impairment on the facility operation as there is no need for fuel movement or contact of the instrument with the potentially contaminated water of the spent fuel pond.

2.2 PGET

The PGET is approved by the IAEA for verification of spent nuclear fuel assemblies stored under water; see [7]. Fission products contained in SFAs emit gamma radiation, which is detected by two collimated CdZnTe detectors. The PGET system is assembled on a rotary baseplate inside a watertight torus shaped enclosure. To carry out the verification measurements the system is positioned under water on the top of an empty rack or on a special tripod on the bottom of the pond. In a next step a SFA is moved and placed in the center of the enclosure and held stationary to perform a measurement. Thus, compared to the ICVD and DCVD additional time to place the SFA in the PGET is needed.

2.3 LWR assemblies and detection capabilities of ICVD, DCVD and PGET

This paper considers two different types of LWR spent fuel such as fuel assemblies from pressurized water reactors (PWR) and boiling water reactors (BWR); see, e.g., [8]. PWRs are operated with fuel assemblies based on a square lattice arrangement characterized by the number of rods they contain, typically, 17 × 17 in current designs with for example 250 fuel pins per assembly. BWRs also use fuel assemblies, which are designed as a square lattice, with rods geometries ranging from 6 × 6 to 10 × 10 containing for example 96 fuel pins.

Each of the three verification measurement instruments has an associated detection capability: What is the probability (the so-called identification probability $p_{instrument}$) that the instrument will identify a falsified SFA as falsified, if a certain percentage of material has been removed from the SFA (defect size)? According to [9], the identification probabilities can be assumed to be step functions taking values zero and one:

$$\begin{aligned} p_{ICVD} &= \begin{cases} 1 & \textit{if } 100\% \textit{ of the pins have been removed} \\ 0 & \textit{otherwise} \end{cases} \\ p_{DCVD} &= \begin{cases} 1 & \textit{if } 30\% \textit{ of the pins or more have been removed} \\ 0 & \textit{otherwise} \end{cases} \\ p_{PGET} &= \begin{cases} 1 & \textit{if } 0.38\% \textit{ of the pins or more have been removed} \\ 0 & \textit{otherwise} \end{cases} \end{aligned} \quad (1)$$

Six comments: First, the identification probabilities in Eq. (1) are based on field trials on multiple fuel types for a range of burnups, cooling times, and number of SFAs measured; see [9]. Second, Eq. (1) indicates that the measurement errors are not normally distributed, as it is usually assumed; see [3]. Third, more complex identification probabilities than in Eq. (1) could be considered if needed. The approach in this paper, however, would have to be modified. Fourth, Eq. (1) quantifies for our purposes the terms gross, partial and bias defect which are usually defined only qualitatively; see 10.7 in [6]. Fifth, because most of the modern LWR assembly designs allow for the exchange of single fuel pins for defective rods, Eq. (1) covers the diversion of single pins. Sixth, a replacement of pins with dummy pins, which contain material leading to a similar signal as a spent fuel pin, is not considered in this paper.

Estimates of the net measurement time for one SFA for any of the three instruments are listed in Table 1, based on personal communication [10]. Note that the set-up time for all three instruments is equal concerning the positioning of the fuel element handling machine; in addition, PGET requires 2 more minutes for the SFA placement.

	ICVD	DCVD	PGET
experienced inspector	3 seconds	1 minute	5 minutes measurement plus 2 minutes placement procedure of the SFA into the PGET
inexperienced inspector	7 seconds	2 minute	

Table 1: Estimated net measurement times for an experience/inexperienced inspector for the three instruments.

Recent experiences show, that the DCVD net measurement time of an experienced inspector is about 2 minutes per SFA instead of 1 minute depending, e.g., on the quality of water, the pond conditions, the light-contrast of the image, and the burnup of the SFAs.

3. One class of SFAs: The detection probability

This section deals with the probabilistic aspects for finding optimal sampling plans, where approaches from [1], [2] and [3] are modified and tailored to the situation discussed here.

Let N be the number of SFAs in the spent fuel pond, L be the number of fuel pins per SFA, $\bar{x}_{Pu}$ be the average amount of plutonium (Pu) per SFA, and SQ be the significant quantity (SQ = 8 [kg] for Pu), i.e. "the approximate amount of nuclear material for which the possibility of manufacturing a nuclear explosive device cannot be excluded."; see 3.14 in [6]. We focus in this paper on the diversion of Pu, because it should be more attractive to a diverter than low enriched uranium, as low enriched uranium 1) requires additional enrichment to become weapon usable material and 2) the number of fuel pins to be removed to get a significant quantity of 75 [kg] is usually much higher compared to acquiring a significant quantity of 8 [kg] for Pu.

IAEA sampling plans are usually based on the equal diversion hypothesis (see [3]) which means that each falsified item is falsified by the same amount of nuclear material. In the context discussed here, this hypothesis means that the diverter removes r_{pin} pins from a certain number of SFAs (items). For example: 10 pins are removed from 20 SFAs, but not: 4 pins are removed from 21 SFAs and 30 pins from 10 SFAs (see section 5). The number r_{pin} ranges from the smallest possible number of removed pins r_{min} (defined below) up to the maximum number of removed pins L.

How many SFAs have to be falsified if r_{pin} pins are removed from each of them? Because the diverter wants to acquire one significant quantity (1 SQ), r_{pin} and the respective number of falsified SFAs $r_{SFA} = r_{SFA}\left(r_{pin}\right)$ have to fulfil the inequality

$$\frac{\bar{x}_{Pu}}{L} \times r_{pin} \times r_{SFA}\left(r_{pin}\right) \geq SQ,$$

which yields, assuming that the diverter will not falsify more SFAs than necessary,

$$r_{SFA}\left(r_{pin}\right) = \left\lceil \frac{SQ \times L}{\bar{x}_{Pu}} \frac{1}{r_{pin}} \right\rceil, \qquad (2)$$

where the ceiling $\lceil a \rceil$ of a real number a is the smallest integer not less than a. Because the number of falsified SFAs must be smaller or equal than the total number of SFAs of the spent fuel pond, i.e. $r_{SFA}\left(r_{pin}\right) \leq N$ for all admissible r_{pin}, the minimum number of removed pins r_{min} is, using Eq. (2), the smallest integer fulfilling $\left\lceil SQ \times L / \bar{x}_{Pu} / r_{min} \right\rceil \leq N$, i.e.

$$r_{min} = \left\lceil \frac{SQ \times L}{N \bar{x}_{Pu}} \right\rceil.$$

Because it is assumed that the diverter can acquire 1 SQ from the SFAs in the spent fuel pond, we must have $SQ \leq N\bar{x}_{Pu}$, which yields, using Eq. (2), $r_{SFA}(L) = \left\lceil SQ / \bar{x}_{Pu} \right\rceil \leq \lceil N \rceil = N$, i.e. the existence of r_{min} can be assured. Therefore, the set of diversion strategies is assumed to be

$$X := \{r_{min}, r_{min}+1, \ldots, L\}, \qquad (3)$$

and $r_{SFA}\left(r_{pin}\right)$ according to Eq. (2) defines for any $r_{pin} \in X$ the number of falsified SFAs. Eq. (2) is illustrated in Table 2 for L = 96, $\bar{x}_{Pu} = 2$ [kg] and SQ = 8 [kg] yielding r_{min} = 1 if $N \geq 384$.

Table 2 illustrates two effects: First, different r_{pin} values may lead to the same number of falsified SFAs. Thus, a rational diverter removes 1, 2, …, 23, 24, 26, 28, 30, 32, 35, 39, 43, 48, 55, 64, 77 or 96 pins, or in general:

$$\widetilde{X} := \left\{ \begin{matrix} r_{pin} \in X : r_{SFA}\left(r_{pin}-1\right) > r_{SFA}\left(r_{pin}\right) \\ for\ all \quad r_{pin} = r_{min}+1 \ldots, L \end{matrix} \right\}.$$

Because of the properties of the DP as a function of r_{pin} (see below), only the three values $r_{pin} \in \{\lceil 0.3L \rceil - 1,\ L-1, L\}$ need to be considered for finding an appropriate

r_{pin}	1	2	3	4	5	6	7	8	9	10	11	12	13	14
$r_{SFA}\left(r_{pin}\right)$	384	192	128	96	77	64	55	48	43	39	35	32	30	28

15	16	17	18	19	20	21	22	23	24,25	26,27	28,29	30,31	32,33,34
26	24	23	22	21	20	19	18	17	16	15	14	13	12

35…38	39…42	43…47	48…54	55…63	64…76	77…95	96
11	10	9	8	7	6	5	4

Table 2: Pairs $\left(r_{pin}, r_{SFA}\left(r_{pin}\right)\right)$ that achieve 1 SQ = 8 [kg].

verification sampling plan; the specific nature of the set of diversion strategies does not matter and thus, we use the set X (not $\widetilde{X}$) as set of diversion strategies. Second, not any number r_{SFA} (e.g., $r_{SFA}\left(r_{pin}\right)=25$) can be achieved under the equal diversion hypothesis and the pin removal scenario.

Let $p_{instrument}\left(r_{pin}\right)$ be the instruments' identification probability in case r_{pin} pins are removed from an SFA. Then Eq. (1) yields for all $L \le 100/0.38 = 263$

$$\begin{aligned} p_{ICVD}\left(r_{pin}\right) &= \begin{cases} 1 & for \quad r_{pin}=L \\ 0 & for \quad 1\le r_{pin}\le L-1 \end{cases} \\ p_{DCVD}\left(r_{pin}\right) &= \begin{cases} 1 & for \quad \lceil 0.3L\rceil \le r_{pin}\le L \\ 0 & for \quad 1\le r_{pin}\le \lceil 0.3L\rceil -1 \end{cases} \\ p_{PGET}\left(r_{pin}\right) &= 1 \quad for \quad 1\le r_{pin}\le L. \end{aligned} \tag{4}$$

Sampling plans are usually based on the DP. In the context analysed in this paper we are interested in the detection of the diversion of 1 *SQ* of Pu from the spent fuel pond by performing item by item tests. This means here that the number of reported pins in an SFA is compared to the number of identified pins in that SFA. For that purpose, the inspector verifies n_1 SFAs with the ICVD, n_2 with the DCVD, and n_3 with the PGET, where per verified SFA only one measurement instrument is applied. Using the probability mass function of a hypergeometric distributed random variable, see, e.g., [1] or [11], the detection probability $DP\left(N,n_1,n_2,n_3,r_{pin}\right)$ is, using Eq. (4), given by

$$DP\left(N,n_1,n_2,n_3,r_{pin}\right)=\begin{cases} 1-\dfrac{\binom{N-r_{SFA}(r_{pin})}{n_3}}{\binom{N}{n_3}} & for \quad r_{\min}\le r_{pin}\le \lceil 0.3L\rceil -1 \\ 1-\dfrac{\binom{N-r_{SFA}(r_{pin})}{n_2+n_3}}{\binom{N}{n_2+n_3}} & for \quad \lceil 0.3L\rceil \le r_{pin}\le L-1 \\ 1-\dfrac{\binom{N-r_{SFA}(r_{pin})}{n_1+n_2+n_3}}{\binom{N}{n_1+n_2+n_3}} & for \quad r_{pin}=L, \end{cases} \tag{5}$$

keeping in mind that $\binom{a}{b}:=0$ for $b > a$ where a and b are integers, and where $r_{SFA}\left(r_{pin}\right)$ is given by Eq. (2). The derivation of Eq. (5) is done in section 7. Note that because the identification capability of the measurement instruments is modelled as a Yes/No decision, i.e. an attribute test is performed, the DP degenerates to a selection probability. Nevertheless, we still call the expression in Eq. (5) DP because this term is commonly used; see [3] for a detailed discussion. Also note, that in the three regions of r_{pin}-values in Eq. (5) only the numbers n_i are utilized for which the respective measurement instrument(s) yield(s) the identification probability of one.

We seek for a sampling plan (n_1, n_2, n_3) that achieves the required DP $1-\beta_{req}$ (set by the IAEA and/or EURATOM) independent of the actual diversion strategy, i.e.

$$DP\left(N,n_1,n_2,n_3,r_{pin}\right)\ge 1-\beta_{req} \text{ for all } r_{pin}\in X. \tag{6}$$

A sampling plan is called optimal, if it fulfils inequality (6), and if it minimizes the number of SFAs to be verified with the most expensive/time-consuming method (i.e. n_3), then minimizes the number of SFAs to be verified with the second most expensive/time-consuming method (i.e. n_2), and finally, minimizes the number of SFAs to be verified with the least expensive/time-consuming method (i.e. n_1), i.e. the lexicographic optimization criterion is applied; see [12].

Because the DP as defined by Eq. (5) is a monotone decreasing function of r_{pin}, i.e. $DP\left(N,n_1,\ n_2,n_3,r_{pin}\right)\ge DP\left(N,n_1,\ n_2,n_3,r_{pin}+1\right)$ for r_{pin} and r_{pin} + 1 from the same region, inequality (6) has to be valid for the three values $r_{pin}\in\left\{\lceil 0.3L\rceil -1, L-1, L\right\}$. Thus, the sampling plan (n_1, n_2, n_3) achieves the required DP $1-\beta_{req}$ if and only if

$$\max\left\{\frac{\binom{N-r_{SFA}(\lceil 0.3L\rceil -1)}{n_3}}{\binom{N}{n_3}},\frac{\binom{N-r_{SFA}(L-1)}{n_2+n_3}}{\binom{N}{n_2+n_3}},\frac{\binom{N-r_{SFA}(L)}{n_1+n_2+n_3}}{\binom{N}{n_1+n_2+n_3}}\right\}\le\beta_{req}. \tag{7}$$

Because for any N, any $1 \le r < N$ and any $1 \le r \le N - r$ we have, see, e.g., [1] or [3],

$$\frac{\binom{N-r}{n}}{\binom{N}{n}}=\prod_{j=0}^{r-1}\left(1-\frac{n}{N-j}\right)\le\prod_{j=0}^{r-1}\left(1-\frac{n}{N}\right)=\left(1-\frac{n}{N}\right)^r,$$

the sampling plan

$$\begin{aligned} n_3&=\left\lceil N\left(1-\sqrt[r_{SFA}(\lceil 0.3L\rceil -1)]{\beta_{req}}\right)\right\rceil, n_2=\left\lceil N\left(1-\sqrt[r_{SFA}(L-1)]{\beta_{req}}\right)\right\rceil-n_3 \\ n_1&=\left\lceil N\left(1-\sqrt[r_{SFA}(L)]{\beta_{req}}\right)\right\rceil-\left(n_3+n_2\right) \end{aligned} \tag{8}$$

fulfils inequality (7) where $r_{SFA}\left(r_{pin}\right)$ is given by Eq. (2). Note that the sampling plan given by Eq. (8) does not need to be optimal because it may overestimate the sample size by up to 3 SFAs (this is a general result in the attribute sampling context; see [13]).

4. One class of SFAs: Examples

In this section optimal sampling plans are determined for the examples in Table 3 where we vary 1) the required DP of 0.5 and 0.9 (first column), and 2) the type of SFAs in the spent fuel pond (BWR and PWR; first row). All other entries in Table 3 are explained in the course of this section.

	BWR, $N = 2500$, $L = 96$, $\bar{x}_{Pu} = 2$	PWR, $N = 500$, $L = 250$, $\bar{x}_{Pu} = 9$
$1-\beta_{req} = 0.5$	*ICVD*: 74 *DCVD*: 203 *PGET*: 121 *experienced*: 17 hours *inexperienced*: 21 hours	*ICVD*: 0 *DCVD*: 170 *PGET*: 80 *experienced*: 12 hours *inexperienced*: 15 hours
$1-\beta_{req} = 0.9$	*ICVD*: 172 *DCVD*: 543 *PGET*: 379 *experienced*: 53 hours *inexperienced*: 62 hours	*ICDV*: 0 *DCVD*: 231 *PGET*: 219 *experienced*: 29 hours *inexperienced*: 33 hours

Table 3: Examples.

r_{pin}	1	2	…	28	29	30	…	95	96
$r_{SFA}(r_{pin})$	384	192	…	14	14	13	…	5	4
$p_{ICVD}(r_{pin})$	0				0				1
$p_{DCVD}(r_{pin})$					1				
$p_{PGET}(r_{pin})$	1								

Table 4: Pairs $\left(r_{pin}, r_{SFA}(r_{pin})\right)$ that achieve $1\,SQ = 8$ [kg] and the identification probabilities as a function of the number r_{pin} of removed pins.

For a detailed discussion, we consider the BWR –90 % example: The spent fuel pond contains $N = 2500$ BWR SFAs, each having $L = 96$ fuel pins and an average amount $\bar{x}_{Pu} = 2$ [kg] of Pu per SFA. Table 4 illustrates in the first and second row the pairs $\left(r_{pin}, r_{SFA}(r_{pin})\right)$ that achieve $1\,SQ = 8$ [kg] of Pu, where $r_{SFA}(r_{pin})$ is given by Eq. (2). The third to fifth row represents the instruments' identification probability according to Eq. (4).

Table 4 demonstrates that in case of a bias defect (i.e. only small numbers of removed pins) only the PGET is capable to identify a falsified SFA as falsified, whereas only in case of a gross defect (all pins are removed) all instruments lead to the identification probability one.

For illustration, consider the sampling plan $(n_1, n_2, n_3) = (10,65,25)$. Figure 1 shows the achieved DP given by Eq. (5) as a function of the number r_{pin} of removed pins. The two vertical lines divide the graph into three regions: in the left region ($1 \le r_{pin} \le 28$) only the PGET is capable to identify a falsified SFA as falsified, in the middle region ($29 \le r_{pin} \le 95$) both the PGET and the DCVD are capable to identify a falsified SFA as falsified, and only in the right region ($r_{pin} = L = 96$) all three instruments are successful in identifying a falsified SFA as falsified.

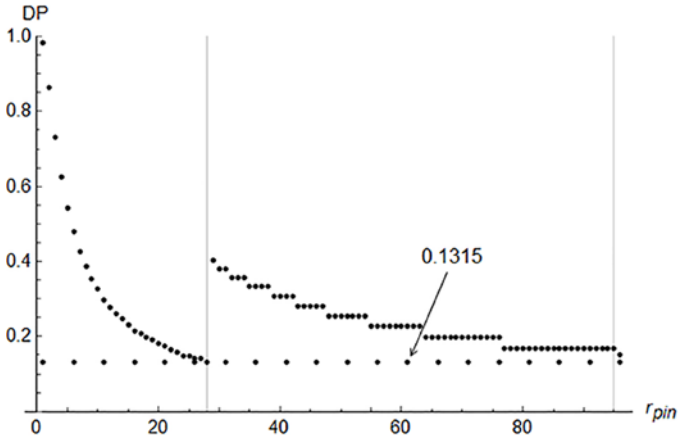

Figure 1: Achieved DP for the sampling plan $(n_1, n_2, n_3) = (10, 65, 25)$.

Three comments on Figure 1:

First, the sampling plan $(n_1, n_2, n_3) = (10,65,25)$ achieves a DP of about 0.1315 (horizontal dots) independent of the actual diversion strategy because the minimum of $DP(N, n_1, n_2, n_3, r_{pin})$ is attained at $r_{pin} = 28$, and we obtain, using Eq. (5), that $DP(N, n_1, n_2, n_3, 28) \approx 0.1315$.

Second, the DP curve is a monotone (but not strictly) decreasing function of r_{pin} in the regions $r_{pin} = 1, \ldots, 28$ and

r_{pin} = 29, …, 95, respectively. This result is plausible, because with an increasing number of removed pins the number of falsified SFAs in the pond decreases (i.e. $r_{SFA}\left(r_{pin}\right) \geq r_{SFA}\left(r_{pin}+1\right)$), and thus, the probability to select at least one falsified SFA when $r_{SFA}\left(r_{pin}\right)$ are in the pond is greater or equal than the probability to select at least one falsified SFA when $r_{SFA}\left(r_{pin}+1\right)$ are in the pond.

Third, the value of the DP is constant, e.g., for all numbers r_{pin} = 48, …,54, because they lead to the same number of falsified SFAs ($r_{SFA}\left(48\right)=\ldots=r_{SFA}\left(54\right)=8$, see Table 2) and because in that region both the PGET and the DCVD are capable to identify a falsified SFA as falsified. In contrast, although $r_{SFA}\left(28\right)=r_{SFA}\left(29\right)=14$ we see that $DP\left(N,n_1,n_2,n_3,28\right) < DP\left(N,n_1,n_2,n_3,29\right)$, because in case r_{pin} = 29 both the PGET and the DCVD are being used and $n_2 > 0$.

Suppose the inspector wants to achieve a required DP of (say) 0.9. How many SFAs does he need to verify? Eq. (8) implies that the sampling plan (n_1, n_2, n_3) = (172,543,380) achieves a DP of 0.9, i.e. at least 380 SFAs must be verified by the PGET. This sampling plan, however, is not optimal in the sense defined after inequality (6), because the number of PGET measurements can be reduced to 379 and the sampling plan (172,543,379) still achieves a DP of 0.9. This illustrates that the sampling plan given by Eq. (8) does not have to be optimal (see also the comment at the end of section 3). Using the net measurement times from Table 1, we see that an experienced inspector needs about 53 hours net measurement time, while an inexperienced one needs about 62 hours (times are rounded down to full hours). Both measurement times are unrealistic and thus, the optimal sampling plan (172,543,379) may be infeasible in practice. The results of the BWR-90% example are summarized in the respective field in Table 3.

The optimal sampling plans for the remaining examples in Table 3 can be obtained in the same way. Therefore, we just make two comments: First, the identification probabilities for the PWR examples are, using Eq. (4),

$$p_{ICVD}\left(r_{pin}\right) = \begin{cases} 1 & for \quad r_{pin}=250 \\ 0 & for \quad 1\leq r_{pin}\leq 249 \end{cases}$$

$$p_{DCVD}\left(r_{pin}\right) = \begin{cases} 1 & for \quad 75\leq r_{pin}\leq 250 \\ 0 & for \quad 1\leq r_{pin}\leq 74 \end{cases}$$

$$p_{PGET}\left(r_{pin}\right) = 1 \quad for \quad 1\leq r_{pin}\leq 250.$$

Second, because Eq. (2) implies $r_{SFA}\left(249\right)=r_{SFA}\left(250\right)=1$, the requirement $DP\left(N,n_1,n_2,n_3,95\right)\geq 1-\beta_{req}$ implies $DP\left(N,n_1,n_2,n_3,96\right)\geq 1-\beta_{req}$ for any $n_1 \geq 0$, and thus, there is no need to perform any ICVD measurement.

It has to be emphasized that the optimal sampling plans in Table 3 highly depend on the definition of the identification probabilities given by Eqs. (1) and (4).

To further illustrate the approach of section 3, we discuss two topics. First, we determine the optimal sampling plan if either "PGET and ICVD" (case 1) or "PGET and DCVD" (case 2) can be applied. Consider a spent fuel pond with N = 2000 BWR SFAs (with L = 96 pins each) and an average amount $\bar{x}_{Pu}=0.5SQ=4$ [kg] of Pu per SFA. If the required DP is 0.9, then the optimal sampling plans that achieve the DP of 0.9 are given by

$$case1: \begin{matrix} ICVD: & 296 \\ PGET: & 1072 \end{matrix}, \quad case2: \begin{matrix} DCVD: & 808 \\ PGET: & 560 \end{matrix}$$

The number of PGET measurements in case 1 is considerably higher compared to case 2. This is due to the fact that in case 1 the PGET has to cover all pin removals r_{pin} with $1\leq r_{pin}\leq 95$, where in case 2 only the region $1\leq r_{pin}\leq 28$ has solely covered by the PGET.

Second, suppose only 20 PGET measurements can be performed, but there is no restriction on the number of ICVD measurements, i.e. the entire spent fuel pond can be verified by the ICVD. Thus, we consider the sampling plan (n_1, n_2, n_3) = (1980,0,20) that yields, using Eq. (5), an achieved DP of about 0.028, which is usually far too low in this context.

In this section only one class of SFAs has been considered which is a valid assumption if the variation (variance) of the amount of Pu amongst the SFAs in the spent fuel pond is not "too big". An example with two classes of SFAs is presented in section 6.

5. One class of SFAs: Non-equal diversion scenarios

In this section non-equal diversion scenarios, which are usually not addressed in common safeguards literature, are considered.

The sampling plans in sections 3 and 4 are based on the equal diversion hypothesis which leads to the relation between r_{pin} and $r_{SAF}\left(r_{pin}\right)$ in Eq. (2). The diverter, however, does not need to falsify SFAs according to this hypothesis. For illustration, let N = 2000, L = 96 and $\bar{x}_{Pu}=2$ [kg] and let the diverter removes 4 pins from 21 SFAs and 30 pins from 10 SFAs. Then he acquires exactly

$$\frac{2\ [kg]}{96}\times\left(4\times 21+30\times 10\right)=8\ [kg]\ ,$$

of Pu. Using Table 4, we see that the 21 SFAs falsified by 4 pins each can only be successfully identified as falsified by the PGET, while the 10 SFAs falsified by 30 pins each can be identified as falsified by both the PGET and the DCVD.

Let us assume that the required DP is 0.5. Following the same procedure as described in section 4 for BWR-90% example, we find the sampling plan (n_1, n_2, n_3) =

(59,162,97) to be optimal if the equal diversion hypothesis is true. What is the achieved DP if the diverter removes the pins as indicated above and if the inspector sticks to the optimal sampling plan (59,162,97)?

We first determine the achieved DP in case the sampling is performed in the order $n_3 \to n_2 \to n_1$, which means that we first sample the SFAs verified by the PGET, then we sample (from the remaining $N - n_3$ SFAs) the SFAs verified by the DCVD, and finally we sample (from the remaining $N - n_3 - n_2$ SFAs) the SFAs verified by the ICVD. The event of non-detection occurs if for the PGET measurements none of the 21 + 10 = 31 SFAs are in the sample, and for the subsequent DCVD measurements none of the 10 SFAs with 30 missing pins are in the sample. Thus, the achieved DP is

$$1-\frac{\binom{31}{0}\binom{N-31}{n_3}}{\binom{N}{n_3}}\frac{\binom{10}{0}\binom{N-n_3-10}{n_2}}{\binom{N-n_3}{n_2}} \approx 0.91.$$

In case the sampling is done in the order $n_3 \to n_2 \to n_1$, the event of non-detection occurs if for the DCVD measurements none of the 10 SFAs with 30 missing pins but i SFAs out of the 21 SFAs with 4 missing pins (and which can only be identified with PGET) are sampled, and for the subsequent PGET measurements none of $21 - i$ remaining SFAs with 4 missing pins, are sampled. The achieved DP is, using the multivariate hypergeometric distribution (see [11]), given by

$$1-\sum_{i=0}^{21}\frac{\binom{21}{i}\binom{10}{0}\binom{N-31}{n_2-i}}{\binom{N}{n_2}}\frac{\binom{21-i}{0}\binom{N-n_2-(21-i)}{n_3}}{\binom{N-n_2}{n_3}} \approx 0.85.$$

Two comments on this example: First, the achieved DP depends on the order the sampling is performed: The order $n_3 \to n_2 \to n_1$ leads – at least in this example – to a higher DP than the order $n_2 \to n_3 \to n_1$. Whether this is true in general has to be investigated. In section 7 it is shown that under the equal diversion hypothesis the order of sampling does not have any influence on the DP.

Second, the achieved DP is – for both orders considered above and using the optimal sampling plan (59,162,97) – higher than 0.5 which was used for finding (59,162,97) under the equal diversion hypothesis. Therefore, one can ask whether this hypothesis is a worst case in the sense that the sampling plan found under the equal diversion hypothesis also achieves the required DP for all non-equal diversion scenarios, i.e. in case the diverter does not remove pins according to the equal diversion hypothesis.

6. Two classes of SFAs: Example

We now consider two classes of BWR (with $L = 96$ pins each) SFAs with $N_1 = 217$ and $N_2 = 297$ SFAs per class in the same spent fuel pond, e.g., one class of SFAs with high burn-up and one class of SFAs with very low burn-up. The average amounts of Pu are assumed to be $\bar{x}_1 = 1.5$ [kg] and $\bar{x}_2 = 3$ [kg] of Pu per SFA in class $i = 1,2$. Again, the diverter wants to remove pins from SFAs to acquire 8 [kg] of Pu. In contrast to sections 3 and 4 he can now get the material from both classes: If m_i, $i = 1,2$, denotes the nuclear material mass diverted from class i, then we have $m_1 + m_2 \geq 8$. To keep the example manageable, we only take special values of (m_1, m_2) into account:

$$M := \{(8,0),(7,1),(6,2),(5,3),(4,4),(3,5),(2,6),(1,7),(0,8)\}. \quad (9)$$

Because $8 \leq \bar{x}_i N_i$ for $i = 1,2$, we have $(8,0),(0,8) \in M$. Within each class the diverter is – as before – assumed to remove $r_{pin,i}$ from $r_{SFA}(m_i, r_{pin,i})$ SFAs of class i, $i = 1,2$, where, using Eq. (2),

$$r_{SFA,i}(m_i, r_{pin,i}) = \left\lceil \frac{m_i \times 96}{\bar{x}_i} \frac{1}{r_{pin,i}} \right\rceil. \quad (10)$$

Let $n_{1,j}$ resp. $n_{2,j}$, $j = 1,2,3$, denote the sample size in class 1 and 2, where $n_{1,1}$ resp. $n_{2,1}$ SFAs are verified by the ICVD, $n_{1,2}$ resp. $n_{2,2}$ by the DCVD, and $n_{1,3}$ resp. $n_{2,3}$ by the PGET, i.e. the first index indicates the class and the second one the measurement method. The identification probabilities are given in Table 4.

Using Eq. (3), the sets $X_1(m_1)$ and $X_2(m_2)$ of diversion strategies in the first resp. second class is for $i = 1,2$ given by

$$X_i(m_i) = \left\{ \left\lceil \frac{m_i \times L}{\bar{x}_i N_i} \right\rceil, \ldots, L \right\}.$$

The overall (over both classes together) DP is, for any $(m_1, m_2) \in M$ and for any $(r_{pin,1}, r_{pin,2}) \in X_1(m_1) \times X_2(m_2)$, given by

$$DP(N_1, N_2, n_{1,1}, n_{1,2}, n_{1,3}, n_{2,1}, n_{2,2}, n_{2,3}, m_1, r_{pin,1}, m_2, r_{pin,2}) \quad (11)$$
$$= 1 - (1 - DP(N_1, n_{1,1}, n_{1,2}, n_{1,3}, m_1, r_{pin,1}))(1 - DP(N_2, n_{2,1}, n_{2,2}, n_{2,3}, m_2, r_{pin,2})),$$

where $DP(N_1, n_{1,1}, n_{1,2}, n_{1,3}, m_1, r_{pin,1})$ and $DP(N_2, n_{2,1}, n_{2,2}, n_{2,3}, m_2, r_{pin,2})$ are defined by Eq. (5) in which $r_{SFA,i}(m_i, r_{pin,i})$ of Eq. (10) is used.

As before we are interested in sampling plans $(n_{1,1}, n_{1,2}, n_{1,3})$ and $(n_{2,1}, n_{2,2}, n_{2,3})$ that achieve the required DP $1 - \beta_{req}$ independent of the actual diversion strategy. Because the diverter may acquire 1 *SQ* from one of the classes only (see the left and right element in the set M in Eq. (9)), the approach is section 3 implies that $(n_{1,1}, n_{1,2}, n_{1,3})$ and $(n_{2,1}, n_{2,2}, n_{2,3})$ have to fulfil inequality (7) for each class separately. This gives for $\beta_{req} = 0.1$ the optimal sampling plans

$$(n_{1,1}, n_{1,2}, n_{1,3}) = (0,45,24) \text{ and } (n_{2,1}, n_{2,2}, n_{2,3}) = (0,98,61) \quad (12)$$

for each class individually. Does the sampling plan given by Eq. (12) achieves the overall DP of 0.9 for all diversion strategies $(m_1,m_2)\in M$ or only for $(m_1,m_2)=(0,8)$ and $(m_1,m_2)=(8,0)$? I.e. we need to check whether the achieved overall DP is at least 0.9 for all pairs $(m_1,m_2)\in M$, i.e. whether

$$\min_{(m_1,m_2)\in M}\ \min_{(r_{pin,1},r_{pin,2})\in X_1(m_1)\times X_2(m_2)} DP\left(N_1,N_2,n_{1,1},n_{1,2},n_{1,3},n_{2,1},n_{2,2},n_{2,3},m_1,r_{pin,1},m_2,r_{pin,2}\right) \quad (13)$$

is at least 0.9. According the multiplicative structure of the overall DP in Eq. (11), the minimization of the overall DP over the set $(r_{pin,1},r_{pin,2})\in X_1(m_1)\times X_2(m_2)$ is equivalent to minimizing the individual DPs $DP(N_1, n_{1,1}, n_{1,2}, n_{1,3}, m_1, r_{pin,1})$ and $DP(N_2, n_{2,1}, n_{2,2}, n_{2,3}, m_2, r_{pin,2})$ over $X_1(m_1)$ and $X_2(m_2)$, respectively.

Consider the pair $(m_1,m_2)=(2,6)$. Then Eqs. (5) and (12) imply (rounded to the fourth digit after the dot)

$$DP\left(N_1,n_{1,1},n_{1,2},n_{1,3},2,r_{pin,1}\right)=\begin{cases}0.4467 & r_{pin,1}=28\\ 0.5358 & for\quad r_{pin,1}=95\\ 0.5358 & r_{pin,1}=96\end{cases}$$

and

$$DP\left(N_2,n_{2,1},n_{2,2},n_{2,3},6,r_{pin,2}\right)=\begin{cases}0.8037 & r_{pin,2}=28\\ 0.9009 & for\quad r_{pin,2}=95\\ 0.7849 & r_{pin,2}=96,\end{cases}$$

and thus, we get for the achieved overall DP by Eq. (11) and the comment after Eq. (13)

$$1-(1-0.4467)\times(1-0.7849)=0.881<0.9,$$

i.e. the sampling plan given by Eq. (12) does not achieve the required overall DP of 0.9. If we increase in Eq. (12) the ICVD measurements by 1 verification in each class, and the DCVD and PGET measurements by 3 verifications in each class, i.e. if we consider the sampling plan

$$(n_{1,1},n_{1,2},n_{1,3})=(1,48,27)\ and\ (n_{2,1},n_{2,2},n_{2,3})=(1,101,64), \quad (14)$$

then the overall DP of 0.9 is achieved for all diversion strategies $(m_1,m_2)\in M$.

Two remarks: First, the sampling plan given by Eq. (14) is most likely not optimal, i.e. a sampling plan with shorter net measurement times might be found using more sophisticated methods other than just shifting sample sizes by a constant. Second, the sampling plan given by Eq. (14) achieves the overall DP of 0.9 for all diversion strategies $(m_1,m_2)\in M$ but not necessarily for all diversion strategies of a more refined set which includes M as a subset, such as

$$\{(8,0),(7.5,0.5),(7,1),\ldots,(1,7),(0.5,7.5),(0,8)\}$$

in which, in contrast to Eq. (9), an incremental step of 0.5 [kg] is used. Indeed, the sampling plan given by Eq. (14) yields an achieved overall DP of about 0.898 for $(m_1,m_2)=(4.5,3.5)$.

7. Derivations

To derive Eq. (5), we need to model the way the random sampling is performed: Quite generally, the following orders are possible: $n_3\to n_2\to n_1$, $n_3\to n_1\to n_2$, $n_2\to n_1\to n_3$, $n_2\to n_3\to n_1$, $n_1\to n_2\to n_3$ and $n_1\to n_3\to n_2$ ($n_3\to n_2\to n_1$ means: first sample the SFAs that are verified by the PGET, then sample the SFAs verified by the DCVD, and finally sample the SFAs verified by the ICVD) and the possibility to choose $n_1+n_2+n_3$ SFAs from the population of SFAs and then distributed them to the verification methods i, i = 1,2,3. We claim that Eq. (5) is true independent of the chosen order, and prove this statement for the cases: 1) $n_3\to n_2\to n_1$ and 2) $n_2\to n_3\to n_1$. Although the proof in case 1) is rather obvious, we present it here in order to show the differences between cases 1) and 2).

Ad 1): If $1\le r_{pin}\le\lceil 0.3L\rceil-1$, then non-detection occurs if and only if none of the $r_{SFA}(r_{pin})$ falsified SFAs are sampled for PGET verifications. The DCVD and ICVD measurements do not influence the DP in this case. Thus, we get with $r_{SFA}:=r_{SFA}(r_{pin})$

$$1-\frac{\binom{r_{SFA}}{0}\binom{N-r_{SFA}}{n_3}}{\binom{N}{n_3}}=1-\frac{\binom{N-r_{SFA}}{n_3}}{\binom{N}{n_3}} \quad (15)$$

which is the first equation in Eq. (5). If $\lceil 0.3L\rceil\le r_{pin}\le L-1$, then non-detection occurs if and only if none of the $r_{SFA}(r_{pin})$ falsified SFAs are sampled for PGET or DCVD verifications. The ICVD measurements do not influence the DP in this case. Thus, we have

$$1-\frac{\binom{r_{SFA}}{0}\binom{N-r_{SFA}}{n_3}}{\binom{N}{n_3}}\cdot\frac{\binom{r_{SFA}}{0}\binom{N-n_3-r_{SFA}}{n_2}}{\binom{N-n_3}{n_2}}=1-\frac{\binom{N-r_{SFA}}{n_2+n_3}}{\binom{N}{n_2+n_3}} \quad (16)$$

where the equal sign can be shown by expanding the binomial coefficients. If $r_{pin}=L$, then we get in analogy to Eq. (16)

$$1-\frac{\binom{N-r_{SFA}}{n_3}}{\binom{N}{n_3}}\cdot\frac{\binom{N-n_3-r_{SFA}}{n_2}}{\binom{N-n_3}{n_2}}\cdot\frac{\binom{N-(n_3+n_2)-r_{SFA}}{n_1}}{\binom{N-(n_3+n_2)}{n_1}}=1-\frac{\binom{N-r_{SFA}}{n_1+n_2+n_3}}{\binom{N}{n_1+n_2+n_3}} \quad (17)$$

i.e. the third equation in Eq. (5).

Ad 2): If $1\le r_{pin}\le\lceil 0.3L\rceil-1$, then non-detection occurs 1) if any SFA is sampled for DVCD verifications (i.e. even falsified SFAs can be sampled, because they can only be identified as falsified by the PGET), and 2) if none of the

remaining falsified SFAs are sampled for PGET verifications. Again, the ICVD measurements do not have an impact on the DP in this case. Thus, we obtain for the DP with $r_{SFA} := r_{SFA}(r_{pin})$

$$1-\sum_{i=Max(0,n_2+n_3-(N-r_{SFA}))}^{Min(r_{SFA},n_2)} \frac{\binom{r_{SFA}}{i}\binom{N-r_{SFA}}{n_2-i}}{\binom{N}{n_2}} \frac{\binom{r_{SFA}-i}{0}\binom{N-n_2-(r_{SFA}-i)}{n_3}}{\binom{N-n_2}{n_3}}. \quad (18)$$

Note that the lower bound of the sum in Eq. (18) is due to the fact that $N-r_{SFA} \geq n_2 - i$ and $N-n_2-(r_{SFA}-i) \geq n_3$, which is equivalent to $i \geq n_2-(N-r_{SFA})$ and $i \geq n_2+n_3-(N-r_{SFA})$.

Eqs. (15) and (18) demonstrate the influence of the order the sampling is done on the DP formula. As announced, however, we show that both DP formulae are equivalent.

Expanding the binomial coefficients, the sum expression in Eq. (18) simplifies to

$$\binom{N}{r_{SFA}}^{-1} \sum_{i=Max(0,n_2+n_3-(N-r_{SFA}))}^{Min(r_{SFA},n_2)} \binom{n_2}{i}\binom{N-(n_2+n_3)}{r_{SFA}-i}. \quad (19)$$

Using the identity

$$\sum_{k=Max(0,m-b)}^{Min(m,a)} \binom{a}{k}\binom{b}{m-k} = \binom{a+b}{m}$$

for any positive integers a, b and m, see [11], we finally get from Eq. (19), using the substitutions $a \to n_2$, $b \to N-(n_2+n_3)$ and $m \to r_{SFA}$,

$$\binom{N}{r_{SFA}}^{-1} \sum_{i=Max(0,n_2+n_3-(N-r_{SFA}))}^{Min(r_{SFA},n_2)} \binom{n_2}{i}\binom{N-(n_2+n_3)}{r_{SFA}-i} = \frac{\binom{N-n_3}{r_{SFA}}}{\binom{N}{r_{SFA}}} = \frac{\binom{N-r_{SFA}}{n_3}}{\binom{N}{n_3}},$$

i.e. the first line of Eq. (5) and Eq. (15). If $\lceil 0.3L \rceil \leq r_{pin} \leq L-1$, then the non-detection event occurs if and only if none of the $r_{SFA}(r_{pin})$ falsified SFAs are sampled for the PGET and DCVD verifications. Thus, its probability is given by Eq. (16) changing $n_3 \to n_2$ and $n_2 \to n_3$. The case $r_{pin} = L$ is given by Eq. (17) again with the replacements $n_3 \to n_2$ and $n_2 \to n_3$.

8. Future work and outlook

The following four topics could be examined in future research activities: First, a sensitivity analysis could be carried out that studies the consequences of the instruments identification thresholds on optimal sampling plans. For example: The ICVD identification threshold could be lower down from 100% to 50%, i.e. the identification probability is one if and only if "50% of the pins or more have been removed"; see Eq. (1). For the DCVD, a reduction of the 30% threshold down to 10% could be considered.

Second, as expanded at the end of section 5, it should be investigated whether optimal sampling plans obtained under the equal diversion hypothesis assure the required DP for all non-equal diversion scenarios. Also the influence of the order the sampling is performed on the DP needs to be investigated.

Third, in case of a non-homogeneous population of SFAs in a spent fuel pond the question of the appropriate number of classes of SFAs, which are characterized by different average amounts of Pu, has to be addressed. This number will depend on the SFAs masses and their variation (variance). A related topic has already been investigated in [14].

Fourth, the example in section 6 calls for an efficient algorithm for the determination of optimal sampling plans in case more than one class of SFAs are stored in the spent fuel pond.

In a future scenario the use of robots could support the inspectorates to confirm the presence of spent fuel in a pond. In this light a nuclear focused robotics challenge co-hosted by the IAEA took place in November 2017 in Australia. The aim of this challenge was to attach an ICVD inside a small robotized floating platform, which autonomously carries out the verification measurements by moving across the surface of the pond; see [15]. The consequences of using robots on the sample sizes can be studied as soon as it becomes clear which inspection activities can be carried through or supported by robots and what the robots' identification capabilities are.

9. Acknowledgements

The authors would like to thank K. Schoop, P. Schwalbach and A. Kavka (DG ENER) for initiating the studies presented in this paper and their helpful support.

10. Disclaimer

Neither the authors of this paper, nor the organization or industrial company they are affiliated with, nor the Federal Government of Germany assume any liability whatsoever for any use of this paper or parts of it. Furthermore, the content of this paper does not reflect any policy of the Federal Government of Germany.

11. References

[1] R. Avenhaus and M. J. Canty, Compliance Quantified - An Introduction to Data Verification, Cambridge, UK: Cambridge University Press, 1996.

[2] J. L. Jaech, Statistical Methods in Nuclear Material Control, Oak Ridge, Tennessee: Technical Information Center, United States Atomic Energy Commission, 1973.

[3] IAEA, Statistical Methods for Verification Sampling Plans (STR 381), Vienna: IAEA, 2017.

[4] E. Branger, S. Jacobsson Svärd, S. Grape and E. Wernersson, "Towards unattended partial-defect verification of irradiated nuclear fuel assemblies using the DCVD," in *Proceedings of the Symposium on International Safeguards: Linking Strategy, Implementation and People*, Vienna, 2014.

[5] J. D. Chen, "Spent fuel verification using a digital Cerenkov viewing device," in *International Conference on Facility Operations - Proceedings*, Portland, 2088.

[6] IAEA, IAEA Safeguards Glossary, 2001 Edition (IAEA International Nuclear Verification Series No. 3), Vienna: IAEA, 2002.

[7] T. Honkamaa, F. Levai, A. Turunen, R. Berndt, S. Vaccaro and P. Schwalbach, "Prototype for passive gamma emission tomography," in *Proceedings of the Symposium on International Safeguards: Linking Strategy, Implementation and People*, Vienna, 2014.

[8] IAEA, "Review of Fuel Failures in Water Cooled Reactors," IAEA, Vienna, 2007.

[9] T. A. White, M. Mayorov, A. R. Lebrun and P. Peura, "Verification of Spent Fuel Nuclear Fuel using Passive Gamma Emission Tomography (PGET)," in *Proceedings of the Symposium on International Safeguards: Building Future Safeguards Capabilities*, Vienna, 2018.

[10] EURATOM, *Personal communication with K. Schoop, P. Schwalbach and A. Kavka,* 2018.

[11] V. K. Rohatgi, Statistical Inference, Mineola, N.Y.: Dover Publications Inc., 2003.

[12] M. Ehrgott, Multicriteria Optimization, Berlin: Springer, 2nd ed. 2005.

[13] T. Krieger and T. L. Burr, "Comparison of an Exact to an Approximate Sample Size Calculation for Attribute Testing," *Journal of Nuclear Materials Management,* vol. XLIV, no. 3, pp. 45-48, 2016.

[14] T. Krieger, T. L. Burr and C. F. Norman, "Consequences of non-zero item variability on the IAEA's inspection sampling plans," in *Proceedings of the INMM 58th Annual Meeting*, Indian Wells, California USA, July 16-20, 2017.

[15] CSIRO, "https://www.csiro.au/en/News/News-releases/2017/International-Robotics-Challenge," November 2017. [Online]. Available: https://www.csiro.au/en/News/News-releases/2017/International-Robotics-Challenge. [Accessed 26 September 2018].

Parametrization of the differential die-away self-interrogation early die-away time for PWR spent fuel assemblies

Li Caldeira Balkeståhl, Zsolt Elter, Sophie Grape
Uppsala University, Division of Applied Nuclear Physics, Uppsala, Sweden

Abstract:

The differential die-away self-interrogation (DDSI) instrument developed and built in Los Alamos National Laboratory (LANL) is being considered for verification before final disposal. One of the signals from this instrument, the early die-away time, has been shown to be proportional to the multiplication of the spent fuel assembly. Full-scale simulations of the instrument response using MCNP are time consuming. This may become a problem in cases when the instrument response to a large number of fuel assemblies is required, such as in the case of training machine learning models.

In this paper, we propose a parametrization of the early die-away time as a function of initial enrichment (IE), burn-up (BU) and cooling time (CT), for intact PWR spent fuel assemblies. The parametrization is calculated from a dataset of 1040 simulated PWR spent fuel assemblies with fuel parameters in the range of IE=2-5%, BU=15-60 GWd/tU and CT=5-70 years. The simulations are done using Serpent2 for the depletion calculation and MCNP6 for the neutron transport and detection in the DDSI.

It was found that the CT dependence can be decoupled from the BU and IE dependence, and that it follows an exponential decay. The BU and IE dependences have been fitted with several different functions, and the best fit was chosen based on the chi-square value. The determination of the die-away time using the parametrization has been tested on a separate dataset, resulting in a root mean square error (RMSE) of 0.6 μs (the early die-away time ranges from 28 μs to 84 μs). A description of this work is given in the paper together with details on the choice of parametrizing function, and qualitative arguments for that choice.

Keywords: DDSI; die-away time; parametrization; modelling; PWR

1. Introduction

The differential die-away self-interrogation (DDSI) technique has been studied by Los Alamos National Laboratory (LANL) [1] as part of the Next Generation Safeguards Initiative - Spent Fuel [2]. A prototype instrument has been manufactured and recently tested on spent nuclear fuel at Clab [3]; the technique may also be considered for future use at encapsulation facilities.

As has been shown in [4] for simulation space, and in [3] and [5] for experimental data, the DDSI early die-away time, τ, is proportional to the multiplication of a fuel assembly. The early die-away time is defined as the decay constant in an exponential fit to the real coincidence Rossi-alpha distribution for neutrons, in the time domain of 4 to 52 μs. The proportionality to the multiplication makes τ an interesting instrument response to study, especially in the context of nuclear safeguards verification where the fuel assembly parameters initial enrichment (IE), burnup (BU) and cooling time (IE) as well as fissile mass are central concepts. The reason is that assembly multiplication reflects the balance between the fissile content and neutron absorbers such as fission products and minor actinides in the assembly. This balance, in turn, varies with the fuel parameters IE, BU, and CT.

Full-scale simulations of the DDSI instrument response using Monte Carlo techniques are however time consuming, especially if many such simulations are needed. For this reason, we here present a parametrization of the early die-away time, as a function of fuel parameters CT, IE and BU, which can be used as an approximation of the instrument response in place of the full simulations.

Section 2 of this paper describes the simulation methods used to obtain the instrument response, section 3 explains how the parametrization was derived and section 4 shows the results of the parametrization for a separate data set.

2. Simulation methods

The simulations of the response of the DDSI instrument to spent nuclear fuel are done in two steps. In the first step, a depletion calculation is performed with Serpent2 [6] to get the isotopic content of the spent fuel. In the second step, the neutron transport and detection is simulated in MCNP6 [7].

Simulations have been performed for 1040 PWR spent fuel assemblies, covering a range of values of IE, BU and CT. IE ranges from 2-5 % atomic weight in steps of 0.25 % (corresponding to a range of 1.98 to 4.94 % in mass weight), and BU ranges between 15-60 GWd/tU in

steps of 5 GWd/tU up to 40 GWd/tU and then in two more steps of 10 GWd/tU. CT ranges between 5-70 y, with smaller steps for shorter cooling times (5 y, 7.5 y, 10 y, 12.5 y, 15 y, 20 y, 30 y, 40 y, 55 y and 70 y). The choice of a grid with an uneven sampling of BU and CT space is made to more accurately capture the variation of τ with these variables, with a smaller grid spacing where τ changes more rapidly.

2.1 Burnup calculation

The burnup, or depletion, calculation is performed in Serpent2 in criticality source mode, in an infinite 2D lattice. The geometry consists of one pin surrounded by water, with reflective boundary conditions. The pin radius is 0.41 cm, the inner cladding radius 0.42 cm, the outer cladding radius 0.48 cm and the pitch 1.26 cm.

The fuel cycles are defined as cycles of 365 days of irradiation at constant power density, resulting in a burnup of 10 GWd/tU per cycle, followed by a down-time of 30 days. The length of the last cycle is adjusted to give the desired burnup, and the desired cooling time is then calculated with the radioactive decay of the spent fuel.

The simulated spent fuel assemblies resulting from this depletion calculation are ideal in several respects: the assembly is uniform, all pins have identical properties; and all assemblies follow idealized cycles (while commercial assemblies might *e.g.* spend a cycle outside the reactor).

2.2 DDSI physics and modelling

The DDSI instrument consists of 56 ^{3}He tubes in four detector pods surrounding the fuel assembly, as described in [1]. The instrument detects neutrons emitted from the spent nuclear fuel, and can be used to calculate the early die-away time τ.

The detected neutrons follow the Rossi-alpha distribution (shown in figure 1). This distribution describes the time difference between detected neutrons, and the non-flat distribution can be explained by the correlation between detected neutrons from the same fission or fission chain. There are in fact two components that describe the neutron correlation, a fast and a slow component, and both are exponential in nature. The fast component corresponds to neutrons from the same fission event or from a fast fission chain, but since the instrument is not capable of resolving this time scale, the decay time of this component instead depends on the instrument geometry and the thermalization of the neutrons before detection. The slow component corresponds to neutrons from a thermal fission chain, i.e. where the neutron thermalizes before inducing a new fission.

The early die-way time results from an interplay between the two components, and has been shown [3-5] to be proportional to the multiplication of the fuel assembly. τ measures how long the neutron population survives in the spent fuel and a larger τ -value shows that the neutrons die-away more slowly. Fissile material therefore increases τ, while neutron poisons decrease it, and the value for each spent fuel assembly is a result of the interplay between these two types of materials.

In MCNP6, the DDSI instrument is modelled surrounding PWR 17x17 spent fuel assemblies, all submerged in water. The fuel pins in the assembly have the geometry described earlier, and the material composition is taken from the output of the Serpent2 simulation. The source term is defined as a spontaneous fission source, and it is distributed evenly in all the fuel rods. The source is restricted to 145 cm of axial length, centred on the DDSI instrument, as a means to speed up the simulation while retaining most of the signal (for details see [8]). The F8 coincidence capture tallies are used to calculate the Rossi-alpha distribution of real coincidences, similarly as in [1]. The Rossi-alpha distribution is simulated from 0 to 200 μs, and τ is calculated from an exponential fit over the range 4-52 μs (including statistical errors).

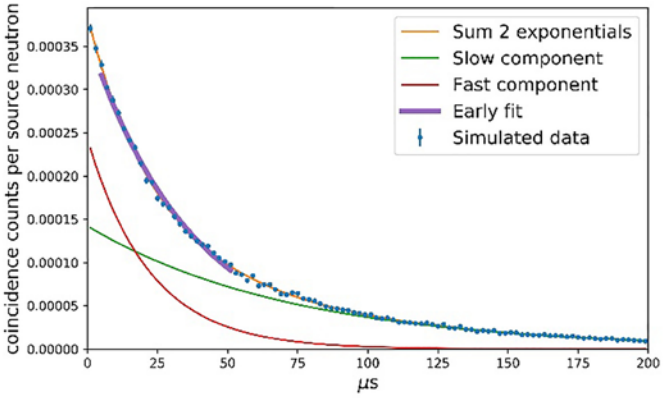

Figure 1: Rossi-alpha distribution for real coincident neutrons as simulated with MCNP6. The simulated spent fuel assembly has IE=3.5 %, BU=43 GWd/tU and CT=59 y, and τ= 37.0 ± 0.4 μs.

3. Parametrization of τ

Intuitively, since the early die-away time is proportional to multiplication, we expect it to decrease with BU (less fissile material and more neutron absorbers are present) and to increase with IE (more fissile material is present). The CT dependence is not so intuitive, most of the fissile material will not depend on CT, although ^{241}Pu does. Figures 2-4 show how τ depends on IE, BU and CT for a part of the data. The dependence for the whole dataset is smooth, and an interpolation between the shown data points can be made.

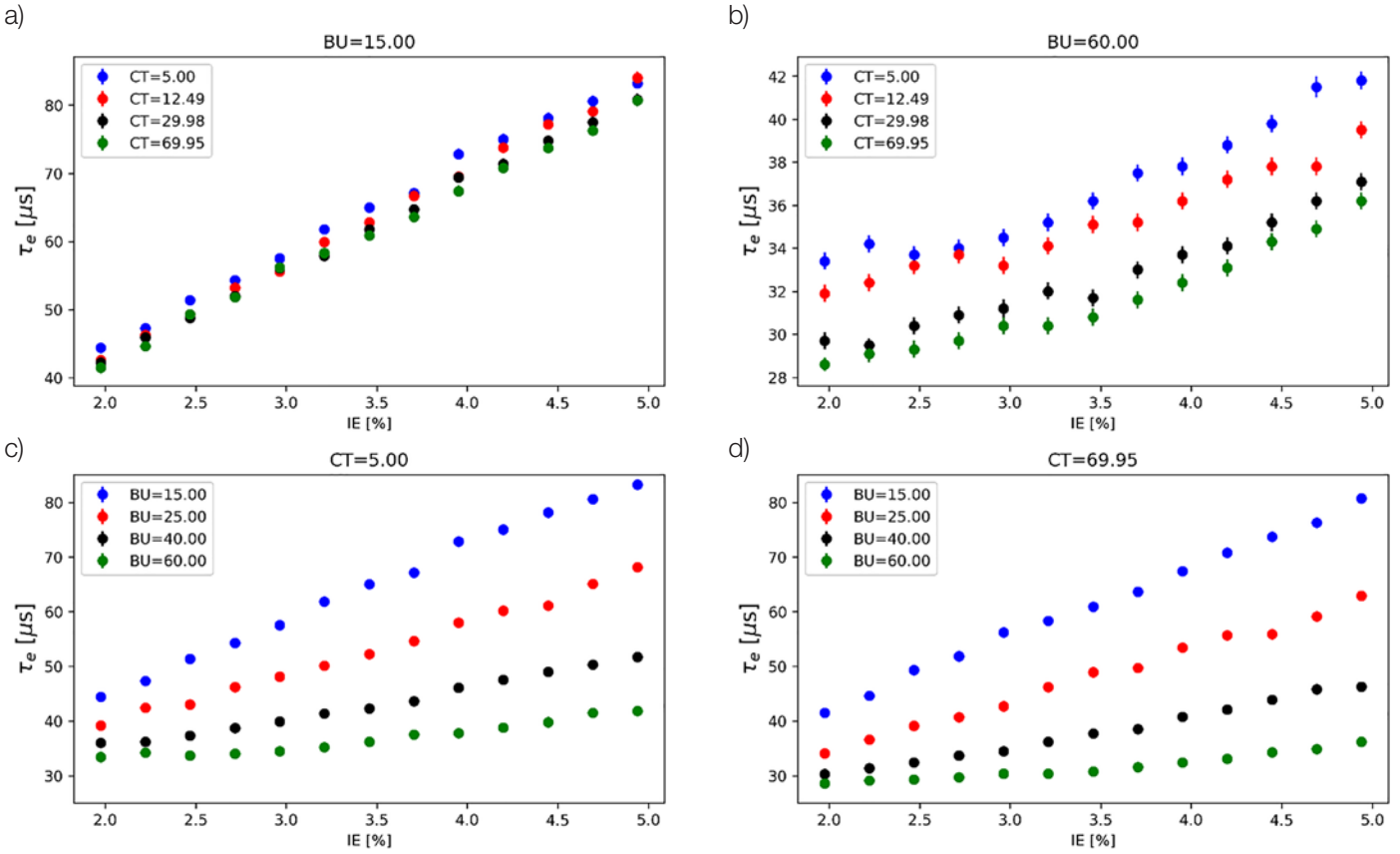

Figure 2: The τ dependence on IE, for low BU (a), high BU (b), low CT (c) and high CT (d). In the top figures, the colors indicate different CT, for the bottom figures it indicates different BU. For a more understandable figure, all simulated data points are not shown.

As can be seen from figures 2a-2d, there is a strong dependence of τ on IE. As expected, τ increases with increasing IE. Figures 2a-2b show that the IE dependence does not depend on CT, since the data sets corresponding to different CT are only separated by a constant offset depending on CT. Figures 2c-2d however show a noticeable effect of BU on the IE dependence, with an increasing slope for lower BU-values.

Similar conclusions can be drawn from figure 3. Figures 3a-3b show a similar shape of the τ-dependence

on BU independent of CT (only the constant offset is different), while figures 3c-3d show a dependence on IE where different IE-values give different slopes to the τ-dependence on BU.

Figure 4 shows that the CT-dependence can be described with an exponentially decreasing function, with figures 4a-4b showing that IE only affects a constant offset and not the exponential itself, and figures 4c-4d show the same but for BU. The different scales of the y-axis make it difficult to compare different subplots with each other, but one can note this effect also by comparing the different colors in each subfigure (they colored data sets only vary by a constant offset). This implies that the CT dependence, described by an exponential function, is independent of IE and BU except for a constant offset. Since the IE and BU dependencies are interconnected, it is more difficult to assess what functional form to use in order to describe them. However, the figures qualitatively tell us that τ increases with IE, with a steeper slope for low BU (e.g. figure 2c); and τ decreases with BU, with a slope that increases with higher IE and flattens out with BU (eg figure 3c).

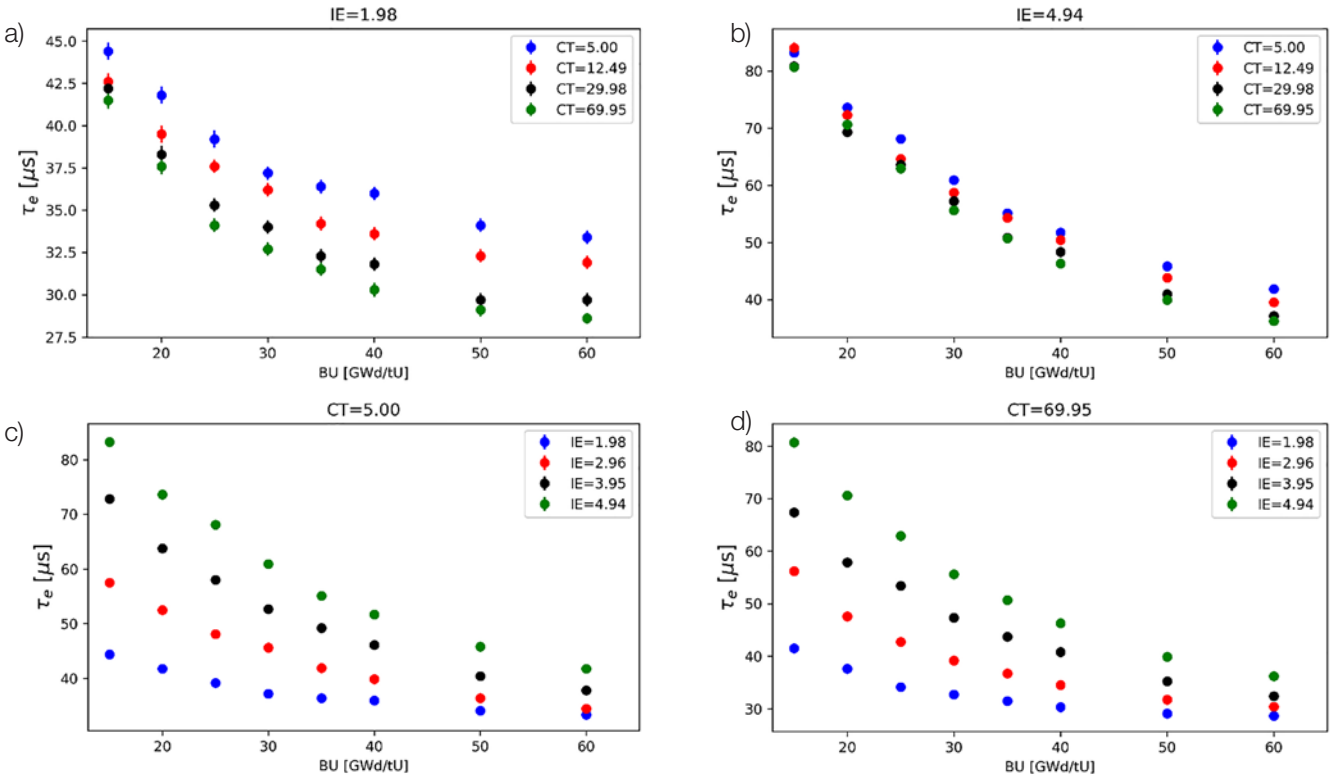

Figure 3: The τ dependence on BU, for low IE (a), high IE (b), low CT (c) and high CT (d). For the top figures, the colors indicate different CT, for the bottom figure it indicates different IE. For a more understandable figure, all simulated data points are not shown.

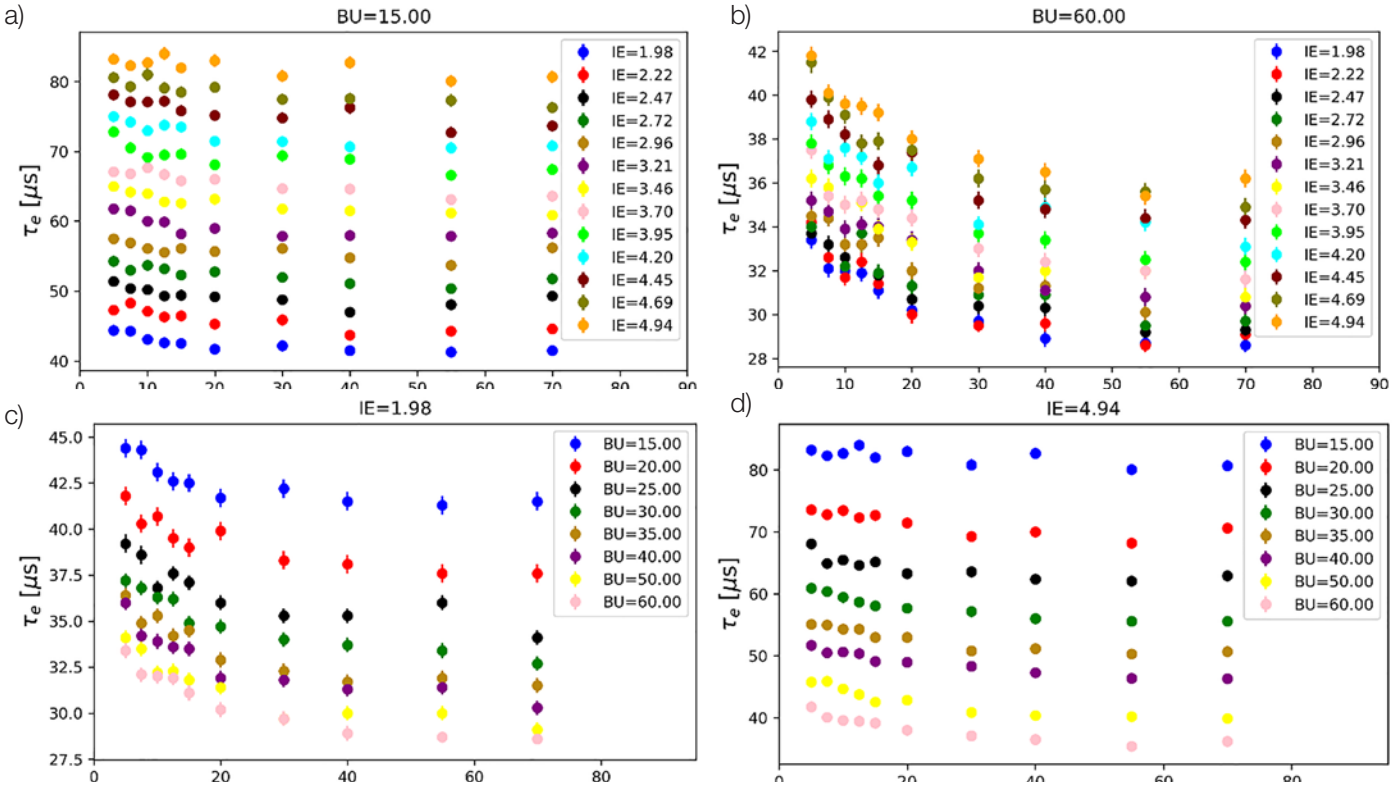

Figure 4: The τ dependence on CT, for low BU (a), high BU (b), low IE (c) and high IE (d). For the top figures, the colors indicate different IE, for the bottom figure the colors indicates different BU.

3.1 Physical considerations

As mentioned above, the early die-away time depends on the quantity of fissile material and neutron absorbers (such as some fission products) in the fuel. To understand which isotopes that are most important when determining τ, we have investigated three quantities in eight example fuels: i) the neutron absorption rate, ii) the neutron induced fission rate and iii) the rate of neutrons produced from fission. The eight example fuels have low and high CT, low and high BU and low and high IE. The respective rates were calculated using the MCNP6 F4 neutron flux tally score, multiplied with the relevant cross-sections. The isotopes where then ranked according to the absolute value of their net neutron emission rate, defined as the difference between the neutron emission rate from fission and the total neutron absorption, where total neutron absorption also includes neutrons lost to fission.

Looking at the top six isotopes for each of the eight example fuels, we find that the sixth isotope always has a net neutron emission which is at least one order of magnitude smaller than the first isotope. Table 1 shows the six top ranked isotopes for one of the eight fuels.

Isotope	Net neutron emission [au]
^{239}Pu	7.8
^{235}U	4.4
^{238}U	-4.2
^{241}Pu	2.4
^{240}Pu	-2.0
^{143}Nd	-0.51

Table 1: Net neutron emissions for an example fuel with IE=4.9%, BU=60 GWd/tU and CT=5y.

To reach a reduction in net neutron emission of two orders of magnitude, it was sometimes necessary to consider 30 ranked isotopes. In qualitatively understanding the impact of the different isotopes on τ, we focus here on eight isotopes that appear at least once in the top five list for the eight fuels: ^{239}Pu, ^{240}Pu, ^{241}Pu, ^{241}Am, ^{235}U, ^{238}U, ^{155}Gd and ^{149}Sm. The top 3 list is often consisting of ^{239}Pu, ^{235}U and ^{238}U. The following subsections give some insight into the mechanism governing τ and its dependence on IE, BU and CT. A more quantitative understanding is beyond the scope of this paper.

3.1.1 CT dependence of τ

From the list of isotopes above, the one isotope with a half-life likely to have a visible effect in the range of CT=5-70 y is ^{241}Pu ($t_{½}$ = 14.3 y). This isotope mainly β^--decays to ^{241}Am. While ^{241}Pu is fissile and has a positive contribution to the early die-away time (more ^{241}Pu gives a larger τ), ^{241}Am absorbs neutrons and has a low probability of fissioning, and thus has a negative contribution to τ. From these considerations, one would expect τ to follow an exponential decay law with CT, with a mean lifetime (the inverse of the exponential decay constant λ) smaller than that of ^{241}Pu, since the decay of ^{241}Pu creates ^{241}Am which lowers τ even more. This is indeed the result found in the study; the mean lifetime of ^{241}Pu is 20.6 y, and the mean lifetime obtained for τ in the fit in section 3.2.1 is 15.8 y (parameter *b* in table 3).

3.1.2 BU and IE dependence of τ

Since higher BU means that more fissile ^{235}U nuclei have been split, τ is expected to decrease with BU. The buildup of other fissile isotopes should offset this and slow down the decrease, while production of neutron poisons would speed up the decrease. Studying how the ^{235}U concentration changes as a function of burnup, we note that the rate of decrease of the ^{235}U concentration depends on the IE, with higher IE resulting in a sharper decrease of the ^{235}U concentration with increasing BU.

Figure 5 shows how the total fissile concentration (i.e. ^{235}U, ^{239}Pu and ^{241}Pu) changes with BU and IE. This dependence is very similar to the dependences observed for only ^{235}U, and this isotope is hence assumed to dominate the dependence. The dependences in figure 5 are qualitatively

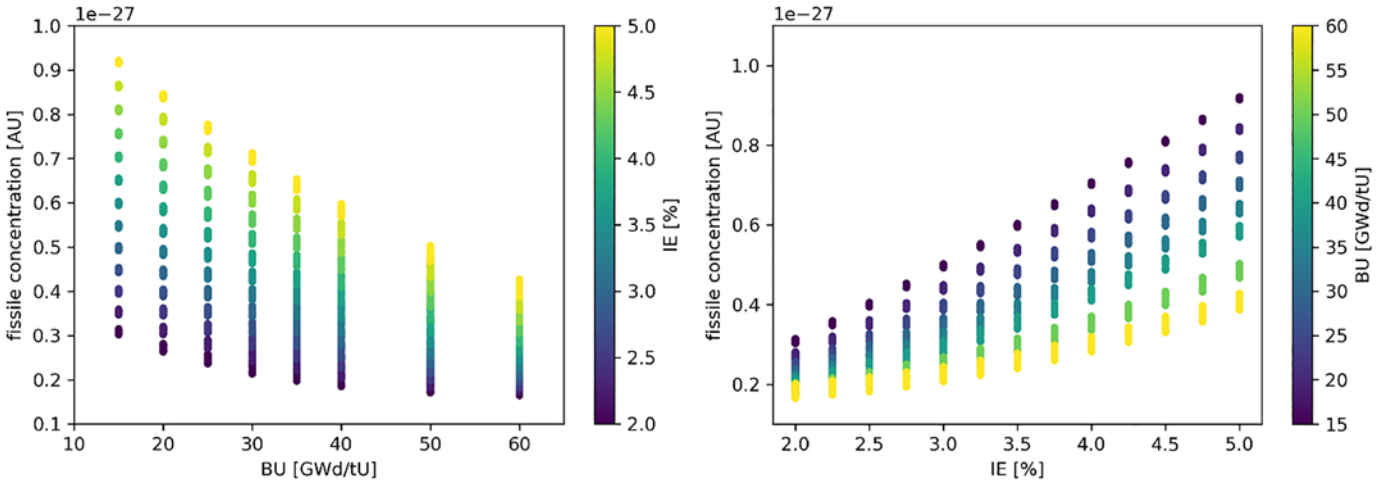

Figure 5: The concentration of fissile isotopes vs BU (left) and IE (right), colored with the IE (left) and BU (right).

very similar to the τ-dependence on these variables, so the contribution from ^{235}U seems to be the most important one. Higher IE, meaning more ^{235}U and less ^{238}U, is expected to give larger values of τ, as is also seen in figure 2. As BU increases, the fuel composition becomes more complex and varied and the increase of τ with IE slows down.

3.2 Fitting functions

Since the τ-dependence on CT seems to be independent of BU and IE, this was investigated first. The function describing the dependence of τ on CT was chosen to be an exponential function of the form

$$\tau = a \cdot e^{-\frac{CT}{b}} + c \quad (1)$$

where *a*, *b* and *c* are the fitting parameters. The choice of the exponential function is explained in section 3.1.1. One exponential function (each generating unique *a*, *b* and *c* parameter values) was fitted to each group of data points with one combination of IE and BU, e.g. each group with the same color in one subplot of figure 4. The fit parameters *a*, *b* and *c* are then analyzed with respect to their dependence on IE and BU. The dependences of the *a* and *c* parameters on BU and IE can be seen in figure 6; the dependence of the *b* parameter looks similar to the *a* dependence and is hence not shown.

Despite rather large statistical fluctuations in figure 6 (the error bars represent the statistical uncertainties in the fit), both the *a* and *b* parameters have been found to be consistent with a constant value. This means that these two parameters can be considered to be independent of IE and BU. The *c* parameter however displays the same trend as τ does for a fixed CT, also indicating that the BU and IE dependence of τ is captured by the *c*-parameter and not by the *a* or *b* parameters. With the ultimate goal of finding a function that describes how τ varies with IE, BU and CT, equation 1 was accordingly chosen with the *a* and *b* parameters constant for the whole range of IE and BU values, but with the *c* parameter replaced by a function that better captures the IE and BU dependences.

In the determination of the second function (capturing the dependence of the *c* parameter on BU and IE), a fit of equation 1 was performed to fix the *a* and *b* constants while allowing the *c* parameter to vary with BU and IE. Accordingly, a different *c* parameter value was obtained for each value of IE and BU.

Determining then the BU dependence first, and to avoid an unphysical increase of τ with BU values outside the fitting range, an exponential fit (Equation 2) was tried

$$c = a_1 \cdot e^{-\frac{BU}{b_1}} + c_1 \quad (2)$$

where a_1, b_1 and c_1 are the fit parameters that vary with IE. Since each fit, corresponding to one IE value, is associated with a unique determination of the parameters a_1, b_1 and c_1, a function can be used to describe how each parameter varies with IE. This function can be described by either a linear, quadratic or constant polynomial of IE. Figure 7 shows the variation of the parameter values with IE, together with a linear fit.

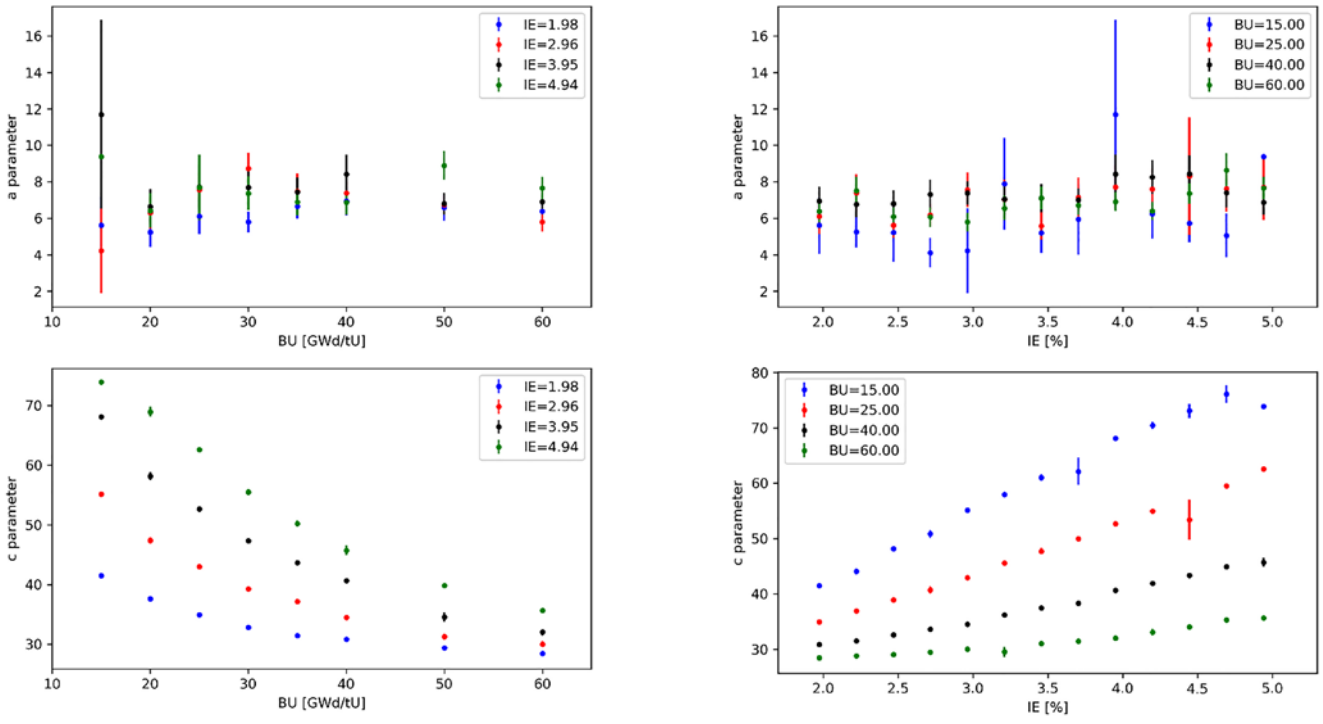

Figure 6: The *a* (upper row) and *c* (lower row) parameters resulting from an exponential fit of τ to CT, shown as a function of BU (left) and IE (right). The data points corresponding to BU=15 GWd/tU and IE=4,94% are plotted without error bars, since the error associated these points is so large that they obscure all other trends. For a more understandable figure, all simulated data points are not shown.

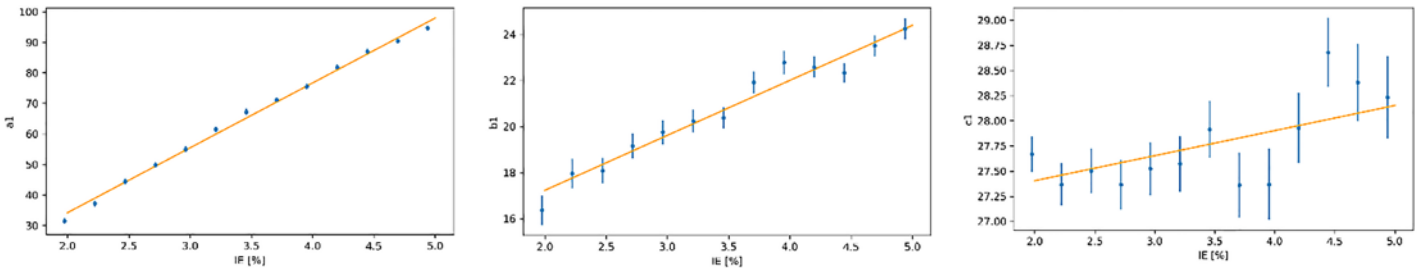

Figure 7: The dependence of the parameters a_1, b_1 and c_1 of the BU fit (equation 2) on IE. The fitted function is linear in all three cases, although table 2 shows that this does not always give the best fit.

Table 2 shows the resulting χ^2 and χ^2 probability values for different functions describing the variation of the a_1, b_1 and c_1 parameters with IE. Table 2 tells us that the a_1 parameter is best described by a function that depends quadratically on IE, the b_1-parameter is best described by a linear function of IE (although the quadratic function is almost equally good), and that the c_1 parameter is best described by a quadratic function (but a linear function is still relevant to try in a global fit).

Parameter	Fit type	χ^2	χ^2 probability
a_1	Linear	25.7	0.007
	Quadratic	5.2	0.88
b_1	Linear	10.7	0.45
	Quadratic	8.6	0.57
c_1	Linear	12.6	0.32
	Quadratic	8.0	0.62
	Constant	21.3	0.04

Table 2: Fit statistics for the BU parameters a_1, b_1 and c_1 as functions of IE.

3.2.1 Global fit

Following the considerations above, several functions were tried in order to find a suitable function for a global fit, that simultaneously describes the dependence of τ on CT, BU and IE. All the functions which were tried, make use of equation 1 but with parameter c replaced by a function C, as shown in equation 3:

$$\tau = a \cdot e^{-\frac{CT}{b}} + C \tag{3}$$

Many different functions C were tried and assessed, the best function as determined by the resulting χ^2 value is shown in equations 4-7

$$C = c' \cdot e^{-\frac{BU}{d}} + e \tag{4}$$

$$c' = \left(c_2 \cdot IE^2 + c_1 \cdot IE + c_0\right) \tag{5}$$

$$d = \left(d_2 \cdot IE^2 + d_1 \cdot IE + d_0\right) \tag{6}$$

$$e = \left(e_2 \cdot IE^2 + e_1 \cdot IE + e_0\right) \tag{7}$$

The resulting parameter values are shown in table 3. This fit has $\chi^2 = 1245$ and χ^2 probability $3.9 \cdot 10^{-6}$. The errors are probably underestimated, leading to this large value of χ^2, and a better error estimate is under consideration.

Figure 8 shows the τ value determined using the parametrization versus the τ value determined using the MCNP simulations, together with the line representing a perfect fit. As can be understood, the global parametrization function seems to work quite well.

Parameter	Value
a	6.87(8)
b	15.8(4)
c0	-28(3)
c1	33(2)
c2	-1.8(2)
d0	11(1)
d1	3.3(7)
d2	-0.14(10)
e0	28.2(6)
e1	-0.7(4)
e2	0.14(7)

Table 3: Fit parameters determined for the best global fit.

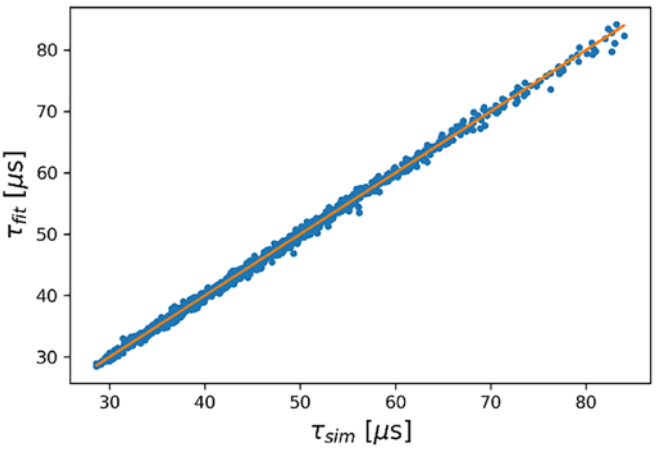

Figure 8: The τ values determined from the parametrization versus those obtained from a full-scale MCNP6 modelling together with a line indicating a perfect match.

4. Test of parametrization

The parametrization has been tested on a separate set of modelled data. The data set comprises 980 simulated PWR fuels, with depletion calculations done using Serpent2 as described in section 2. However, the ranges of IE, BU and CT were slightly different from the fuels described earlier. IE ranged from 2-5% atomic weight in steps of 0.5%, while BU and CT were randomly selected with a uniform probability in the intervals 15-50 GWd/tU and 5-70 y, respectively. Figure 9 shows the early die-away time τ determined using the parametrization versus determination using MCNP, as well as the normalized residuals $r_n = \frac{\tau_{fit} - \tau_{sim}}{\sigma_{\tau_{sim}}}$, centered around zero.

The root mean squared error (RMSE) is 0.57 μs, χ^2 = 1131 and the χ^2 probability $5.4 \cdot 10^{-4}$. As previously mentioned, the errors are probably underestimated, leading to a larger value of χ^2 than is to be expected, but this remains to be investigated.

5. Conclusion and Outlook

This paper describes a way to estimate the early die-away time τ from the DDSI prototype instrument, as a way to avoid the computationally demanding MCNP simulations that are usually performed. This can be specifically useful when die-away times for large number of fuel assemblies are required, such as in the case of training machine learning models.

Our work shows that in the case of modelled PWR 17x17 fuel assemblies, the CT dependence of the early die-away time can be decoupled from the BU and IE dependencies. The research also suggested that the CT dependence of τ follows an exponential decay. In this work it was decided to, in the second step, describe the BU dependence and thirdly the IE dependence. The reverse order was tried, although the results are not shown in this paper, and the results were similar to those obtained here but not as good. The BU dependence could be best described using another exponential decay, although other functions with a similar fall-off were found to also work well. The IE-dependence was finally captured using functions with a quadratic dependence on this parameter.

The die-away times estimated using the resulting parametrization function were compared to the accurate estimations using MCNP6 modelling and a fit to the Rossi-alpha distribution, and the agreement was shown to be very good, also for the case of a new data set of modelled fuel assemblies with a slightly different set of fuel parameters (within the same range as the first one). As an important next step, an experimental validation of this parametrization is planned, since the ability of the parametrizing function to estimate the DDSI die-away time for commercial reactor fuel might be significantly influenced by a deviation of burnup, initial enrichment and cooling time from the assumed ideal case. Furthermore, it is important to study to what extent the parametrization function also correctly estimates the die-away time for other fuel types or designs.

6. Acknowledgements

We would like to acknowledge the financial support from the Swedish Radiation Safety Authority under contracts SSM2016-661, SSM2015-4125 and SSM2016-4600.

The authors would also like to thank Dr. Alexis Trahan at Los Alamos National Laboratory for her kind assistance with respect to DDSI modelling.

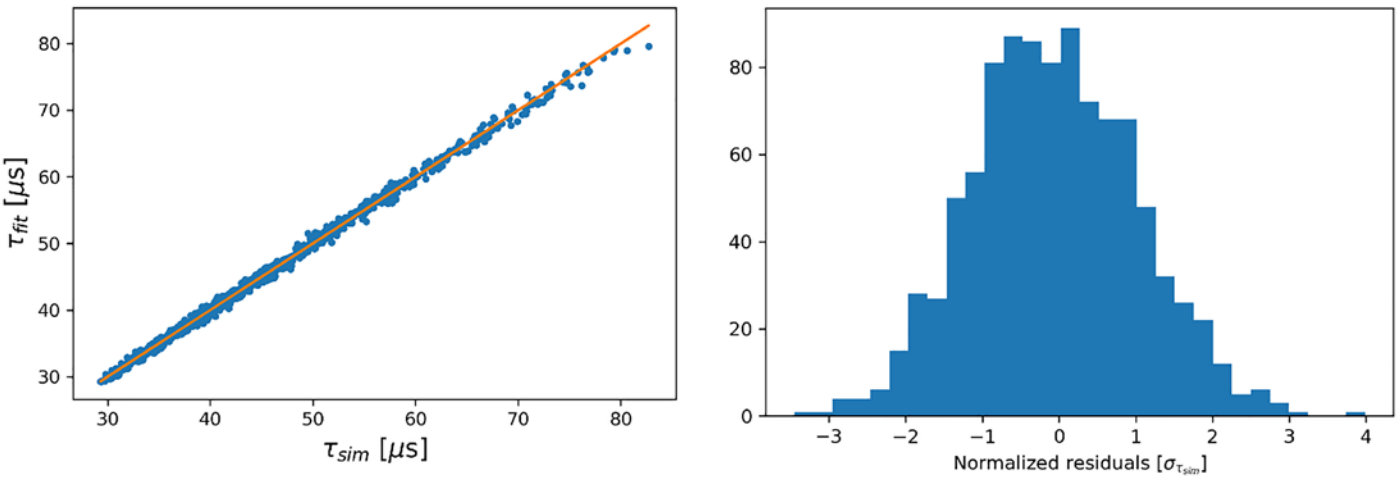

Figure 9: The simulated and calculated values of τ for the test data fall close to the line indicating a perfect match (left). The normalized residuals are shown in the right figure.

7. References

[1] A. Trahan. “Utilization of the Differential Die-Away Self-Interrogation Technique for Characterization and Verification of Spent Nuclear Fuel”. PhD thesis. University of Michigan, 2016.

[2] M. A. Humphrey, S. T. Tobin, and K. D. Veal. “The Next Generation Safeguards Initiative’s Spent Fuel Nondestructive Assay Project”. In: Journal of Nuclear Material Management 40 (2012), pp. 6-11.

[3] A. Trahan, G. McMath, P. Mendoza, H. Trellue, U. Backstrom, and A. Sjöland. “Preliminary Results from the Spent Nuclear Fuel Assembly Field Trials with the Differential Die-Away Self-Interrogation Instrument”. In: Proceedings of the Institute of Nuclear Materials Management 59th Annual Meeting, July 22-26, Baltimore, Maryland. Institute of Nuclear Materials Management. 2018.

[4] A. C. Kaplan, V. Henzl, H. O. Menlove, M. T. Swinhoe, A. P. Belian, M. Flaska, and S. A. Pozzi. “Determination of spent nuclear fuel assembly multiplication with the differential die-away self-interrogation instrument”. In: Nuclear Instruments and Methods in Physics Research Section A: Accelerators, Spectrometers, Detectors and Associated Equipment 757 (2014), pp. 20-27.

[5] A. C. Trahan, A. P. Belian, M. T. Swinhoe, H. O. Menlove, M. Flaska, and S. A. Pozzi. “Fresh Fuel Measurements with the Differential Die-Away Self-Interrogation Instrument”. In: IEEE Transactions on Nuclear Science 64.7 (2017), pp. 1664-1669.

[6] J. Leppänen, M. Pusa, T. Viitanen, V. Valtavirta, and T. Kaltiaisenaho. “The Serpent Monte Carlo code: Status, development and applications in 2013”. In: Annals of Nuclear Energy 82 (2015), pp. 142-150.

[7] T. Goorley et al. “Initial MCNP6 Release Overview”. In: Nuclear Technology 180.3 (2012), pp. 298-315.

[8] L. Caldeira Balkeståhl, Z. Elter, S. Grape, and C. Hellesen. “MCNP simulations of prototype DDSI detector”. In: Proceedings of the International Workshop on Numerical Modelling of NDA Instrumentation and Methods for Nuclear Safeguards (NM-NDA-IMNS18). ESARDA. 2018.

Use of machine learning models for the detection of fuel pin replacement in spent fuel assemblies

Riccardo Rossa, Alessandro Borella
SCK•CEN Belgian Nuclear Research Centre
Boeretang 200 – 2400 Mol, Belgium
E-mail: rrossa@sckcen.be

Abstract:

The nuclear material contained in the spent fuel assemblies represents the majority of the material verified during the safeguards inspections, and the replacement of spent fuel pins from an assembly is one of the possible scenarios to divert nuclear material.

Due to the high number of fuel pins contained in a fuel assembly (e.g. 264 pins in a PWR 17x17 geometry), a practically infinite number of diversion scenarios can be considered by a potential proliferator. In this framework, Monte Carlo simulations were used to model some of the possible diversion scenarios and to develop a database of detector responses corresponding to different non-destructive assay (NDA) techniques. In addition, the database contains the detector responses obtained with complete fuel assemblies with different initial enrichment, burnup, and cooling time.

Given the large size of the database and the multiple detector responses resulting from the NDA techniques, the use of machine learning is proposed for the data analysis. In this work we focus on the classification problem with the aim of classifying the diversion scenarios based on the percentage of replaced pins. Several machine learning models were developed for this problem using decision trees, discriminant analysis, support vector machine, and nearest neighbors algorithms. The accuracy of the models was calculated as the number of correct classifications in the whole dataset.

The results from the study show that the selection of the detector type used as input in the machine learning model has a strong impact on the accuracy of the developed model. In general the use of gamma-ray detectors leads to higher accuracies compared to the use of neutron detector responses. In addition, several machine learning models achieved a complete correct classification.

Keywords: Machine learning, fuel diversion, Monte Carlo, spent fuel, non-destructive assays

1. Introduction

As defined in the INFCIRC/153 [1] the technical objective of safeguards is the timely detection of diversion of significant quantities of nuclear material. The nuclear material contained in the spent fuel assemblies represents the majority of the material verified during the safeguards inspections [2], and the replacement of spent fuel pins from an assembly is one of the possible scenarios to divert nuclear material.

The capabilities to detect a subset of missing or replaced spent fuel pins, the so-called partial defect testing, were assessed in the past for the Fork detector [3]. In addition, several non-destructive assay (NDA) techniques are proposed to improve the current capabilities for partial defect testing [4], [5]. Among others NDA techniques, the Self-Indication Neutron Resonance Densitometry (SINRD) and the Partial Defect Tester (PDET) have been investigated in the past years at SCK•CEN [6].

Given the large number of diversion scenarios that can be developed and the multiple detector responses resulting from the two NDA techniques, the use of machine learning [7] is proposed for the data analysis as alternative to a previous approach chosen in recent work [8]. Due also to the continuous increase in the computer power, machine learning is extensively used in many fields where large amount of data is available [9], [10]. Within SCK•CEN, research on machine learning applied to the safeguards field focused so far on the use of artificial neural networks (ANN) for the determination of initial enrichment, burnup, and cooling time of spent fuel assemblies [11].

In this contribution the NDA technique chosen for the study is described in Section 2, whereas the overview of the Monte Carlo simulations is presented in Section 3, and the description of the machine learning models is included in Section 4. The results from the data analysis are discussed in Section 5, followed by the conclusion and outlook for future work in Section 6.

2. Description of the NDA technique

2.1 Models geometry

The NDA technique chosen for this study stems from the Self-Indication Neutron Resonance Densitometry (SINRD) and the Partial Defect Tester (PDET).

The SINRD technique is a passive NDA technique that was originally developed by LANL based on the passive

neutron emission from spent fuel due to spontaneous fissions and (α,n) reactions [12]. The principle of the SINRD technique is to measure the attenuation of the neutron flux in the 0.3 eV energy region to obtain a direct estimation of the ^{239}Pu content in the spent fuel. The technique has been studied for the measurement of spent fuel underwater at LANL [13], [14], [15], whereas a measurement approach in air has been investigated at SCK•CEN [16], [6]. Previous research [6] indicated that the use of ^{239}Pu fission chambers increased the sensitivity to the ^{239}Pu content in the spent fuel. In addition, the fast neutron flux was measured with ^{238}U fission chambers according to the approach developed at SCK•CEN.

The Partial Defect Tester (PDET) is a NDA technique that measures the passive neutron and gamma emission from the fuel assembly by inserting a set of small detectors in the guide tubes of a PWR fuel assembly [17], [18], [19]. The PDET was originally proposed by LLNL with the aim of detecting partial defects, and a PDET prototype has been built and tested in a measurement campaign at the Swedish Interim Storage Facility CLAB in January 2015 [20]. The total neutron flux was measured with ^{235}U fission chambers, whereas the gamma-ray flux was measured with ionization chambers.

The NDA detector setup adopted in this study is shown in Figure 1 for both measurements in air and in fresh water. A thick slab of polyethylene surrounds the fuel assembly during the measurement in air (left side of Figure 1) to ensure neutron moderation. The PWR 17x17 fuel assembly geometry was considered in all simulations.

The detector types considered for the SINRD technique and those used by PDET are combined in the NDA technique proposed for this study, and the details of the detector responses are described in Section 2.2. The detectors positions include the guide tubes (red and yellow positions in Figure 1) as in the approach proposed for the PDET detector, but also additional detectors are placed around the fuel assembly (green positions).

2.2 Detector responses

The detector responses were calculated from the results of the Monte Carlo simulations and following the approach proposed in [6]. As shown in Figure 1, for both measurement in air and in fresh water the detector positions and the detector types are identical. The calculated detector responses include:

- Thermal neutrons (TH): bare ^{235}U fission chamber;
- Fast neutrons (FAST): bare ^{238}U fission chamber;
- Resonance region neutrons (RES): difference between the neutron counts with a ^{239}Pu fission chamber covered by Gd foil and a ^{239}Pu fission chamber covered by Cd foil;
- Gamma-rays (P): ionization chamber.

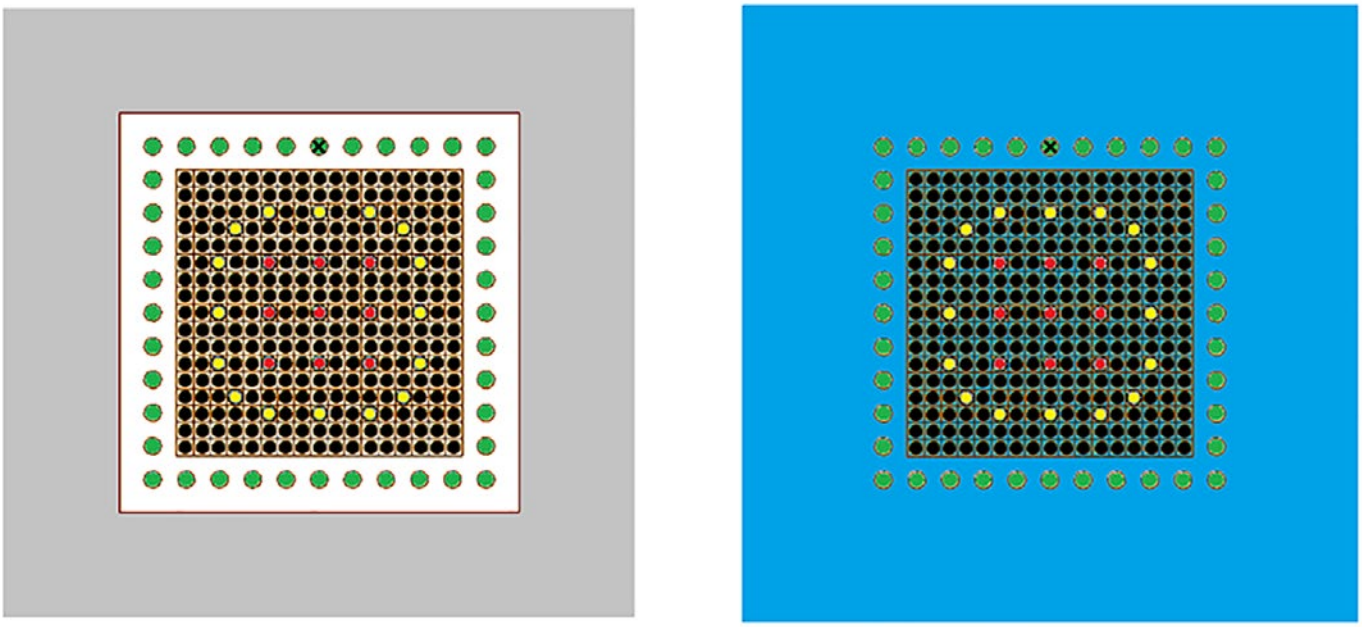

Figure 1: Monte Carlo models of the detector setups chosen in this study. The PWR 17x17 fuel assembly is represented with the fuel pins shown in black. The positions of the detectors are depicted in red, yellow, and green. The detector responses are normalized to the value obtained for the detector position marked with a cross. The picture on the left shows the setup for the measurement in air, with the polyethylene slab in grey surrounding the fuel assembly, and the picture on the right shows the setup for the measurement in fresh water (depicted in blue).

3. Overview of the Monte Carlo simulations

3.1 Complete fuel assemblies

The same set of Monte Carlo simulations was performed both for the NDA technique in air and in fresh water. From each simulation the detector responses were normalized to the value obtained for the detector marked with a cross in Figure 1. The average value was then calculated for the nine central guide tube positions, the sixteen peripheral guide tube positions, and the forty detector positions outside the fuel assembly. The choice to normalize the detector responses followed the approach for the PDET detector where the detector responses are normalized to one detector position [18]. In this way the range of values of the normalized detector responses is greatly reduced compared to the range of the un-normalized detector responses. Future work will consider as input the detector responses before the normalization and will estimate the influence of this step in the accuracy of the machine learning models.

A first set of simulations was performed with complete fuel assemblies, i.e. assemblies with all the fuel pins with equal material composition and source strength, considering different values of:

- Initial enrichment: 2.0, 2.5, 3.0, 3.5, 4.0, 4.5, 5.0%;
- Burnup: 5, 10, 15, 20, 30, 40, 60 GWd/t_{HM};
- Cooling time: 1, 5, 10, 50 years.

A total of 196 simulations resulted from all combinations of these parameters. The aim of these simulations is to assess the influence of the fuel irradiation history on the calculated

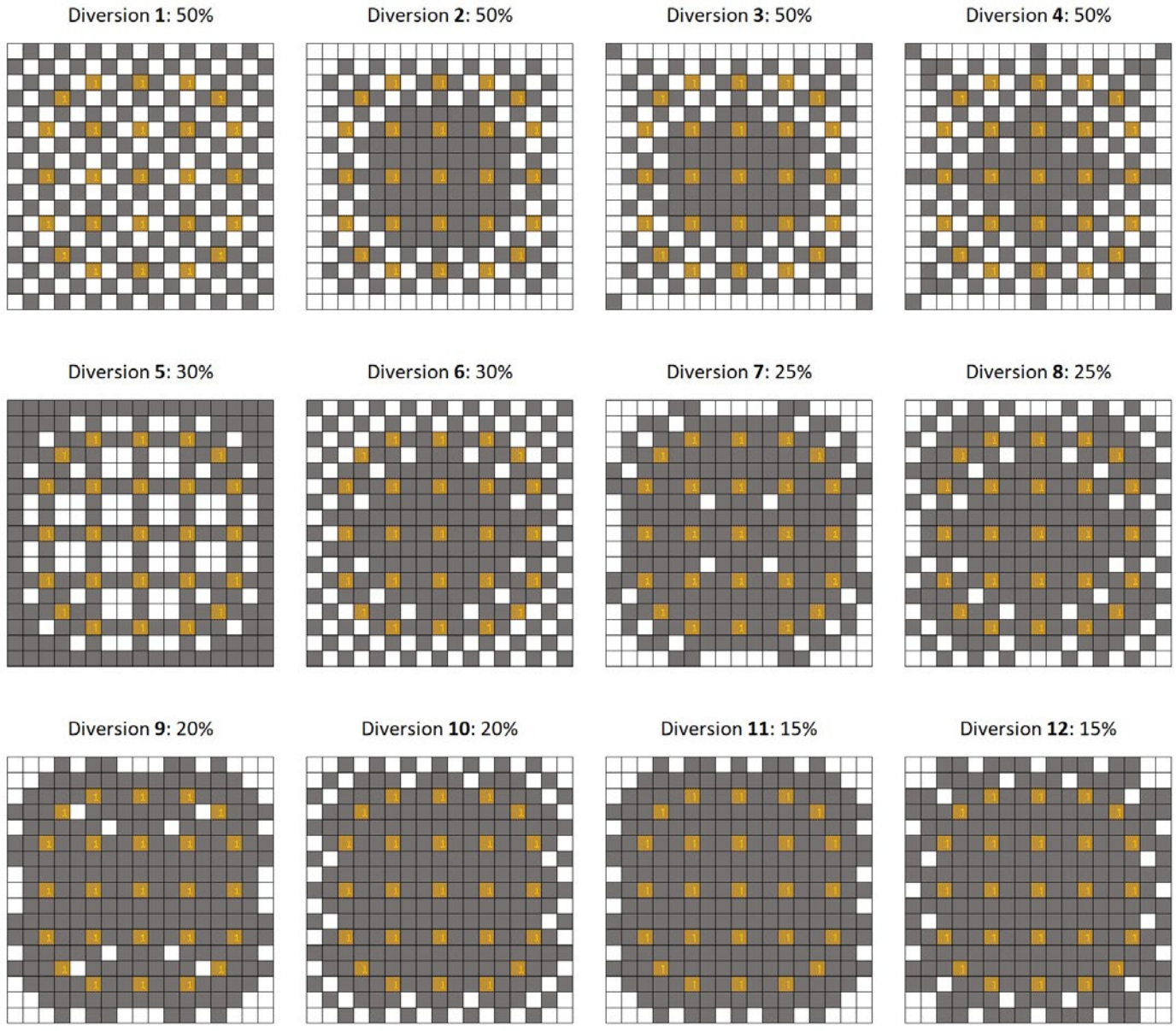

Figure 2: Overview of the diversions scenarios considered in this study. The fuel pins are marked in grey, the dummy pins in white, and the guide tube positions in yellow. The percentage of dummy pins is mentioned for each scenario.

detector responses. The fuel composition and source strength were taken from the SCK•CEN reference spent fuel library [21]. This library did not contain fuel assemblies with burnable poisons; therefore, the impact of this design characteristic could not be estimated at this stage.

3.2 Diversion scenarios

A second set of simulations considered twelve diversion scenarios, where some of the spent fuel pins were replaced by dummies made of stainless steel. The remaining spent fuel pins had equal material composition and source strength as in the case for complete fuel assemblies, whereas no source term was included in the dummy pins. The scenario with pin replacement is expected to be more difficult to detect compared to the case of diversion without replacement.

The diversion scenarios are shown in Figure 2 and they cover cases with replacement between 50% and 15% of the total number of fuel pins. The fuel pins are depicted in grey, the dummy pins in white, and the guide tube positions in yellow. Most of the replacement occurs on the outer region of the fuel assembly, but also a chess-board pattern (Diversion 1) and diversion from the inner section of the fuel assembly (Diversion 5) are included.

All simulations concerning the diversion scenarios considered fuel with a cooling time of 5 years, but the influence of the irradiation history was taken into account simulating fuel with different values of:

- Initial enrichment: 2.0, 3.5, 5.0%;
- Burnup: 10, 30, 60 GWd/t_{HM}.

A total of 108 simulations were carried out in this set of simulations.

4. Machine learning models used for the data analysis

4.1 Introduction to machine learning

Machine learning is used nowadays for a broad range of applications such as speech recognition, financial fraud detection, and cancer prognosis. [22], [23], [24], [25], [26]

The machine learning models can be divided into two broad categories of supervised and unsupervised learning [27]. In the case of supervised learning the observations in the dataset have associated output values, whereas in the case of unsupervised learning the input data do not have corresponding output values.

A machine learning model for supervised learning is first developed during the training phase on a set of known input and output data. Once the model is trained, it is used to predict (prediction phase) new input data for which the output data is unknown. The generic workflow for supervised learning is shown in Figure 3. The machine learning model developed by supervised learning uses regression or classification techniques depending on the type of output data. Regression techniques are used to predict output data that can assume continuous values (e.g. changes in temperature or pressure, fluctuations in housing prices), whereas classification techniques are used to classify input data into categories that can assume only a limited set of values (e.g. type of fruit, benign/malign tumor). [9]

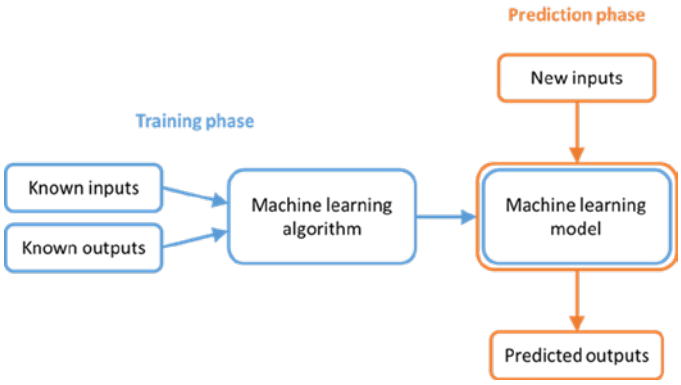

Figure 3: Generic workflow in case of supervised learning. The development of the machine learning model from known inputs and outputs is indicated as training phase, whereas the prediction of outputs from new inputs is referred to as prediction phase.

Independently from the machine learning algorithm chosen, the data needed to develop a machine learning model is generally organized in a database. According to the machine learning terminology the records in the database are called observations and the input variables are called features or predictors. In case of supervised learning the output variables are called responses. Specific to classification techniques, the responses can assume only a finite set of values (either in numerical or text format) called classes.

The detector responses calculated with the Monte Carlo simulations described in Section 3 were organized in a database where the normalized average detector responses were the features and the percentage of replaced pins represented the response. Six classes were defined for the response, representing 50, 30, 25, 20, 15, and 0% of replaced pins. Therefore, each observation in the database consisted in 12 features and 1 response. An extract of the database for the NDA technique with the fuel assembly in air is shown in Table 1; the same database structure was used for the data with the fuel assembly in fresh water. Since each observation in the training database contained the corresponding response class, the detection of fuel pins diversion was treated as a supervised machine learning problem to be solved with classification techniques.

The accuracy of the models was calculated as the number of correct classifications in the whole dataset, and this metric was used to compare the different machine learning models developed.

Features												Resp.
Central det. positions				Peripheral det. positions				External det. positions				
TH	FA	RES	P	TH	FA	RES	P	TH	FA	RES	P	
0.35	1.85	0.40	2.09	0.52	1.64	0.56	1.91	1.10	0.86	1.04	0.85	0
0.34	1.85	0.35	2.09	0.51	1.64	0.51	1.91	1.10	0.86	1.05	0.85	0
0.34	1.86	0.32	2.09	0.51	1.64	0.48	1.91	1.10	0.86	1.06	0.85	0
0.34	1.86	0.30	2.09	0.51	1.64	0.47	1.91	1.10	0.86	1.06	0.85	0
0.33	1.87	0.28	2.08	0.51	1.65	0.45	1.91	1.10	0.86	1.06	0.85	0

Table 1: Extract of the training database for the NDA technique with the fuel assembly in air.

4.2 Parameters chosen for the machine learning models

The machine learning models for this study were developed using the Classification Learner App that is part of the MATLAB Statistics and Machine Learning Toolbox [28].

The toolbox offers the choice of several machine learning algorithms that can be used for supervised and unsupervised learning problems. The Classification Learner App has a graphical user interface (GUI) that allows the user to select in the first window the training database, the variables to be used as features, and those to be used as responses.

The selection of the validation scheme used to assess the accuracy of the developed model is the next step in the GUI. The default MATLAB 5-fold cross-validation approach was chosen, where the training database is divided into five equal-sized subsections. As noted in [28], the validation scheme is used only for the estimation of the model accuracy; the final model is always trained using the complete training database.

The next section in the GUI is the selection of the model type and model parameters, and the training of the model. Four main families of machine learning models were used for the data analysis: decision trees, discriminant analysis, support vector machines, and nearest neighbors classifiers. The principles of the models are described extensively in literature [28], [22], [9], [29], [30], [31]. The parameters used for each developed model are listed in Tables 2-5.

Model name	Maximum number of splits	Split criterion	Surrogate decision splits
Simple tree	5	Gini's diversity index	Off
Medium tree	10	Gini's diversity index	Off
Complex tree	30	Gini's diversity index	Off

Table 2: Parameters chosen for the decision trees models.

Model name	Function used to separate classes	Covariance matrix
Linear discriminant	Linear	Diagonal
Quadratic discriminant	Quadratic	Diagonal

Table 3: Parameters chosen for the discriminant analysis models.

Model name	Kernel function	Box constraint level	Kernel scale mode	Manual kernel scale	Multiclass method	Standardize data
Linear SVM	Linear	1	Auto	------	1-vs-1	Yes
Quadratic SVM	Quadratic	1	Auto	------	1-vs-1	Yes
Cubic SVM	Cubic	1	Auto	-----	1-vs-1	Yes
Coarse Gaussian SVM	Gaussian	1	Manual	4	1-vs-1	Yes
Medium Gaussian SVM	Gaussian	1	Manual	1	1-vs-1	Yes
Fine Gaussian SVM	Gaussian	1	Manual	0.25	1-vs-1	Yes

Table 4: Parameters chosen for the support vector machine models. In the first three models the kernel scale mode was set to Auto, so the option Manual kernel scale was not used.

Model name	Number of neighbors	Distance metric	Distance weight	Standardize data
Coarse kNN	100	Euclidean	Equal	Yes
Medium kNN	10	Euclidean	Equal	Yes
Fine kNN	1	Euclidean	Equal	Yes
Cosine kNN	10	Cosine	Equal	Yes
Cubic kNN	10	Minkowski (cubic)	Equal	Yes
Weighted kNN	10	Euclidean	Squared inverse	Yes

Table 5: Parameters chosen for the nearest neighbors models.

5. Results

5.1 NDA technique with fuel assembly in air

The classifier models described in Section 4.2 were applied to the detector responses for the NDA technique with the fuel assembly in air. The accuracies of all models developed using as features the detector responses from the external detector positions are shown in Table 6, whereas the results obtained using all input features are shown in Table 7. These results were selected because they represent the lowest and highest accuracies among the models developed.

The rows of Tables 6-7 indicate the names of the machine learning models, whereas the columns indicate the normalized detector responses used for the analysis. As described in Section 2.2 the detector responses refer to neutron detectors sensitive to the thermal (TH), resonance (RES), or fast (FA) energy regions, and to the total gamma-ray emission (P). One or more detector responses were considered in the analysis and are included in the table. In Table 6 only one feature per detector response was used, namely the average detector response from the detectors in the external positions. In Table 7 three separate features were used for each detector response, corresponding to the average values from the detectors in the central, peripheral, and external positions, respectively. The values included in the table are the accuracy of each model, which is defined as the percentage of observations with correct classification. It was not possible at this stage to estimate the uncertainty of the calculated accuracy, but this topic will be addressed in future work.

The results of Table 6 indicate that the selection of the features used as input variable in the model is important to obtain a reliable classification, and in general the use of the gamma-ray detector response leads to higher accuracy of the model compared to other detector types. This result is in line with previous research [8]. However, the addition of multiple features does not strongly improve the accuracy of the model in most of the cases.

Once the features used in the model are chosen, similar accuracies were obtained for most of the machine learning models applied in this study. However, “Linear discriminant”, “Coarse kNN”, and “Cosine kNN” models showed several cases where the accuracy was lower than 75%. Complete correct classifications were reached for the “Complex tree”, “Fine Gaussian SVM”, “Fine kNN”, and “Weighted kNN” models when the gamma-ray detector response (P) was used as feature alone or in combination with the fast neutron detector response (FA).

The accuracies calculated for the machine learning models using the detector responses from all positions (i.e. central, peripheral, and external) are included in Table 7. Most of the conclusions drawn from the results in Table 6 are also applicable for Table 7, but in general the use of the detector responses from all available positions lead to an increase in the model accuracy. The largest accuracies are obtained using the responses of detectors sensitive to fast neutrons or gamma-rays. Accuracies lower than 75% were obtained for all cases using “Fine Gaussian SVM” and “Coarse kNN” models except when the feature used was only the fast neutron detector response (FA) or the gamma-ray detector response (P). Complete correct classifications were reached for several models, usually when the gamma-ray detector response (P) was used as feature either alone or in combination with other features.

5.2 NDA technique with the fuel assembly in fresh water

Machine learning models based on the parameters described in Section 4.2 were also developed from the detector responses of the NDA technique with the fuel assembly in fresh water. The accuracy for each model was computed and compared to the accuracy of the corresponding model developed for the NDA technique with the fuel assembly in air. Tables 8-9 show the accuracy calculated using the detector responses from the external positions or from all positions, respectively.

The results in the tables show that in most of the cases the accuracy calculated for the fuel assembly kept either in air or in fresh water is within ±5%. Therefore, the comments reported in Section 5.1 are also valid in this Section. Focusing on the cases where the difference in accuracy is larger than 5%, the accuracy for the NDA technique with the fuel assembly in fresh water is generally higher than the corresponding value obtained with the fuel assembly in air. This is observed in Table 8 when the responses of detectors sensitive to thermal neutrons (TH) or resonance region neutrons (RES) are used as features alone or in combination. On the contrary, a decrease between 5 and 10% was observed for several models when the responses of detectors sensitive to resonance region neutrons (RES) or fast neutrons (FA) are both used as features. Complete correct classifications were achieved using the “Fine Gaussian SVM” model with the (FA,P) features, the “Fine kNN” model using the (FA,P), (TH,FA,P), and (RES,FA,P) features, and the “Weighted kNN” model using the (FA,P) feature.

It is worth to note that for the NDA technique with the fuel assembly in fresh water no detector response alone is able to reach a complete correct classification using the detector positions located outside the fuel assembly. This is in contrast to the results obtained for the fuel assembly stored in air, where the gamma-ray detector response reached a complete correct classification with several machine learning models. The results obtained for the NDA technique with the fuel assembly in air are remarkable in the sense that they indicate that a passive gamma measurement in air has the potential for a complete correct

classification. In addition, if neutron detectors such as fission chambers are not needed, it would significantly simplify the design of a measurement device for spent fuel assay.

However, a safeguards verification underwater, like the one based on the PDET approach, is probably more realistic than a measurement in air, like the one based on the SINRD approach.

Hence future work will be targeted at improving the accuracy of the current models to reach a complete correct classification also for the NDA technique with the fuel assembly in fresh water.

Considering the accuracies calculated using all detector positions in Table 9, the largest difference between the NDA technique with the fuel assembly either in air or in fresh water were obtained using as input features the responses of detectors sensitive to thermal neutrons (TH) or resonance neutrons (RES) either alone or in combinations. An increase between 5 and 10% of the accuracy calculated with the fuel assembly in fresh water was obtained for decision tree and discriminant analysis models, whereas a decrease between -5% and -10% was obtained for “Linear SVM”, “Quadratic SVM”, and “Cubic SVM” models. Several models reached a complete correct classification using the NDA technique with the fuel stored in fresh water, especially when the gamma-ray detector response (P) was used alone or in combinations with other detector responses.

Detector positions considered: external (1 feature per detector response)															
Detector response 1	TH	RES	FA	P	TH	TH	TH	RES	RES	FA	TH	TH	TH	RES	TH
Detector response 2					RES	FA	P	FA	P	P	RES	RES	FA	FA	RES
Detector response 3											FA	P	P	P	FA
Detector response 4															P
Simple tree	67.8	70.1	83.9	84.9	72.0	82.9	85.9	82.2	84.5	86.2	84.5	83.6	87.2	88.8	87.2
Medium tree	68.8	68.4	86.2	94.4	69.4	84.5	94.7	85.9	92.1	99.0	87.2	93.1	97.4	96.4	94.7
Complex tree	63.8	62.5	85.9	**100**	66.8	84.9	97.7	87.2	94.1	99.3	85.9	93.8	98.4	96.1	96.4
Linear discriminant	68.1	69.4	70.4	73.4	71.1	79.9	74.3	83.2	78.9	76.6	79.6	79.6	80.3	81.6	81.3
Quadratic discriminant	67.8	69.7	79.9	85.2	70.4	84.9	85.2	87.8	90.5	85.2	85.2	88.2	85.9	87.5	85.9
Linear SVM	67.4	70.1	76.0	80.6	69.7	83.9	79.9	85.2	87.2	86.5	84.9	84.9	88.5	89.8	90.1
Quadratic SVM	69.7	70.1	81.3	89.5	69.7	86.2	89.1	88.8	94.1	94.7	90.1	92.4	96.4	95.4	96.7
Cubic SVM	39.8	53.9	79.9	96.4	72.0	86.8	94.4	90.5	94.1	96.7	86.8	91.4	97.7	96.4	96.4
Coarse Gaussian SVM	64.5	70.1	78.3	79.3	70.1	83.9	78.0	86.2	83.9	83.9	86.2	84.5	86.5	90.1	90.1
Medium Gaussian SVM	68.4	70.4	80.9	90.8	70.4	85.5	87.5	89.8	95.1	99.3	89.8	93.4	97.4	96.7	96.7
Fine Gaussian SVM	67.4	68.8	88.8	**100**	70.1	85.2	89.8	81.6	94.4	**100**	69.7	71.4	84.9	81.3	68.8
Coarse kNN	64.5	64.5	70.4	64.5	64.5	65.5	64.5	67.4	64.5	67.4	64.5	64.5	67.1	67.4	67.4
Medium kNN	67.4	68.8	87.5	98.7	70.1	83.2	81.3	89.1	92.4	98.4	84.9	86.2	87.8	96.4	89.5
Fine kNN	56.9	54.9	84.9	**100**	62.5	88.5	90.5	88.8	94.7	**100**	86.2	91.4	97.4	98.0	96.1
Cosine kNN	64.5	64.5	75.7	69.4	72.0	80.9	74.0	81.3	82.2	89.8	82.6	81.6	82.9	88.5	85.2
Cubic kNN	66.8	69.7	86.8	98.0	72.0	81.3	81.6	89.5	88.5	97.0	84.9	85.5	85.9	94.1	90.1
Weighted kNN	60.2	59.9	87.2	**100**	68.8	84.2	92.8	88.8	95.4	**100**	86.5	92.1	97.0	97.7	94.1

Table 6: Accuracy (%) of the machine learning models using the detector responses from the external detector positions. Results for the NDA technique with the fuel assembly in air. The cases with complete correct classification are highlighted in bold.

Detector positions considered: central, peripheral, external (3 features per detector response)

Detector response 1	TH	RES	FA	P	TH	TH	TH	RES	RES	FA	TH	TH	TH	RES	TH
Detector response 2					RES	FA	P	FA	P	P	RES	RES	FA	FA	RES
Detector response 3											FA	P	P	P	FA
Detector response 4															P
Simple tree	70.7	70.7	92.4	92.8	72.0	92.4	92.8	92.4	93.1	93.1	92.4	93.1	92.1	92.4	91.4
Medium tree	70.4	71.4	98.0	**100**	72.7	97.4	**100**	97.7	**100**	99.7	96.4	**100**	99.3	99.3	99.0
Complex tree	71.7	68.4	98.0	**100**	71.1	97.4	**100**	98.0	**100**	99.7	97.7	**100**	99.0	99.3	99.3
Linear discriminant	71.1	68.8	90.1	88.8	63.5	87.2	86.2	85.5	85.9	88.5	82.6	84.2	90.5	87.5	88.2
Quadratic discriminant	71.7	66.8	92.4	94.4	66.1	93.1	95.1	93.1	95.1	94.4	91.8	95.1	94.4	95.4	95.4
Linear SVM	89.8	78.6	94.1	94.1	87.5	94.1	93.8	94.1	93.1	96.1	94.7	96.4	94.1	95.4	94.4
Quadratic SVM	92.8	80.6	97.7	98.7	93.1	99.7	99.7	98.7	97.7	98.4	99.0	99.0	98.4	99.3	99.7
Cubic SVM	91.8	82.6	99.3	**100**	92.1	**100**	**100**	98.7	99.7	**100**	98.7	98.4	**100**	99.7	98.7
Coarse Gaussian SVM	74.7	73.4	92.8	94.4	77.6	94.7	94.1	93.1	94.7	96.1	95.1	95.7	97.0	97.7	97.4
Medium Gaussian SVM	83.6	75.0	99.7	**100**	80.9	98.7	99.0	95.4	97.7	**100**	87.8	86.8	98.0	95.7	86.2
Fine Gaussian SVM	79.3	70.1	98.0	**100**	64.5	68.1	77.3	64.5	70.4	98.7	64.5	64.5	67.4	64.5	64.5
Coarse kNN	64.5	64.5	73.4	67.4	64.5	72.0	67.4	70.7	66.8	73.0	69.7	66.8	71.7	71.7	70.1
Medium kNN	76.0	73.4	98.7	**100**	75.3	86.2	87.5	90.1	91.1	99.7	85.2	87.8	90.8	93.4	91.4
Fine kNN	83.6	81.3	99.7	**100**	80.3	98.7	99.7	97.4	97.7	**100**	94.7	95.4	**100**	99.0	97.4
Cosine kNN	81.3	73.0	96.1	99.3	78.6	85.2	86.8	87.2	85.2	97.7	85.5	83.2	85.5	88.2	86.2
Cubic kNN	79.6	73.4	99.3	**100**	75.3	85.5	87.5	88.5	89.8	98.7	84.5	85.9	89.5	92.4	87.5
Weighted kNN	82.2	80.3	99.7	**100**	79.6	98.4	97.7	95.7	96.1	**100**	92.1	91.1	99.0	99.0	96.4

Table 7: Accuracy (%) of the machine learning models using the detector responses from all detector positions. Results for the NDA technique with the fuel assembly in air. The cases with complete correct classification are highlighted in bold.

Detector positions considered: external (1 feature per detector response)															
Detector response 1	TH	RES	FA	P	TH	TH	TH	RES	RES	FA	TH	TH	TH	RES	TH
Detector response 2					RES	FA	P	FA	P	P	RES	RES	FA	FA	RES
Detector response 3											FA	P	P	P	FA
Detector response 4															P
Simple tree	76.0	74.7	82.2	87.2	78.0	82.9	86.2	83.6	87.2	88.5	84.2	85.9	88.2	89.1	88.8
Medium tree	77.6	75.7	85.2	96.1	79.9	88.8	95.7	84.9	97.7	97.4	88.2	95.1	96.4	95.4	94.7
Complex tree	77.6	74.0	86.2	98.7	78.6	88.5	96.4	84.9	96.4	97.0	88.5	95.1	96.1	93.1	96.7
Linear discriminant	71.4	71.1	69.4	74.0	71.7	72.0	79.6	73.4	77.3	79.3	73.0	80.3	80.9	78.6	80.9
Quadratic discriminant	78.3	76.6	78.3	85.5	77.0	81.3	87.8	80.6	85.2	86.8	83.9	88.8	89.8	87.2	91.4
Linear SVM	75.0	73.7	76.6	82.6	74.7	78.0	87.5	76.6	83.9	85.5	77.6	87.5	90.1	84.2	91.4
Quadratic SVM	77.0	75.7	78.6	88.2	77.3	88.8	92.4	85.9	90.1	98.0	86.8	92.8	95.7	95.4	95.7
Cubic SVM	72.0	69.4	78.3	91.8	76.0	89.1	95.1	85.2	93.1	99.0	88.8	94.7	98.4	97.7	97.7
Coarse Gaussian SVM	77.3	74.3	76.6	80.3	77.3	79.3	88.5	77.3	84.2	82.9	79.6	88.8	89.8	88.5	91.8
Medium Gaussian SVM	77.6	76.0	81.6	85.9	78.3	87.2	93.8	83.6	90.1	96.7	87.5	92.4	99.0	97.7	99.3
Fine Gaussian SVM	78.9	77.6	87.2	97.0	76.3	87.5	95.7	82.9	92.8	**100**	78.9	79.6	96.7	93.1	76.6
Coarse kNN	71.4	68.8	70.4	64.5	69.7	70.4	67.4	70.4	67.4	68.4	70.4	67.4	68.1	67.8	68.8
Medium kNN	77.3	73.4	83.6	98.4	78.6	87.2	93.1	82.6	89.1	99.7	85.5	88.5	97.7	91.1	93.1
Fine kNN	74.7	75.0	84.5	97.0	79.3	89.5	97.7	84.2	95.4	**100**	88.8	93.1	**100**	**100**	99.3
Cosine kNN	75.0	64.5	73.7	72.0	72.0	76.6	88.5	76.3	82.6	86.5	78.6	83.6	90.5	87.2	89.8
Cubic kNN	79.9	73.7	83.6	98.7	78.6	89.1	89.5	81.3	87.5	96.7	83.6	89.1	96.4	92.4	93.1
Weighted kNN	74.0	75.3	83.2	97.4	78.6	90.8	97.0	82.9	94.1	**100**	87.8	93.1	99.3	97.7	97.7

Table 8: Accuracy (%) of the machine learning models using the detector responses from the external detector positions. Results for the NDA technique with the fuel assembly in fresh water. The cases with complete correct classification are highlighted in bold.

Detector positions considered: central, peripheral, external (3 features per detector response)																
Detector response 1	TH	RES	FA	P	TH	TH	TH	RES	RES	FA	TH	TH	TH	RES	TH
Detector response 2					RES	FA	P	FA	P	P	RES	RES	FA	FA	RES
Detector response 3											FA	P	P	P	FA
Detector response 4															P
Simple tree	78.6	82.2	93.4	94.1	84.5	93.4	94.1	87.8	88.5	94.1	88.8	88.8	93.8	88.8	89.8
Medium tree	81.6	81.9	98.4	**100**	83.9	98.7	**100**	96.7	97.0	99.7	96.7	96.7	99.7	96.4	95.7
Complex tree	81.6	83.2	99.0	**100**	85.5	99.0	**100**	95.7	97.0	99.7	97.0	95.7	99.3	97.0	96.1
Linear discriminant	75.7	75.0	90.5	86.8	73.0	86.5	86.8	85.5	87.2	91.1	81.3	81.6	89.1	88.5	86.2
Quadratic discriminant	83.6	80.3	93.4	94.7	80.6	93.8	95.4	95.4	96.1	94.7	92.8	95.1	95.7	96.1	95.7
Linear SVM	80.6	81.9	94.1	93.4	82.9	92.8	93.8	95.4	96.7	95.7	95.4	94.4	93.4	95.4	94.4
Quadratic SVM	84.9	84.9	99.0	98.4	87.5	99.7	99.3	99.0	99.7	98.4	99.0	99.7	99.0	99.7	99.7
Cubic SVM	84.2	85.9	**100**	**100**	84.9	**100**	99.3	99.3	**100**	**100**	99.3	99.3	**100**	99.7	**100**
Coarse Gaussian SVM	81.3	83.6	93.4	94.1	83.6	93.8	95.1	95.7	98.4	96.4	94.7	97.4	97.4	99.0	98.0
Medium Gaussian SVM	84.9	82.6	**100**	**100**	84.2	98.7	98.4	97.4	96.7	**100**	89.5	93.1	99.0	97.0	89.1
Fine Gaussian SVM	76.3	69.1	99.7	**100**	65.1	68.1	69.7	65.5	65.8	98.7	64.5	65.1	64.5	65.1	64.5
Coarse KNN	65.1	68.8	73.4	67.4	66.4	72.0	68.1	73.4	71.4	73.4	73.0	69.1	73.0	73.4	73.4
Medium KNN	78.9	81.3	99.3	**100**	82.2	88.2	90.5	94.1	95.7	**100**	90.8	92.8	94.4	99.0	95.4
Fine KNN	81.9	80.9	**100**	**100**	82.9	**100**	**100**	98.0	99.7	**100**	95.1	97.7	**100**	**100**	99.7
Cosine KNN	76.0	77.3	93.8	98.7	81.3	85.5	86.8	90.5	92.1	98.7	88.2	89.8	90.1	95.1	91.1
Cubic KNN	77.3	80.3	97.7	**100**	82.2	85.5	89.5	91.1	94.7	**100**	88.5	90.5	92.4	94.7	93.1
Weighted KNN	82.9	80.6	**100**	**100**	82.9	98.4	98.0	98.0	98.7	**100**	95.1	96.4	99.7	**100**	99.0

Table 9: Accuracy (%) of the machine learning models using the detector responses from all detector positions. Results for the NDA technique with the fuel assembly in fresh water. The cases with complete correct classification are highlighted in bold.

6. Conclusion

The detector responses of a set of detector types were modelled to assess the capability of machine learning models to detect the diversion of fuel pins from a fuel assembly. Several machine learning models were developed and applied for the data analysis for an NDA technique with fuel assembly either in air or in fresh water.

The different models were evaluated in terms of accuracy, which was defined as the percentage of cases with correct classifications compared to the total dataset. The use of the NDA technique for a fuel assembly either in air or in fresh water was also compared using this metric.

The results for the NDA technique showed that the detector response used for the data analysis plays an important role in the accuracy of the model, and in general the gamma-ray detector response obtained the highest accuracy compared to the neutron detector responses. However, the addition of multiple detector responses did not improve significantly the accuracy of the models.

Comparing the use of the NDA technique for a fuel assembly either in air or in fresh water, similar results in terms of accuracy were obtained for the majority of the models. Only in some cases the accuracy calculated with the fuel assembly in fresh water was more than 5% higher compared to the value obtained with the fuel assembly in air.

Very promising results were obtained for the machine learning models using the decision trees, support vector machine, and nearest neighbors techniques. Several models reached a complete correct classification over the dataset used in this study, especially when the gamma-ray detector response was used alone or in combination with other features.

Future work will refine the models developed in this study by investigating different model parameters with the aim of increasing the accuracy of the current models. The uncertainty of the calculated accuracy will also be estimated. In addition, the training database will be further expanded by generating several additional diversion scenarios and including other detector responses to be used as input features.

7. References

[1] International Atomic Energy Agency (IAEA). "*The structure and content of agreements between the Agency and States required in connection with the treaty on the nonproliferation of nuclear weapons*". INFCIRC/153 (corrected), 1972.

[2] International Atomic Energy Agency (IAEA). "*IAEA annual report for 2013*". IAEAGC(58)/3, 2014.

[3] van der Meer K., et al. "*An assessment of the FORK detector as a partial defect tester*". Proceedings of the 27th ESARDA Symposium on Safeguards and Nuclear Material Management, London, 10-12 May, 2005.

[4] Grape S., et al. "*Recent modelling studies for analysing the partial-defect detection capability of the Digital Cherenkov Viewing Device*". Proceedings of the 2013 ESARDA annual meeting, 2013.

[5] White T., et al. "*Application of Passive Gamma Emission Tomography (PGET) to the inspection of spent nuclear fuel*". Proceedings of the 2018 INMM annual meeting, 2018.

[6] Rossa R. "*Advanced non-destructive methods for criticality safety and safeguards of used nuclear fuel*". Ph.D. dissertation at Université libre de Bruxelles, 2016.

[7] Smola A., et al. "*Introduction to Machine Learning*". Cambridge University Press. ISBN 0 521 82583 0, 2008.

[8] Rossa R. "*Comparison of the SINRD and PDET detectors for the detection of fuel pins diversion in PWR fuel assemblies*". Proceedings of the 59th INMM Annual Meeting, 2018.

[9] Kotsiantis S. B. "Supervised Machine Learning: A Review of Classification Techniques". Informatica 31, 2007, Pages 249-268.

[10] Soofi A. A., et al. "*Classification techniques in machine learning: applications and issues*". Journal of basic & applied sciences, 2017, 13, Pages 459-465.

[11] Borella A., et al. "*Signatures from the spent fuel: simulations and interpretation of the data with neural network analysis*". ESARDA Bulletin, No. 55, December 2017, Pages 29-38.

[12] Menlove H. O., et al. "*A resonance self-indication technique for isotopic assay of fissile material*". Nuclear applications, volume 6, 1969, Pages 401-408.

[13] LaFleur A. M. "*Development of self-interrogation neutron resonance densitometry (SINRD) to measure the fissile content in nuclear fuel*". Ph.D. dissertation at Texas A&M University, 2011.

[14] LaFleur A. M., et al. "*Development of self interrogation neutron resonance densitometry to improve detection of partial defects in PWR spent fuel assemblies*". Nuclear Technology, 181, 2013, Pages 354-370.

[15] LaFleur A. M., et al. "*Analysis of experimental measurements of PWR fresh and spent fuel assemblies*

using self-interrogation neutron resonance densitometry". Nuclear Instruments and Methods Section A, 781, 2015, Pages 86-95.

[16] Rossa R., et al. "*Investigation of the self-interrogation neutron resonance densitometry applied to spent fuel using Monte Carlo simulations*". Annals of Nuclear Energy 75, 2015, Pages 176-183.

[17] Sitaraman S., et al. "*Characterization of a safeguards verification methodology to detect pin diversion from pressurized water reactor (PWR) spent fuel assemblies using Monte Carlo techniques*". Proceedings of the 48th INMM annual meeting, 2007.

[18] Ham Y. S., et al. "*Development of a safeguards verification method and instrument to detect pin diversion from pressurized water reactor (PWR) spent fuel assemblies phase I study*". Lawrence Livermore National Laboratory technical report LLNL-TR-409660, 2009.

[19] Ham Y. S., et al. "*A new versatile safeguards tool for verification of PWR spent fuel*". Proceedings of the 53rd INMM annual meeting, 2012.

[20] Ham Y. S., et al. "*Partial defect verification of spent fuel assemblies by PDET: principle and field testing in interim spent fuel storage facility (CLAB) in Sweden*". Proceedings of the 2015 ANIMMA conference, 2015.

[21] Rossa R., et al. "*Development of a reference spent fuel library of 17x17 PWR fuel assemblies*". ESARDA Bulletin n. 50, 2013, Pages 48-60.

[22] Mitchell T. M. "*Machine Learning*". McGraw-Hill editor, 1997.

[23] Bishop C. M. "*Pattern recognition and machine learning*". Springer, 2006, ISBN-13: 978-0387-31073-2.

[24] Oudeyer P-Y. "*The production and recognition of emotions in speech: features and algorithms*". International Journal of Human-Computer Studies, Volume 59, Issues 1–2, 2003, Pages 157-183.

[25] Ngai E. W. T., et al. "*The application of data mining techniques in financial fraud detection: A classification framework and an academic review of literature*". Decision Support Systems, Volume 50, Issue 3, 2011, Pages 559-569.

[26] Kourou K., et al. "*Machine learning applications in cancer prognosis and prediction*". Computational and Structural Biotechnology Journal, Volume 13, 2015, Pages 8-17.

[27] Murphy K. P. "*Machine learning: a probabilistic perspective*". Massachusetts Institute of Technology, 2012, ISBN 978-0-262-01802-9.

[28] MathWorks, Inc. "*Statistics and Machine Learning Toolbox™ - User's Guide*", 2018.

[29] Li T., et al. "*Using discriminant analysis for multi-class classification: an experimental investigation*". Knowledge and Information Systems 10 (4), 2006, Pages 453-472.

[30] Kecman V. "*Support Vector Machines – An Introduction*". Studies in Fuzziness and Soft Computing, Springer, 2005.

[31] Iggane M., et al. "*Self-training using a k-Nearest Neighbor as a base classifier reinforced by Support Vector Machines*". International Journal of Computer Applications (0975 – 8887) Volume 56– No. 6, 2012.

Verifying PWR assemblies with rod cluster control assembly inserts using a DCVD

Erik Branger, Sophie Grape, Peter Jansson
Uppsala University, Uppsala, Sweden
E-mail: erik.branger@physics.uu.se

Abstract:

One of the instruments available to authority inspectors to measure and characterize the Cherenkov light emissions from irradiated nuclear fuel assemblies in wet storage is the Digital Cherenkov Viewing Device (DCVD). Based on the presence, characteristics and intensity of the Cherenkov light, the inspectors can verify that an assembly under study is not a dummy object, as well as perform partial defect verification of the assembly.

PWR assemblies are sometimes stored with a rod cluster control assembly (RCCA) inserted, which affects the Cherenkov light production and transport in the assembly. Such an insert will also block light from exiting the top of the fuel assembly, which will affect the light distribution and intensity of the Cherenkov light emissions. Whether or not this constitutes a problem when verifying the assemblies for gross or partial defects with a DCVD has not previously been investigated thoroughly.

In this work, the Cherenkov light intensity of a PWR 17x17 assembly with two different RCCA inserts were simulated and analysed, and compared to the Cherenkov light intensity from an assembly without an insert. For the studied assembly and insert types, the DCVD was found to be able to detect partial defects on the level of 50% in all studied cases with similar performance, though with a higher measurement uncertainty due to the reduced intensity when an RCCA insert is present. Consequently, for the studied assembly and insert types, assemblies with inserts can be verified with the same methodology as used for assemblies without inserts, with similar partial defect detection performance.

The simulation approach used also made it possible to investigate the minimum Cherenkov light intensity reduction resulting from partial defects of other levels than 50%, in the PWR 17x17 fuel assembly with and without RCCA inserts. The results for the simulations without an insert were in agreement with previous results, despite differences in substitution patterns, substitution materials, modeling software and analysis approach.

Keywords: DCVD; partial defect verification; Rod cluster control assembly, Cherenkov light; Geant4

1. Introduction

One of the many safeguards inspection tasks undertaken by authority inspectors is to measure irradiated nuclear fuel assemblies to verify that all nuclear material is present and accounted for. To aid the inspectors, a multitude of instruments has been developed. One of the instruments available is the Digital Cherenkov Viewing Device (DCVD), which measures the Cherenkov light produced in the water surrounding an assembly. The characteristics and quality of the Cherenkov light can be used to perform *gross defect verification*, verifying that the assembly under study is a spent nuclear fuel and not a dummy object. The DCVD is more frequently used for *partial defect verification*, verifying that 50% or more of the rods in an assembly have not been diverted. In such a verification, the Cherenkov light intensity emitted by the assembly is integrated to provide a value corresponding to the total light intensity of the assembly. Based on earlier simulations, it is estimated that a 50% substitution of irradiated fuel rods in an assembly with non-radioactive steel rods will decrease the total Cherenkov light intensity of the assembly by at least 30% [1]. Hence, by comparing the measured intensities to predicted ones, assembly intensities deviating more than 30% can be identified. Recent prediction methods account for the irradiation history of the assembly, i.e. its cycle-wise burnup and cooling time, as well as the physical design of the assembly [2]. Any assembly having an intensity deviating more than 30% from expected is flagged as an outlier, and further investigations and measurements are called for to confirm whether the assembly is subject to a partial defect, or if the deviation is caused by something else such as erroneous declarations.

PWR assemblies in wet storage are in some cases stored with inserts, such as a rod cluster control assembly (RCCA) insert. For such storage cases, the neutron absorber rods of the RCCA are stored inserted into the guide tubes of PWR fuels. This can help save storage space, since no additional space is needed to store the RCCA. In addition, when inserted into a fuel assembly, the RCCA helps ensure sufficient limits to criticality. Before placing spent nuclear fuel in a difficult-to-access storage, the assemblies must be verified for partial defects [3]. It is reasonable to assume that the fuel assemblies will be verified

in their current state, with any RCCA inserts still present during the verification measurements.

The presence of an RCCA is believed to affect the Cherenkov light in such fuel assemblies in two ways. Firstly, it prevents Cherenkov light from being created in the guide tubes, as the water inside the guide tubes is substituted by absorber material. Secondly, the RCCA will partly cover the top of the assembly, preventing a significant fraction of Cherenkov light from exiting the assembly to be detected.

Against this background, the objectives with this work is to i) verify the 30% intensity reduction limits of [1] for a 50% partial defect using different simulations codes and partial defect scenarios, since the limit in [1] is an estimate based on 30% rod substitutions. And ii) investigate how RCCA inserts affect the 30% intensity reduction limit assumed for a 50% partial defect level. As a consequence of the methodology chosen to investigate this, it becomes possible to also to study the minimum Cherenkov light reduction resulting from other partial defect levels, ranging from 0-100% substitution of the irradiated rods in an assembly.

2. Simulating the effect of top plates and inserts

To simulate DCVD images of PWR 17x17 assemblies, the three-step method of [4] has been used. These three steps are:

1. In the first step, the gamma emission spectrum of the assembly is simulated using ORIGEN-ARP [5]. In principle, beta decays may contribute, but their contribution has been shown in [2] to be minor and they were therefore neglected here.
2. In the second step, the gamma transport and interaction in a fuel assembly geometry is simulated using Geant4 [6], using a simulation toolkit based on [7]. In this process, Cherenkov light is created and transported to the top of the assembly. Once a Cherenkov photon reaches the top of the assembly, its position and direction is saved. The simulation model considers the full 3-D geometry and axial burnup distribution of the assembly.
3. In the third step, the saved photons are projected onto an imaging plane, using a pinhole camera model, to simulate a DCVD image.

Note that in the second step, the top plate, lifting handle and other structures at the assembly top are not included. The effect of these structures are instead included in the third step. This allows for the computationally expensive second step to be run only once, and different top plates and other structures at the assembly top can quickly be simulated in the third step. The effects of the top structures are studied by applying a mask, detailing where structure material is preventing the Cherenkov light from exiting the fuel assembly, and where light can pass through to be detected.

It was found in [4] that the burnup and cooling time of an assembly will not strongly influence the light distribution in a simulated image. For burnups of 10-40 MWd/kgU and cooling times of 1-40 years the total intensity of the simulated image will change at most 1% due to the changing light distribution. Consequently, in this work one PWR 17x17 assembly with a burnup of 40 MWd/kgU and a cooling time of 10 years was chosen, which is expected to be representative for assemblies with other burnups and cooling times. Using ORIGEN-ARP, the gamma spectrum of the assembly was simulated in the first step, and in the second step the gamma emissions from the fission products were simulated in a fuel geometry. Two different geometries were simulated: one where all guide tubes were filled with water, corresponding to the absence of an insert, and one where all guide tubes were filled with In-Ag-Cd, corresponding to control rod material. Depending on the design of the RCCA, some or all guide tubes will contain absorber material. By applying the top plate mask to the simulations without control rods and with control rods, the extreme values are found for the Cherenkov light intensity in the simulated images. The case of some guide tubes containing control rods are expected to fall between these extreme values.

In the simulations of the second step, the light contribution from each rod in the assembly was stored separately. Thus, it was easy to include only the light contributions from selected rods in the final image. This facilitates studies of partial defect verification, where irradiated fuel rods are substituted by non-irradiated rods with similar density containing natural uranium, depleted uranium or low enriched uranium. Using this approach, it is thus possible to investigate the resulting total Cherenkov light intensity as a function of various rod substitution patterns, and to assess the DCVD capability to detect such substitutions.

2.1 Masks used

To obtain a mask representing the regions of the assembly covered by the top plate, a photograph of a PWR assembly top plate was used. Using the photograph, the covered regions could be manually identified and traced, and converted into a binary mask. The photograph and the resulting mask obtained is shown in Figure 1.

Two different RCCA inserts were studied in this work. For the two RCCA inserts, DCVD images of assemblies with inserts were used to identify which additional regions were covered. This information was used to manually design a mask for assemblies with such inserts. One of the studied inserts had a comparatively large frame for holding the control rods, and consequently covered a substantial fraction of the assembly top, as seen to the left in Figure 2. This

RCCA will be referred to as the “thick insert” in this work. The other studied insert had much finer features, and was relatively more open, as can be seen to the right in Figure 2. This insert will be referred to as the “thin insert” in this work. The thin insert is likely the insert described in [8].

3. Sensitivity of DCVD verification of partial defect in assemblies with inserts

The effect on the total Cherenkov light intensity of substituting irradiated rods with non-radioactive rods is shown in Figure 3. These values show the minimum Cherenkov light intensity reduction for partial defects of a given magnitude. In order to find the most challenging partial defect case to detect, the rods were substituted in an order reflecting their contribution to the total light intensity, starting with replacement of the least significant rod. The rod substitution pattern was estimated individually for the studied cases based on the identification of the fuel rods contributing the least to the total intensity, and the patterns thus differ between the cases. Hence, Figure 3 shows the minimum intensity reduction in the total Cherenkov light intensity for various levels of partial defects, with replacement rods having similar gamma attenuation as the original rod and otherwise identical properties. Thus, for all other substitution scenarios, the intensity reduction will be larger and should be easier to detect.

As mentioned, there are different RCCA designs. In some cases, fuel assemblies with RCCA inserts may have control

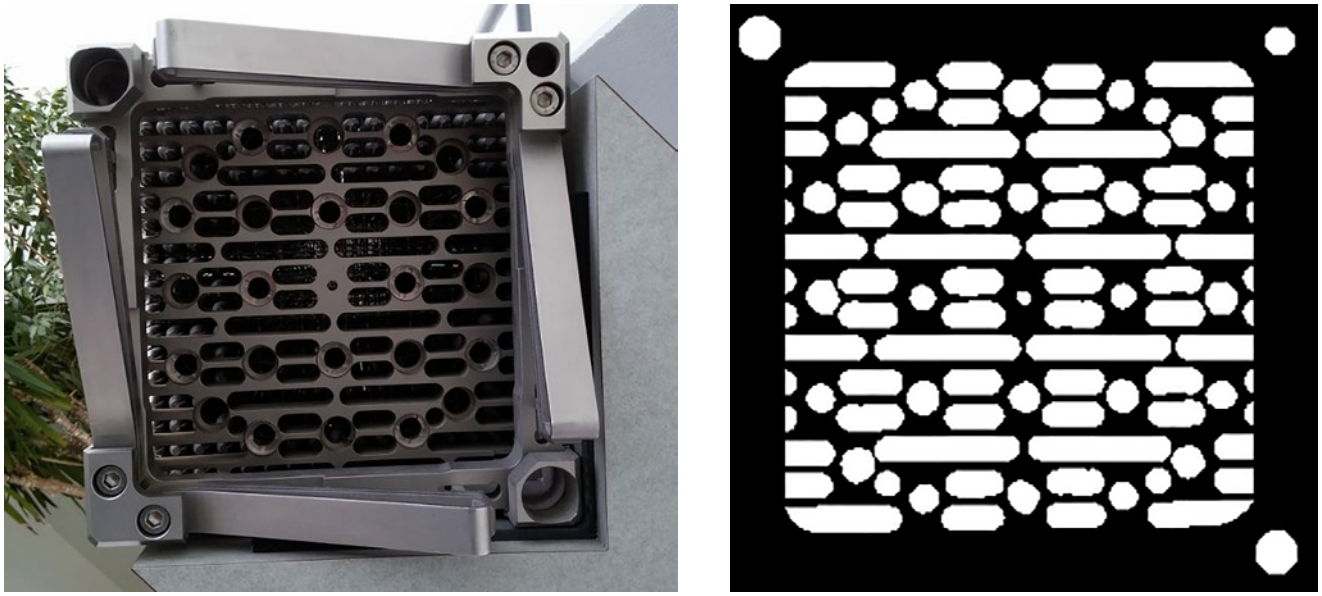

Figure 1 Left: a photograph of the top structure of an assembly model. **Right:** the mask created based on the photograph, to indicate which regions are covered by the top plate and lifting handle.

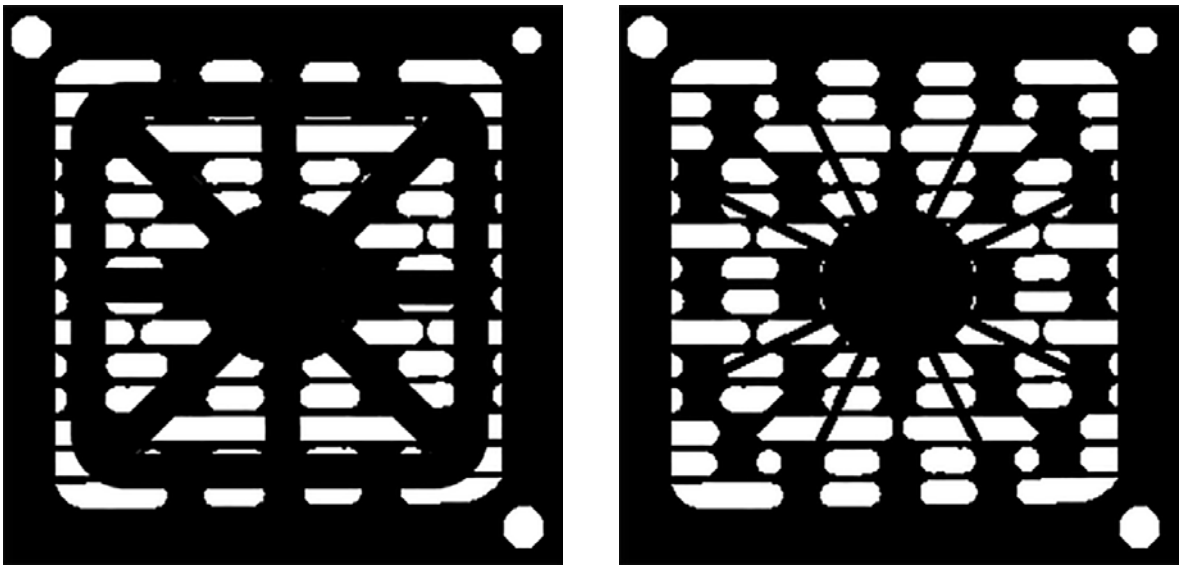

Figure 2 Left: The top plate mask with the addition of the thick RCCA insert, covering a substantial part of the assembly top. **Right:** the top plate mask with the addition of a second, thin type of RCCA insert, having smaller features and covering relatively less compared to the mask on the left. A picture of this insert can be found in [8].

rods inserted into all guide tubes, while in other cases only some of the guide tubes have control rods while others are water-filled. To investigate the impact of this variability on the light intensity, the masks from Figure 2 were applied to the simulated fuel assembly with all control rods present, and to the fuel assembly with only water-filled rods in the guide tube positions. The results for an assembly with an RCCA insert having control rods at only some of the available positions are expected to fall between the results of these two cases. The results show that as the control rods are removed, the light reduction due to a partial defect increases slightly. For both types of RCCA inserts, the light reduction could be up to 1 percent unit higher if the control rods are missing, as compared to if all control rods are present, shown in figure Figure 3. Hence, the case of an RCCA with a full complement of control rods is the most challenging one, and can conservatively be used to estimate the minimum light intensity reduction that a partial defect in an assembly with a RCCA causes.

	No insert	Thick insert	Thin insert
Intensity reduction	27%	27%	29%

Table 1: Cherenkov light intensity reduction at a 50% partial defect level for the studied partial defect cases.

In [1], partial defect detection using the DCVD was studied using simulations. Partial defect levels of 30% (where fuel rods were substituted with stainless steel rods) were studied, with resulting reductions in total Cherenkov light ranging from 15% to 40% depending on the diversion pattern. In [1], it was also estimated that a 50% partial defect would result in at least a 30% intensity reduction. For the case studied here, where partial defects on the level of 30% (where fuel rods are substituted with natural uranium, depleted uranium or low-enriched uranium) are modelled, it is found that the Cherenkov light intensity will be reduced by at least 10%. Partial defects on the level of 50% gives a Cherenkov light intensity reduction of at least 27%, as seen in Table 1 . Both studies hence give rather similar results, despite using different substitution patterns, substitution materials, modeling software and analysis approach.

For the cases of RCCA inserts, the DCVD verification methodology is found to actually be slightly more sensitive to a 50% partial defect, compared to the case of no insert, since the total Cherenkov light reduction is slightly higher. For the thick insert (Figure 2 left), the intensity reduction is at least 27%, and for the thin insert (Figure 2 right) the intensity reduction is at least 29%. Hence, for partial defects at the 50% level, the same partial defect detection criteria in terms of required light intensity reduction can be used for both the insert case as in the non-insert case.

The reason for the higher sensitivity in the RCCA case has to do with the light distribution in a DCVD image. Since the light emitted by the assembly is highly collimated, the central region vertically below the DCVD will be the brightest, and regions further away will appear dimmer. Consequently, in an image without an insert, a rod in the central region will contribute more, in relative terms, to the total Cherenkov light intensity, as compared to a rod near the edge. In

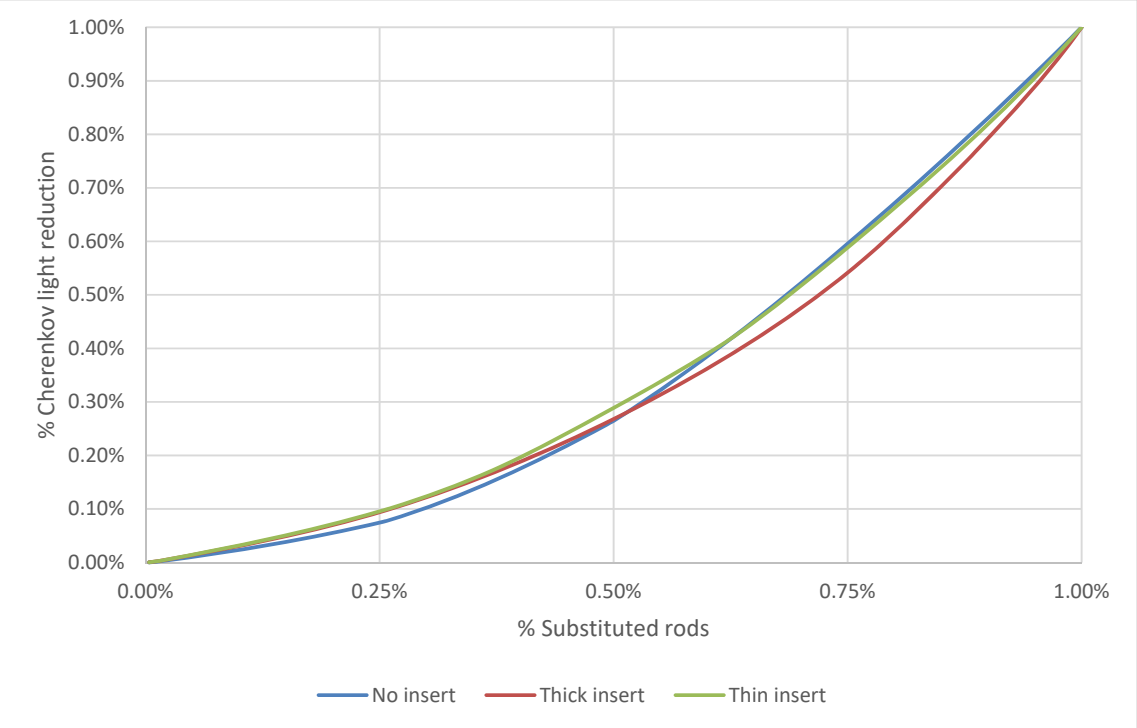

Figure 3: Reduction in Cherenkov light intensity as a function of the fraction of rods replaced with non-radioactive substitutes. Rods contributing the least to the total intensity were removed first, and accordingly the rod substitution pattern differs in all three cases.

addition, since the lifting handle covers the edges, the intensity contribution from a rod at the edge is further suppressed. When an RCCA is present, it will cover large parts of the central region, and consequently suppress the intensity from the otherwise brightest regions at the center. As a result, the distribution of light over the measurement image will be more even, and the relative intensity contributions from the rods will vary less when an RCCA is present.

For the studied cases with and without an RCCA insert, the DCVD verification methodology is least sensitive to substitution of rods near the assembly edge. As noted above, this is a combined effect of the collimation and of the lifting handle obstructing the view. For the more centrally located rods, the contribution per rod to the total intensity varies significantly, depending on which parts that are covered by the RCCA insert. Thus, for partial defect on the order of 50%, the rod substitution pattern that is most challenging to detect using the DCVD, will differ depending on the presence or absence of an RCCA insert, and will be different for RCCA of different designs.

While the inserts do not significantly change the intensity reduction limits, they do change the total Cherenkov light intensity of the image. The simulated total intensity reduction for the two RCCA cases is compared to the non-insert case in Table 2. As can be seen, the insert will significantly reduce the intensity of the Cherenkov light reaching the DCVD detector, and consequently the measurement uncertainties in the RCCA insert case will be higher, for otherwise identical assemblies. Thus, care must be taken when verifying low-intensity assemblies with inserts. Without inserts such assemblies may have a sufficiently high Cherenkov light intensity to be verified for a 50% partial defect level, but with an RCCA present, the intensity may be too low to allow for an accurate measurement, and thus an accurate verification. For the case of a RCCA insert with only a few control rods, the relative intensity is slightly higher, and can increase up to 40% for the thick insert and up to 50% for the thin insert (an increase with 3 percentage points in both cases). These values are similar enough that the assemblies can be readily compared, even if their RCCA inserts contain a different number of control rods, as long as the physical design of the top of the RCCA is the same. The main cause of the change in Cherenkov light intensity in the RCCA case is that more parts of the top of the assembly are covered, the effect of having RCCA inserts with differing number of control rods is less significant.

	No insert	Thick insert	Thin insert
Relative intensity	100%	37%	47%

Table 2: Relative measured Cherenkov light intensity for an assembly without an RCCA insert and for the same assembly with a thick respectively a thin insert present. The values are scaled so that the intensity of the no-insert case is 100%.

4. Conclusions and outlook

PWR assemblies in wet storage can be stored with an RCCA inserted, which will alter the characteristics and detected total intensity of the Cherenkov light produced inside the assembly. This work has investigated the partial defect detection capability of the DCVD for one PWR 17x17 fuel assembly. A regular fuel assembly has been modelled, as well as the same fuel assembly with two different kinds of RCCA inserts. The minimum expected reduction in total Cherenkov light has then been modelled for partial defects ranging from 0% to 100% for the fuel assembly without as well as with RCCA inserts. The substitution scenario considered is that the irradiated rods are replaced by non-irradiated rods, having identical gamma attenuation properties. Such replacement rods could for example be made of low-enriched uranium, natural uranium or depleted uranium.

The simulation results indicate that the studied partial defect scenarios affects assemblies with and without RCCA inserts in a similar way. Consequently, the currently adopted partial defect verification method using the DCVD can be used also to verify partial defects also in the case of assemblies with inserts, with similar partial defect detection performance. Furthermore, the previously established detection requirement of a 30% reduction in the measured Cherenkov light intensity (for a partial defect level of 50%) compared to the predicted one, can be applied also to the RCCA insert cases. Some RCCA inserts do not have control rods in all available positions, but the simulation results show that this has a comparatively small effect on the total Cherenkov light intensity, and does not pose any additional problems to the verification methodology.

For the studied PWR 17x17 assembly, the rods closest to the edges contribute the least to the detected Cherenkov light intensity. This is due to the collimation of the Cherenkov light, coupled with the positioning of the DCVD during a measurement, and due to the lifting handle covering rod positions around the edges of the fuel assembly. It may be possible to compensate for the collimation by performing measurements with the DCVD aligned over the edges of the assembly. Alternatively, it may be possible to model the effect of the collimation on the light distribution in an image, and use that information to compensate for the collimation effect. Both these procedures could potentially increase the DCVD verification methodology sensitivity to rod substitution near the assembly edges. However, care must be taken to consider Cherenkov light produced in an assembly due to radiation originating in neighbouring assemblies, since such radiation will not travel far to reach a neighbouring assembly, and will hence predominately create Cherenkov light near the edges of an assembly.

In addition to RCCA inserts, assemblies may be stored with other inserts, such as a flow stoppers. The

methodology developed here could be applied to assess how such an insert affects the partial defect sensitivity of the DCVD verification methodology. Ideally, all types of inserts that frequently occur should be investigated in this way, to ensure that the standard DCVD verification procedure will accurately verify such assemblies.

5. Acknowledgements

This work was supported by the Swedish Radiation Safety Authority (SSM), under contract SSM2012-2750, and SSM2017-5979. The computations were performed on resources provided by SNIC through Uppsala Multidisciplinary Centre for Advanced Computational Science (UPPMAX) under project p2007011.

6. References

[1] J.D. Chen et al., “Partial defect detection in LWR spent fuel using a Digital Cerenkov Viewing,” *Institute of Nuclear Materials Management 50th annual meeting,* 2009.

[2] E. Branger, s. Grape, S. Jacobsson Svärd and P. Jansson, “Comparison of prediction models for Cherenkov light emissions from nuclear fuel assemblies,” *Journal of instrumentation,* 2017.

[3] International Atomic Energy Agency, “Special Criteria for Difficult-to-Access Fuel Items. SG-GC-Annex-04,” Vienna, Austria, 2009.

[4] E. Branger, S. Grape, P. Jansson and S. Jacobsson Svärd, “On the inclusion of light transport in prediction tools for Cherenkov light intensity assessment of irradiated nuclear fuel assemblies,” *Journal of Instrumentation,* vol. 14, 2019.

[5] S. Bowman, L. Leal, O. Hermann and C. Parks, “ORIGEN-ARP, a fast and easy to use source term generation tool,” *Journal of Nuclear Science and Technology,* vol. 37, pp. 575-579, 2000.

[6] Agostinelli, S, et al (the Geant4 collaboration), “Geant4 - a simulation toolkit,” Nuclear Inst. and Meth. in Physics Research Section A: Accelerators, Spectrometers, Detectors and Associated Equipment, Volume 506, Issue 3, 1 July 2003, Pages 250-303.

[7] S. Grape, S. Jacobsson Svärd and B. Lindberg, “Verifying nuclear fuel assemblies in wet storage on a partial defect level: A software simulaiton tool for evaluating the capabilities of the Digital Cherenkov Viewing Device,” Nuclear inst. and Meth. A, Volume 698, 11 January 2013, Pages 66-71, ISSN 0168-9002, 10.1016/j.nima.2012.09.048.

[8] Westinghouse Nuclear, “Enhanced Performance – Rod Cluster Control Assemblies (EP-RCCAs). Data sheet.,” 10 2014. [Online]. Available: http://www.westinghousenuclear.com/Portals/0/flysheets/NF-FE-0047%20Enhanced%20Performance%20RCCAs.pdf. [Accessed 04 04 2019].

Determination of ^{239}Pu content in spent fuel with the SINRD technique by using artificial and natural neural networks

Borella Alessandro[1], Riccardo Rossa[1], Hugo Zaioun[1,2]

[1]SCK•CEN, Boeretang 200, B2400 Mol, Belgium
[2]IMT Atlantique, Campus de Nantes, rue Alfred Kastler 4, 44307 Nantes, France
Email: aborella@sckcen.be

Abstract:

In the last years, a database of simulated spent fuel observables was developed at SCK•CEN by combining the results of depletion-evolution codes and the responses of several detectors obtained by Monte Carlo models. We analysed the large amount of generated data with Artificial Neural Networks, by using the MATLAB toolbox.

In this paper we focus on the application of Artificial Neural Networks to simulated Self-Interrogation Neutron Resonance Densitometry observables with the aim to quantify the ^{239}Pu content in spent fuel. In view of a realistic application of the method, the number of data in the training and validation sets was limited to 20 spent fuel assemblies; the obtained performance when using randomly selected spent fuel assembly was compared with the one obtained when the spent fuel assemblies were selected by expert judgement. The average deviation between the nominal ^{239}Pu content and the calculated ^{239}Pu content in the testing data set was 0.2% with a standard deviation of 3.5% and a maximum deviation of 10%.

It was found that the selection of spent fuel assemblies based on expert judgement results in better performances and therefore speeds up the data analysis when compared to a pure random selection of the data; hence the term natural, as opposite to artificial, is present in the title of the paper.

Keywords: Spent Fuel; Non Destructive Analysis observables; Artificial neural networks; Self-Interrogation Neutron Resonance Densitometry; Large Data sets

1. Introduction

Non-destructive assay (NDA) of spent fuel assemblies (SFA), either for safeguards verification purposes or for safety aspects related to nuclear fuel cycle, relies often on the detection of neutron and gamma radiation spontaneously emitted by the spent fuel [1]. Gamma radiation is mainly emitted by fission products and therefore its measurement does not represent a direct assay of the quantity of fissile material present in the SFA. Neutron radiation is originating mainly from spontaneous fission decay and α-decay via (α,n) reactions on oxygen isotopes. The decay of actinides such as Cm isotopes represents the main source of such neutron radiation which can then undergo subsequent multiplication in the fissile material of the fuel. Therefore, also the observables associated to neutron measurements on SFA do not represent a direct assay of the quantity of fissile material present in the SFA, unless one is able to determine the multiplication and relate that to the residual fissile mass [2].

In this framework, and in relation to increased verification needs associated to the imminent start of operation of geological repositories [3,4], R&D on NDA intensified in the last decade [5,6,7,8,9]. One of the techniques that was studied is the Self-Interrogation Neutron Resonance Densitometry (SINRD) [10,11]. The observables associated to this technique are directly related to the quantity of ^{239}Pu in the fuel and therefore have the potential to provide means for a direct quantification of the ^{239}Pu amount in a SFA.

The use of the SINRD technique and the data analysis of the associated observables by means of artificial neural network (ANN) [12,13] is described in the paper.

2. Self-Interrogation Neutron Resonance Densitometry observables

The SINRD technique [10] is a NDA technique for the direct quantification of ^{239}Pu. The total neutron cross-section of ^{239}Pu shows a strong resonance around 0.3 eV and the attenuation of the neutron flux around the 0.3 eV energy region is used to directly quantify the ^{239}Pu mass. The passive neutron emission from spent fuel is measured with fission chambers bare or wrapped with different absorbers as follows:

- Cd wrapped ^{235}U fission chamber, insensitive to thermal neutrons
- Bare ^{235}U fission chamber, mainly sensitive to thermal neutrons
- Bare ^{238}U fission chamber, mainly sensitive to fast neutrons
- ^{239}Pu fission chamber covered by Gd foil, sensitive to neutrons with energy > 0.1 eV
- ^{239}Pu fission chamber covered by Cd foil, sensitive to neutrons with energy > 1 eV

The observables of interest are two; the first one is the SINRD signature R_{SI}, defined as the ratio between the neutron count by the ^{238}U fission chamber (C_{FAST}) and the count differences in the Gd and Cd wrapped ^{239}Pu loaded fission chamber (C_{Gd}-C_{Cd}); the second one is the ratio between C_{FAST} and the count differences in the bare and the Cd wrapped a ^{235}U fission chambers (C_{TH}).

As explained in [14] the estimated uncertainty due to counting statistics for a measurement time of 1 h is strongly dependent on the burnup of the spent fuel assembly. This estimated uncertainty is lower than 5% for fuel with 3.5% initial enrichment, 5 years of cooling time, and burnup larger than 15 GWd/t_{HM} [14]. The use of ^{239}Pu fission chambers enhances the sensitivity of the technique to ^{239}Pu content [11].

The two observables were estimated by means of Monte Carlo simulations with the code MCNPX 2.7.0 [15], the radionuclide composition of the fuel was taken from the spent fuel library developed at SCK•CEN [16,17,18]. Two observables, R_{SI} and C_{FAST}/C_{TH}, were determined for a total of 2940 cases of the spent fuel library [19].

The obtained results [7] for 17x17 PWR SFA indicated that SINRD can only be applied in dry conditions and that calibration curves can be determined to quantify ^{239}Pu provided that initial enrichment (IE) is known.

Figure 1 shows the R_{SI} observable as a function of ^{239}Pu content for different values of IE and BU. If the burnup (BU) is above 30 GWd/t_{HM} the data cluster around an almost straight line and there is a strong correlation between R_{SI} and ^{239}Pu content irrespective if the IE. For burnup below 30 GWd/t_{HM} the data exhibit a more scattered behaviour. This is due the fact that at lower BU values the presence of ^{235}U interferes due to the presence of a weak resonance at about the same energy as the one of ^{239}Pu.

The ratio C_{FAST}/C_{TH}, shown in Fig. 2, can be used to determine the IE if the BU is less than 30 GWd/t_{HM} and to account for the interference from ^{235}U. The ratio R_{SI} is almost independent from the cooling time (CT) up to CT of 300 years, while the ratio C_{FAST}/C_{TH} starts to decrease from not less than 10 years (Fig. 3).

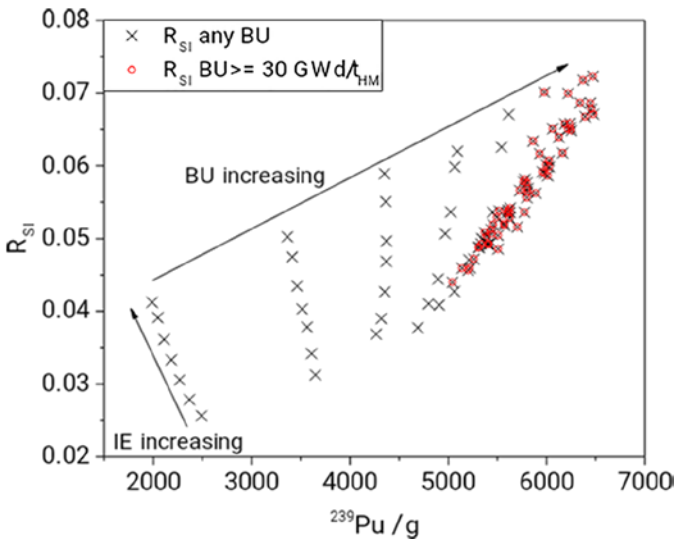

Figure 1: R_{SI} as function of ^{239}Pu amount for any BU values and for BU values of at least 30 GWd/t_{HM}. CT was 5 years and IE between 2% and 5%.

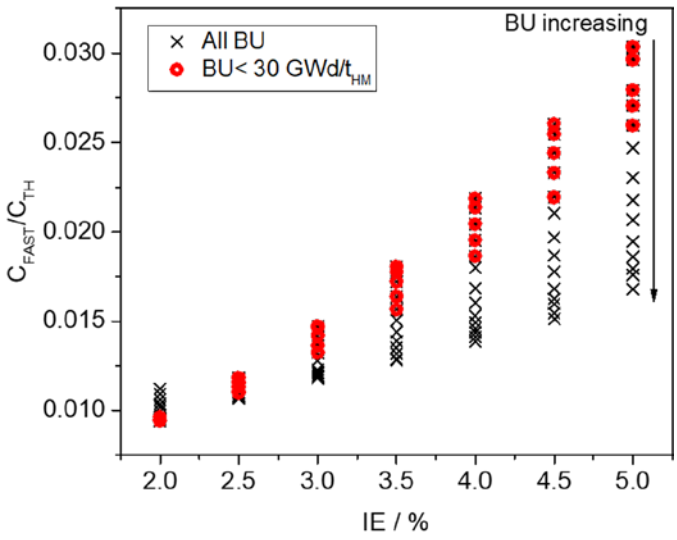

Figure 2: C_{FAST}/C_{TH} as a function of IE for any BU values and a CT of 5 years. The results for BU values of less than 30 GWd/t_{HM} are highlighted in a different colour.

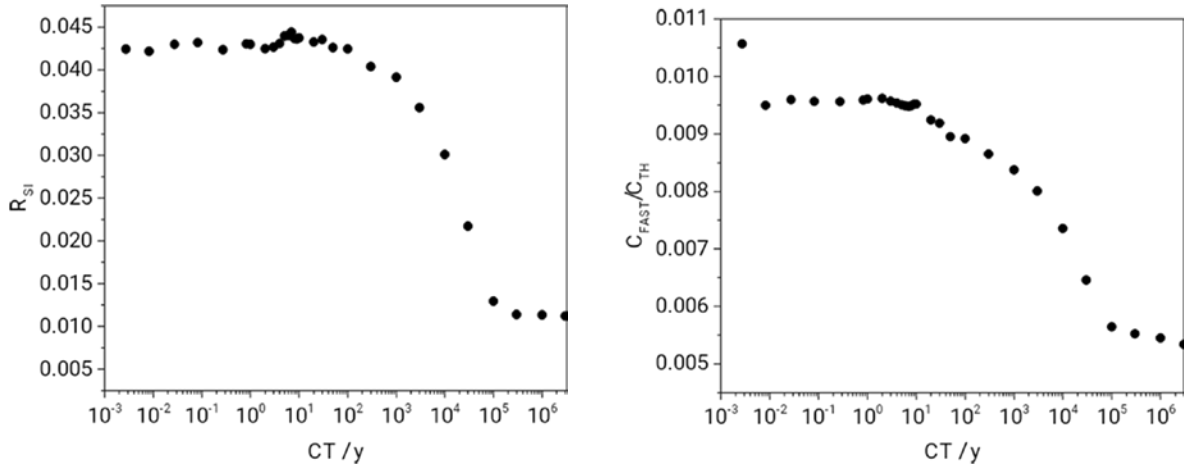

Figure 3: R_{SI} and C_{FAST}/C_{TH} as a function of CT. The data are for an IE of 2% and BU of 30 GWd/t_{HM}.

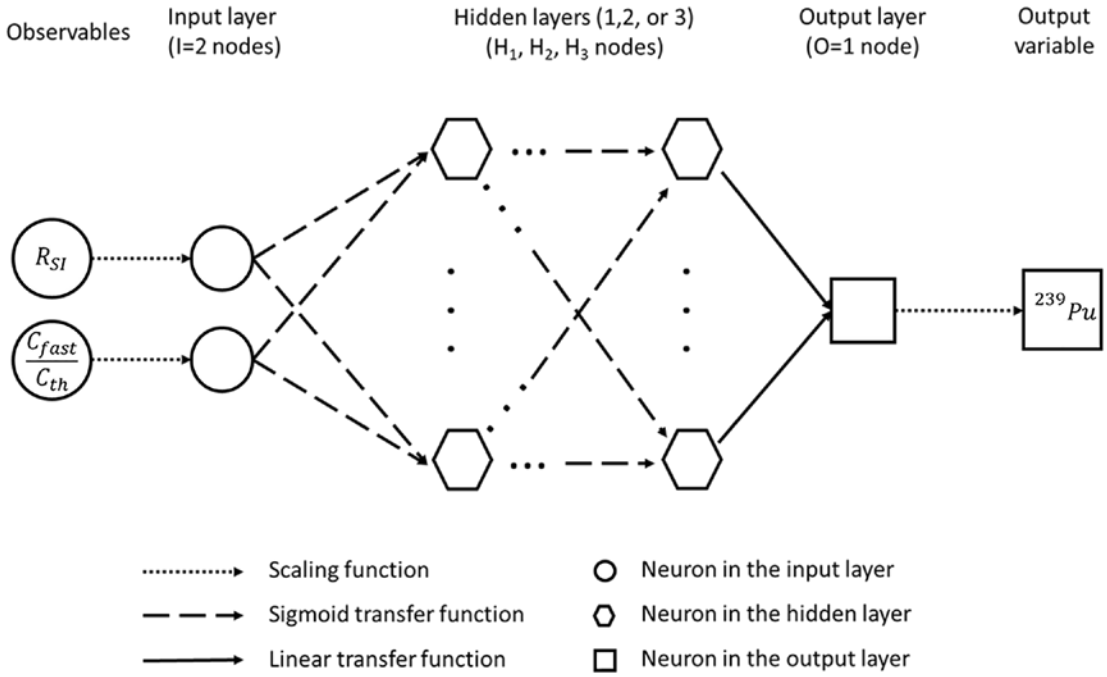

Figure 4: Architecture of the Neural network considered in this work.

3. Data analysis with artificial neural networks

3.1 Artificial Neural Networks

In addition to the above mentioned approach, we decided to investigate the use of artificial neural networks [12] as mean to determine the ^{239}Pu quantity given the two observables R_{SI} and C_{FAST}/C_{TH}.

An ANN can be described as a network in which each node (or neuron) *i* processes the *n* input units it is connected to through a transfer (or activation) function f_i :

$$y_i = f_i\left(\sum_{j=1}^{n}(w_{ij}\cdot x_j - \theta_i)\right) \quad (1)$$

where y_i is the output of neuron *i*, x_j is the *j*-th input to node *i*, w_{ij} is the weight of the connection between input *j* and node *i,* and θ_i is the threshold (or bias) of the node. While each neuron *i* can have its own transfer function in our implementation [13, 20] the same transfer function was used for all the neurons in a given layer.

Neural networks have a multilayer architecture consisting of one layer for input neurons, one or more inner layers of neurons (also called hidden layers), and one layer for output neurons. The architecture chosen in this work is represented in Fig. 4 and consists up to three hidden layers. The number of nodes in the input layer is indicated with *I*, the number of nodes in the hidden layer number k is indicated with H_k, and the number of nodes in the output layer is indicated with *O*.

In this architecture, the input variables (Observables) are linearly scaled between -1 and +1 before being fed to the ANN. Sigmoid functions are used to connect the neurons in the input layer to the neurons in the first hidden layer, as well as to connect the neurons in the different hidden layers. Linear functions are used to connect the neurons in the last hidden layer to the neurons in the output layer. Finally the output from the neurons of the output layer is transformed into the output variable (^{239}Pu mass) with the inverse of the linear scaling function used for the considered observables.

The database of simulated observables and spent fuel characteristics is divided in three sets, corresponding to training, validation and testing. The training process of a neural network is an iterative process where the weights and biases of each neuron are adapted as result of the predictive error. Using an initial set of weights and biases, the training set is used by the training algorithm to calculate the predictive error and to adapt the weights and biases of the neurons. The predictive error is also computed for the validation set for each iteration during the training process. The predictive error for the training set and validation set normally decreases with the number of iterations but, as the network begins to overfit the dataset, the error in the validation set tends to increase. The weights and biases of the neurons in the trained network are those obtained for the minimum value of the predictive error in the validation set. The testing set is finally used to determine the accuracy of the trained ANN and to evaluate its capability to predict results from data it was not trained with. [21]

3.2 Data analysis of SINRD signatures

We considered only SINRD observables for cases with CT of 5 years, given the weak dependence on the CT up to a CT value of 10 years. The dataset is therefore reduced to 98 entries associated to 14 values of BU and 7 IE.

The size of the data set is relatively small when compared to the large data sets that are usually used when training an ANN; however, this is in line with the fact that, in view of a deployment of the ANN with experimental data, the data set would also not be large when considering realistic combinations of IE and BU values.

Starting from Eq. (1) we estimated the number of parameters of the ANN that need to be estimated during the training procedure as a function of the network structure. The results are shown in Table 1 and indicate the number *N* of parameters as a function of the number of nodes *I* in the input layer, the number of nodes H_k in the hidden layer number *k*, and the number of nodes *O* in the output layer. Different configurations with *k* between one and three were considered with a minimum level of complexity, in view of the limited availability of training data.

In this work we use an architecture where the two observables enter the input layer, and the ^{239}Pu amount is the only quantity in the output layer. Therefore for our case *I*=2, representing the two SINRD observables, and *O*=1, representing the ^{239}Pu amount.

In practice, the data processing with ANN consists in identifying a ANN configuration that describes the dependence of ^{239}Pu varies in the space of the variable C_{FAST}/C_{TH} and R_{SI}.

I	H_1	H_2	H_3	O	N
2	3			1	13
2	2	2		1	15
2	2	2	2	1	21

Table 1: Number n of the ANN parameters to be determined as a function of the network architecture.

For a given ANN configuration, there is a level of arbitrarity when choosing the size of training, testing and validation. In our case, given the limited size of the whole database and the limited possibilities to carry out actual measurement we decided to limit the size of the training and validation set to 10 entries each; the rest of the database was used for testing.

Since the number *N* of the network parameters should not exceed the size of the training and validation data set we opted for a network with two hidden layers with two nodes each. The choice of two layers stems from previous experience where we learned that better performance can be achieved when the number of layers is increased [13, 20].

The analysis of the data was carried with a tool [20] developed in MATLAB [22]; the tool allows to carry out the analysis through a graphical user interface (GUI); through this GUI the user can import data from a text file, filter the data based on certain criteria, define the network architecture and several optimization options such as internal processing functions, performance function and training function [20]. The results and network configuration can be exported. The tool allows training with random or fixed initial values for weights and offset. Also the entries of the database to be used for training, validation can be chosen randomly by the programme or by the user via flags associated to entries in the database.

In our analysis, the optimization of the ANN through the quantity mean square error (*mse)*

$$mse = \frac{1}{N}\sum_{k=1}^{N}\left(A_{k,calc} - A_k\right)^2 \qquad (2)$$

Where $A_{k,calc}$ is the value of the parameter as determined by the ANN in the output layer, A_k is the nominal value of

the parameter. After each iteration (also called epoch) the weights and biases of the nodes were updated according to the Levenberg-Marquardt [23,24,25] or Bayesian regularization [26,27] algorithms as implemented in Matlab with the *trainlm* and *trainbr* functions, respectively. The value of the parameters used in the both algorithms are included in Table 2.

Maximum number of epochs	10^5
Maximum time to train (in seconds)	1000
Network performance goal	0
Minimum performance gradient	10^{-7}
Maximum value for the Marquardt adjustment parameter (mu)	10^{10}

Table 2: Parameters used for the training algorithms.

In our analysis we tested the option not to include the scaling function described in Fig. 4 between observables and input layer and between output layer and output variables. This test resulted in worse values of the *mse* when compared with an analysis that include this scaling step.

3.3 Results

Initially we kept random initial values for weights and offset as well as the entries of the database to be used for training, testing and validation. We observed a large variation in the number of epochs before the training timing ended as well as a variation of several orders of magnitude in terms of *mse.*

We realized that it is impossible to identify the configuration with the minimum *mse* based on a random or sequential selection of the database entries. Assuming that the assignment of an entry to the validation or training data set does not matter, with 20 entries in 98 this would correspond to

$$\binom{n}{k} = \frac{n!}{k!(n-k)!} = \frac{98!}{20!(78)!} \sim 3\times10^{20}$$

combinations.

With the used data analysis tool, both the initial values for weights and offset as well as the entries for training and testing can be defined by the user or chosen randomly.

Since weights and offset define the ANN to be trained, the choice of the initial values of weights and offset was kept random.

We then tried to identify, by expert judgement and hence natural intelligence, the entries of the database. The choice of the entries was carried out by studying how the ^{239}Pu varies in the space of the variable C_{FAST}/C_{TH} and R_{SI}. This is shown in Fig. 5.

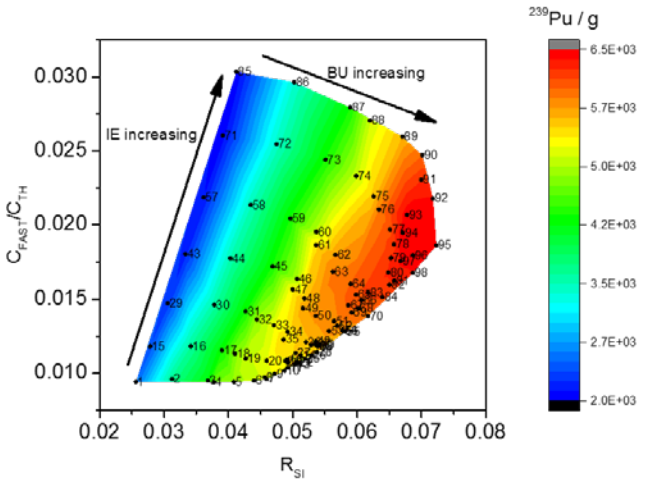

Figure 5: ^{239}Pu amount as a function of R_{SI} and C_{FAST}/C_{TH}. The number indicate the corresponding entry in the considered data set.

The data in Fig. 5 reveal that C_{FAST}/C_{TH} and R_{SI} have a limited range of variation and lie in specific domain. As explained before, we are looking for a ANN configuration that describes the dependence of ^{239}Pu in the space of the variables C_{FAST}/C_{TH} and R_{SI}. Given the results in Fig. 5, it was logical to assume that entries to use in the training and validation data set should lie at the boundary of the domain of C_{FAST}/C_{TH} and SINRD. In addition, it seemed logical that a sufficient number of them should lie inside the area in order to allow to describe the shape over the domain of C_{FAST}/C_{TH} and R_{SI}.

Based on these criteria, we defined the entries for the training validation data set as indicated in the Table 3 and Fig. 6. It is worth to comment that the entries indicated in italic, although present in the spent fuel library, are not realistic since the BU is too high for the chosen IE. These entries were nevertheless considered to assess the performance of the method in a configuration where all the entries of the database of spent fuel library observables can be used.

The training was then repeated one hundred times to try different initial values for weights and offset.

It was found initial values for weights and offset can affect the *mse* up to two order of magnitude; this corresponds to about 1 order of magnitude change in the resulting ^{239}Pu mass standard deviation.

The best obtained value of *mse* was 2.3×10^4. The square root of *mse* corresponds to a standard deviation between declared and predicted of ^{239}Pu about 150 g. Changing the training function between *trainlm* and *trainbr* did not seem to affect the results.

The deviation between the predicted ^{239}Pu mass and the value in the data base is shown in Fig. 7, where the entries used for training, validation and testing are shown with different colours.

ID	Flag	BU	IE	CT		ID	Flag	BU	IE	CT
1	T	5	2	5		**5**	V	25	2	5
28	T	*70*	*2.5*	*5*		**29**	V	5	3	5
31	T	15	3	5		**35**	V	35	3	5
59	T	15	4	5		**45**	V	15	3.5	5
63	T	35	4	5		**57**	V	5	4	5
75	T	25	4.5	5		**64**	V	40	4	5
78	T	40	4.5	5		**70**	V	*70*	*4*	*5*
85	T	5	5	5		**87**	V	15	5	5
89	T	25	5	5		**91**	V	35	5	5
95	T	55	5	5		**93**	V	45	5	5

Table 3: Selected entries for training (T) and validation (V) data sets.

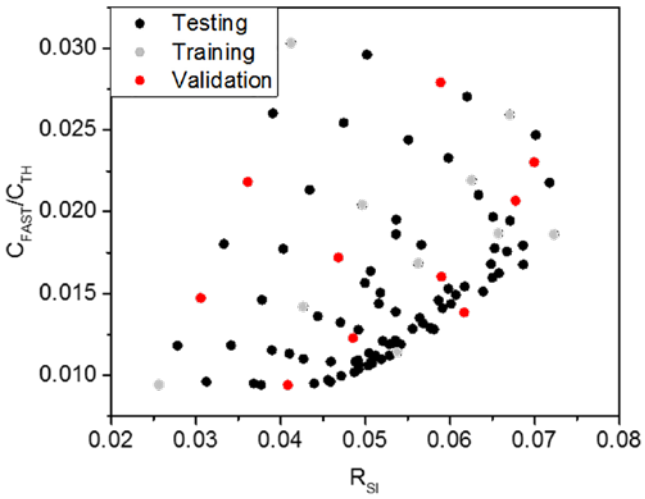

Figure 6: Training, validation and testing data sets.

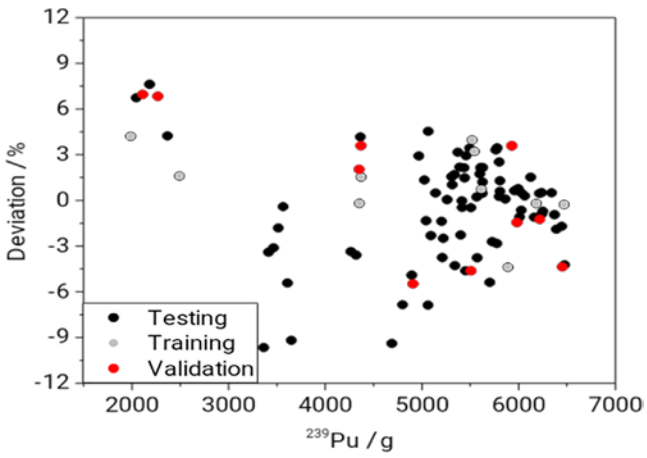

Figure 7: Percentage deviation between predicted and nominal ^{239}Pu amount for training, validation and testing data sets.

In the testing data set, the average deviation between the nominal ^{239}Pu content and the calculated one was 0.2% with a standard deviation of 3.5% and a maximum deviation of 10%.

4. Conclusions

We described a data analysis approach based on artificial neural networks (ANN) to process the observables associated to the SINRD technique. The SINRD observables were obtained with Monte Carlo based simulations using fuel composition from a spent fuel library and represent a data set of nearly 3,000 entries.

Given the fact that the SINRD observables are not depending on cooling time up to a cooling time of 10 years, we restricted the analysis to the 98 entries with a cooling time of 5 years.

While the choice of the initial values of weights and offset was kept random, we identified by expert judgement and hence natural intelligence, the 20 entries of the database to be used for training and validation. The obtained results reveal that, the average deviation between the nominal ^{239}Pu content and the calculated one was 0.2% with a standard deviation of 3.5% and a maximum deviation of 10%.

The selection of spent fuel assemblies based on expert judgement is not necessarily the best, in terms of ANN precision, but allowed to resolve quickly a problem that would have not been possible to solve by selecting on a randomly the database entries for training and validation.

Future work will focus on possibly reducing even further the size of the data base for training and validation and limiting only on realistic cases of the library of observables. In addition, we would like to study a different form of the performance function for example accounting for the relative deviations rather than absolute deviations. We would like also to analyse data with different cooling times by including an additional observables from the observable database in the data analysis.

5. References

[1] D. Reilly, N. Ensslin, H. Smith Jr. and S. Kreiner, *Passive Nondestructive Assay of Nuclear Materials*, NUREG/CR-5550, LA-UR-90-732, 1991

[2] H. Würz, *A Simple Non-Destructive Measurement System For Spent Fuel Management*, Nuclear Technology 95 (1991) pp 193-206

[3] Park W. S., et al., 2014. *"Safeguards by design at the encapsulation plant in Finland"*. Proceedings of the 2014 IAEA safeguards symposium.

[4] European Council Decision 2006/976/Euratom of 19 December 2006

[5] *Coordinated Technical Research Meeting on Spent Fuel Verification Methods*, IAEA March 3-6 2003

[6] A. Borella, et al., *Advances in the Development of a Spent Fuel Measurement Device in Belgian Nuclear Power Plants*.- In: Symposium on International Safeguards, Linking Strategy, Implementation and People, Book of Abstracts, Presentations and Papers, 2014, IAEA, Vienna, Austria, p. 272

[7] R. Rossa, *Advanced non-destructive methods for criticality safety and safeguards of used nuclear fuel,* PhD thesis at Université libre de Bruxelles, September 2016.

[8] S. Tobin, H. Menlove, M. Swinhoe, M. Schear, *Next Generation Safeguards Initiative research to determine the Pu mass in spent fuel assemblies: Purpose, approach, constraints, implementation, and calibration*, Nuclear Instruments & Methods In Physics Research Section A, 2011, doi 10.1016/j.nima.2010.09.064

[9] T. White, et al., 2018. "Application of Passive Gamma Emission Tomography (PGET) to the inspection of spent nuclear fuel". Proceedings of the 2018 INMM annual meeting.

[10] H. Menlove, C. Tesche, M. Thorpe and B. Walton, *A Resonance Self-Indication Technique for Isotopic Assay of Fissile Materials*, Nuclear application Vol. 6 April 1969 pp 401-408

[11] Rossa, R., Borella, A. & van der Meer, K. *Investigation of the Self-Interrogation Neutron Resonance Densitometry applied to spent fuel using Monte Carlo simulations* Jan 2015 In : Annals of Nuclear Energy. 75, p. 176-183

[12] Leshno, M., Lin, V. Y., Pinkus, A., & Schocken, S., *Multilayer feedforward networks with a nonpolynomial activation function can approximate any function*, Neural networks, 6(6):861-867, 1993.

[13] Borella, A., Rossa, R. & Turcanu, C, *Signatures from the spent fuel: simulations and interpretation of the data with neural network analysis,* 1 Dec 2017 In : ESARDA Bulletin. p. 29-38 10 p.

[14] Rossa R., Borella A., Labeau P.E., Pauly N., van der Meer K., Neutron absorbers and detector types for spent fuel verification using the self-interrogation neutron resonance densitometry, Nuclear Instruments and Methods in Physics Research A 791 (2015), 93-100.

[15] D.B. Pelowitz, Ed., "MCNPX Users Manual Version 2.7.0"LA-CP-11-00438 (2011).

[16] R. Rossa., et al., *Development of a reference spent fuel library of 17x17 PWR fuel assemblies*, ESARDA BULLETIN, No. 50, December 2013

[17] A. Borella, et al., *Extension of the SCK•CEN spent fuel inventory library*, 37th ESARDA Annual Meeting, 2015

[18] A. Borella, M. Gad, R. Rossa, K. van der Meer, *Sensitivity Studies on the Neutron Emission of Spent Nuclear Fuel by Means of the Origen-ARP Code*, In: Proceeding of the 55th INMM Annual Meeting, Atlanta, Georgia, United States, July 2014.

[19] Borella, A., Rossa, R. & van der Meer, K. *Simulated observables for spent fuel non-destructive assay* 22 Jul 2018 Proceedings of the 2018 INMM annual meeting

[20] Zaïoun, H. *Analysis and interpretation of spent fuel signatures with an artificial neural network: Improvement of the network, based on the previous work, and development of a graphical user interface* 30 Mar 2018 Studiecentrum voor Kernenergie. 25 p. (SCK•CEN Reports; no. I-0687)

[21] https://nl.mathworks.com/help/deeplearning/ug/divide-data-for-optimal-neural-network-training.html

[22] https://www.mathworks.com/help/matlab/

[23] https://nl.mathworks.com/help/deeplearning/ref/trainlm.html

[24] Marquardt, D., "An Algorithm for Least-Squares Estimation of Nonlinear Parameters," SIAM Journal on Applied Mathematics, Vol. 11, No. 2, June 1963, pp. 431–441

[25] Hagan, M.T., and M. Menhaj, "Training feed-forward networks with the Marquardt algorithm," IEEE Transactions on Neural Networks, Vol. 5, No. 6, 1999, pp. 989–993, 1994.

[26] MacKay, David J. C. "Bayesian interpolation." Neural computation. Vol. 4, No. 3, 1992, pp. 415–447.

[27] Foresee, F. Dan, and Martin T. Hagan. "Gauss-Newton approximation to Bayesian learning." Proceedings of the International Joint Conference on Neural Networks, June, 1997.

Tamper-Indicating Enclosures with Visually Obvious Tamper Response

Heidi A. Smartt, Annabelle I. Benin, Cody Corbin, Joyce Custer, Patrick L. Feng, Matthew Humphries, Amanda Jones, Nicholas R. Myllenbeck

Sandia National Laboratories
Albuquerque, New Mexico, USA
P.O. Box 5800 MS1371 Albuquerque, NM, USA 87185
E-mail: hasmart@sandia.gov

Abstract:

Sandia National Laboratories is developing a way to visualize molecular changes that indicate penetration of a tamper-indicating enclosure (TIE). Such "bleeding" materials (analogous to visually obvious, colorful bruised skin that doesn't heal) allows inspectors to use simple visual observation to readily recognize that penetration into a material used as a TIE has been attempted, without providing adversaries the ability to repair damage. Such a material can enhance the current capability for TIEs, used to support treaty verification regimes. Current approaches rely on time-consuming and subjective visual assessment by an inspector, external equipment, such as eddy current or camera devices, or active approaches that may be limited due to application environment. The complexity of securing whole volumes includes: (1) enclosures that are non-standard in size/shape; (2) enclosures that may be inspectorate- or facility-owned; (3) tamper attempts that are detectable but difficult or timely for an inspector to locate; (4) the requirement for solutions that are robust regarding reliability and environment (including facility handling); and (5) the need for solutions that prevent adversaries from repairing penetrations. The approach is based on a transition metal ion solution within a microsphere changing color irreversibly when the microsphere is ruptured. Investigators examine 3D printing of the microspheres as well as the spray coating formulation. The anticipated benefits of this work are passive, flexible, scalable, cost-effective TIEs with obvious and robust responses to tamper attempts. This results in more efficient and effective monitoring, as inspectors will require little or no additional equipment and will be able to detect tamper without extensive time-consuming visual examination. Applications can include custom TIEs (cabinets or equipment enclosures), spray-coating onto facility-owned items, spray-coating of walls or structures, spray-coatings of circuit boards, and 3D-printed seal bodies. The paper describes research to-date on the sensor compounds and microspheres.

Keywords: tamper-indicating enclosures; international nuclear safeguards

1. Introduction

Tamper-indicating enclosures (TIEs)[1] are used in treaty verification regimes to detect access to an item of interest. Items of interest can include, but are not limited to, (1) inspectorate-owned equipment enclosures in which detecting access is desired to ensure trust in information stored or processed within the enclosure and (2) facility-owned enclosures containing nuclear materials that have been measured by inspectors and require maintaining continuity of knowledge in the absence of the inspector. Current deployed TIEs typically fall within three categories. The first are materials that an inspector will primarily visually inspect for signs of unauthorized access, such as the ubiquitous anodized aluminium enclosures that the IAEA deploys with the RMSA fiber loop seal, the NGSS surveillance system, legacy surveillance systems, and other monitoring equipment. The second category are active electronic methods/materials that continuously monitor the volume for signs of unauthorized access, such as the conductive foil within the EOSS fiber loop seal and the fiber mesh embedded in the enclosure of the NGSS. The third category are externally deployed indicators of penetration or access to materials, such as eddy current or imaging devices. Note that both the second and third category also require visual inspection. The limitations to these three categories are the subjective and time-consuming process of visually inspecting surfaces, the inability to deploy an active approach in some situations because of batteries or because of environmental conditions or facility requirements, and the limited materials able to be analysed by eddy current and potential inability to bring external equipment into a facility. Further, some approaches rely more on post-mortem analysis rather than in-situ verification.

The existing toolkit for TIEs is limited regarding the complex issues involved, and many technologies are old which may leave them more vulnerable. Simple visual approaches capable of high detection sensitivity have not received adequate research and development, although applications already exist that could benefit from such a capability. Sandia National Laboratories (SNL)

1 Note that TIEs are essentially volumetric seals. As such, they must have an integrity and identity element. The integrity element (tamper-indicating) is the thrust of this work. The identity element will be addressed separately.

recognizes these limitations and is developing “bleeding” materials (analog of visually obvious colorful bruised skin that doesn’t heal) that provide inspectors the ability to readily recognize using simple visual observation that penetration into the material has been attempted without providing adversaries the ability to repair damage. Such material can significantly enhance the current capability for TIEs, used to support treaty verification regimes.

SNL’s approach is research and development of cargo-loaded microspheres embedded in 3D-printed structures or spray-coated onto existing surfaces, that when penetrated or tampered, cause an irreversible color change that is visually obvious[1]. Work comprises the following general tasks: (1) sensor and microsphere development and optimization (i.e., intensity of response, surface area of response, and microsphere composition, size, wall thickness, rupture point), (2) integration of transition metal-loaded microspheres into 3D-printed, spray-coated, or moulded geometries, and (3) testing and evaluation of prototypes, including environmental and industrial considerations. The anticipated benefits of this work are passive, flexible, scalable, cost-effective TIEs with obvious and robust responses to tamper attempts. These responses result in more efficient and effective monitoring as inspectors will require little or no additional equipment and will be able to detect tampering without extensive time-consuming visual examination. Applications can include custom TIEs (cabinets or equipment enclosures), spray-coating onto facility-owned items, spray-coating of walls or structures, spray-coatings of circuit boards, and 3D-printed seal bodies.

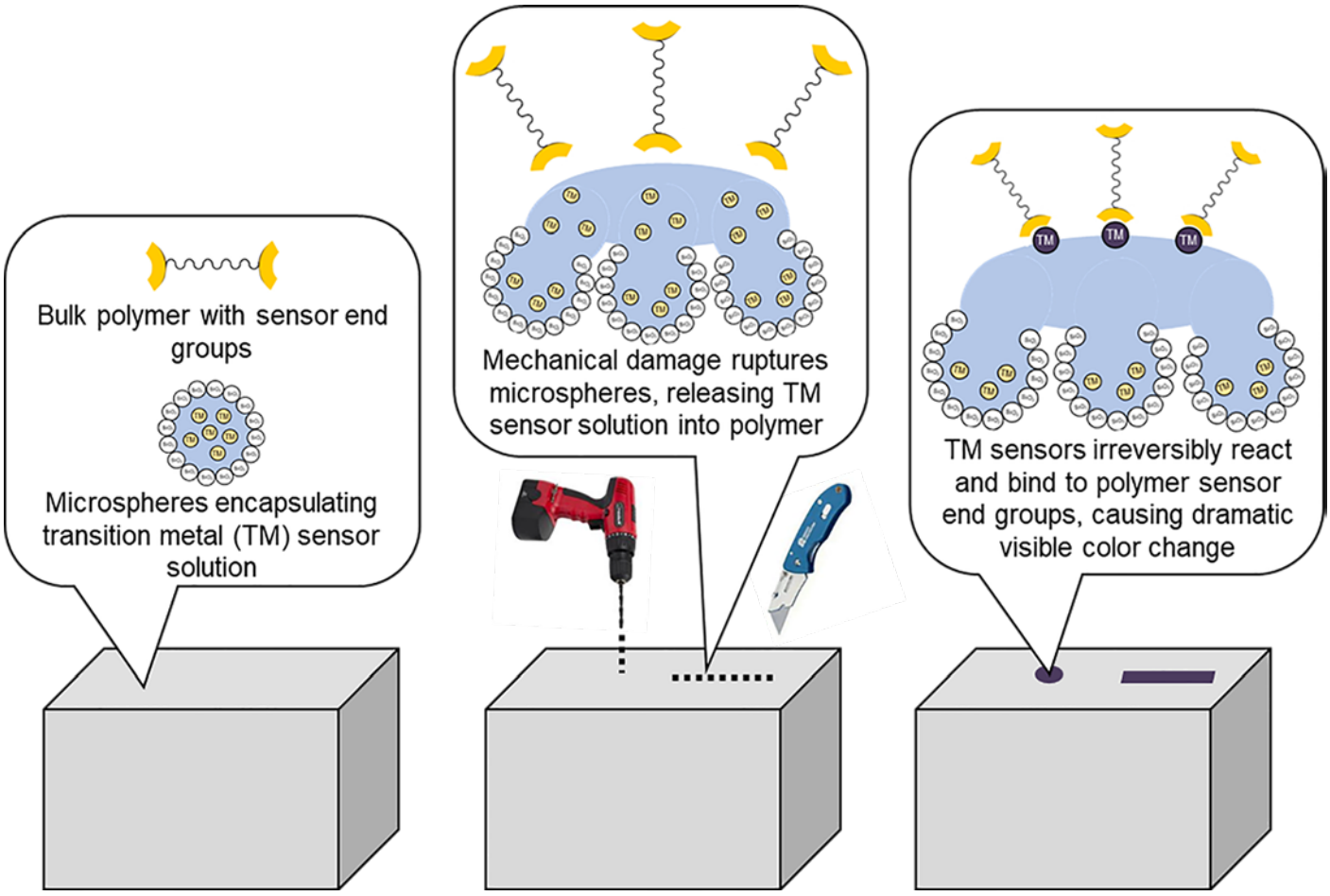

Figure 1: General schematic of R&D concept. A two-phase material consisting of a sensing polymer and transition-metal encapsulated microspheres are 3D-printed or spray-coated on to a unique geometry. Upon tampering, the microspheres rupture and the two sensor components interact to form an irreversible visible color change.

2. R&D of sensor compounds

Transition metal complexes consist of a transition metal center derived from a metal salt (e.g. $FeCl_3$) and an organic molecule. The combination of these components can lead to dramatic and highly visible color changes which may be utilized for sensing application spaces. The initial approach for the goal of this project was to perform a scoping study with various 3d transition metals with one organic sensor (2,6-bis(10-methyl-benzimidazolyl)-4-hydroxypyridine, (HO-Bip)) to establish a qualitative evaluation of color change.[2,3] Figure 2 presents these results along with the chemical structure of the sensor that was utilized.

Once the plausibility of the mechanism was confirmed, our second goal was to make a series of transition metal complexes with a commercially available sensor. The compound 5,6-epoxy-5,6-dihydro-[1,10]-phenanthroline (Ephen) was chosen as the sensor because it is cheap, colorless, and can be easily polymerized using various methods. The series of transition metal complexes were prepared via combining dilute solutions of the metal salts ($CrCl_3$, $Mn(OAc)_3$, $FeCl_2$, $FeCl_3$, $CoCl_2$, $CuCl_2$, $NiCl_2$, and $ZnCl_2$) with a dilute solution of Ephen in a 1:1 molar ratio. This ratio was chosen because it represents the minimum binding of the sensor to the metal salt. Two common solvents were investigated, methanol and dimethyl sulfoxide (DMSO). These solvents were chosen as these are expected to have good penetration into epoxy-based polymeric materials while also allowing efficient solubility of the metal salts.

Figure 3 shows the results of mixing $FeCl_2$, $FeCl_3$, $CoCl_2$, and $CuCl_2$ with the sensor, Ephen. The other metal salts, $CrCl_3$, $Mn(OAc)_3$, $NiCl_2$, and $ZnCl_2$, did not yield an easily visible color change in either solvent. All solutions from Figure 3 have concentrations of 10 mM except the

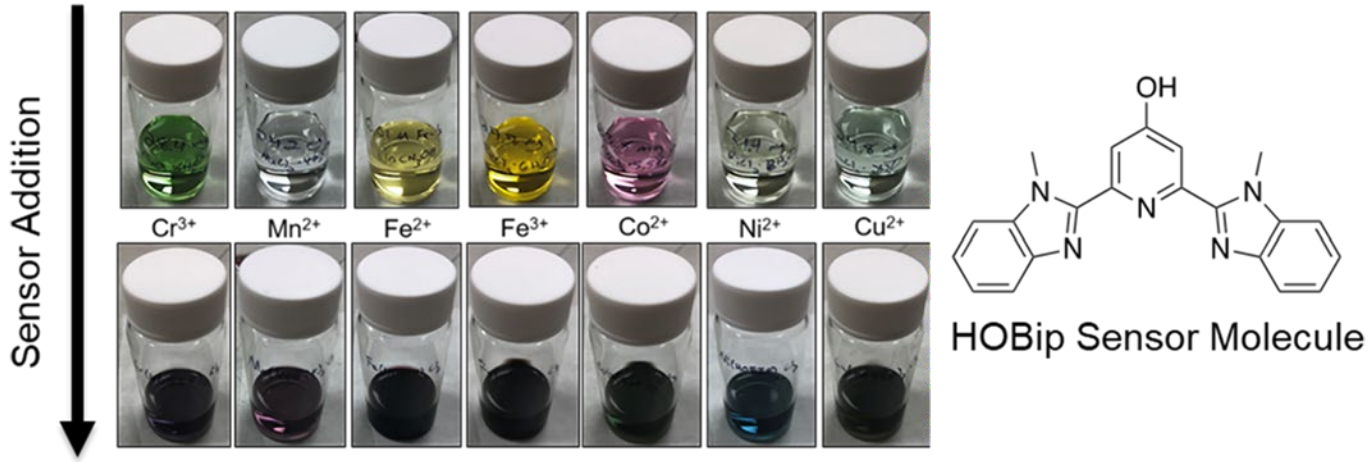

Figure 2: Qualitative scoping study results on 3d transition metal color changes with addition of organic sensor in methanol. All metal solutions get significantly darker, and many have a dramatic color change.

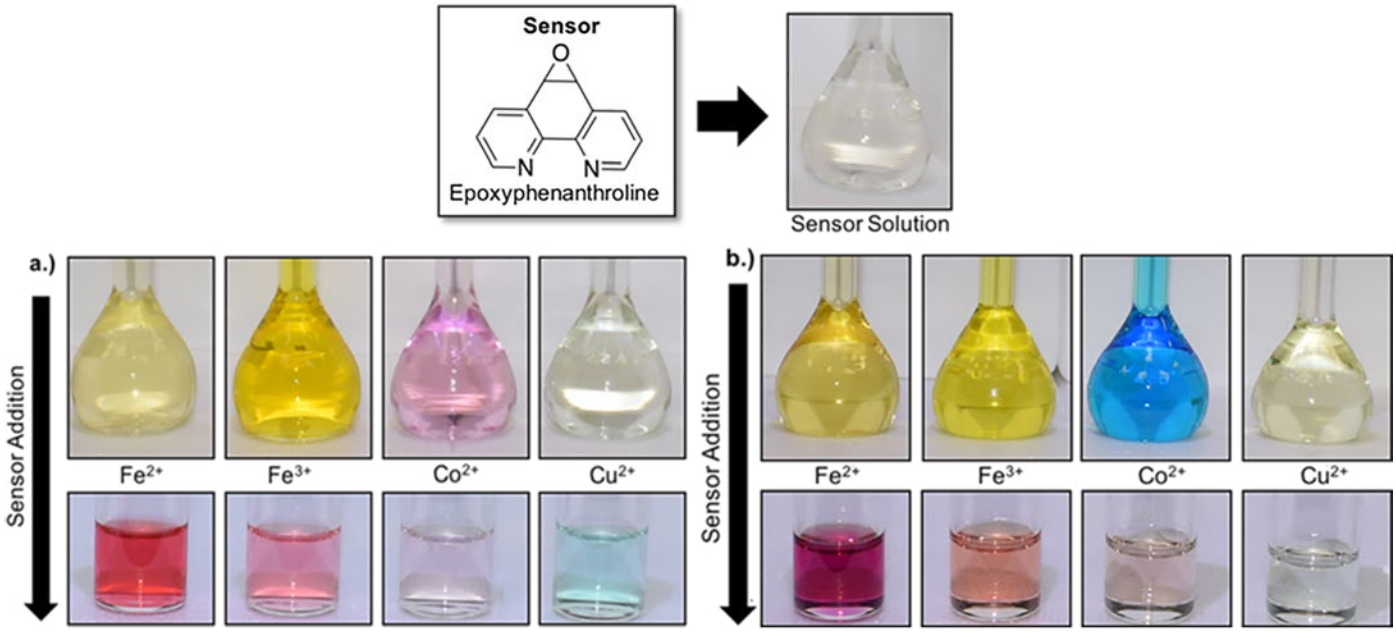

Figure 3: Colorless sensor solution in both methanol and DMSO (top); (a) addition of sensor solution to various metal salt solutions in a 1:1 molar ratio in methanol; (b) addition of sensor solution to various metal salt solutions in a 1:1 molar ratio in DMSO.

Fe^{3+} ($FeCl_3$), which had to be diluted to 2 mM. The transition metal complexes formed when mixing the Ephen sensor with the Fe^{2+}, Fe^{3+}, and Co^{2+} solutions, all of which produced dramatic and visibly obvious color changes.

A more quantitative look at the color changes is shown in Figure 4. The solutions above were analyzed by UV-Visible absorbance spectroscopy and the results were plotted as a function of wavelength. The two most intense transitions occur with the Fe^{2+} and Co^{2+} ions. In the case of Fe^{2+} where the solution initially absorbs around 375 nm (visibly yellow), addition of the sensor dramatically shifts the absorbance to around 510 nm (visibly red). The Co^{2+} DMSO solution on the other hand begins as an intense, broad peak between 550 nm and 750 nm (visibly blue) and addition of the sensor produces a broad, weak absorbance around 500 nm. The other solutions do not produce such intense transitions.

The most visibly obvious color changes occurred in the solutions of Fe^{2+} and Fe^{3+} in both methanol and DMSO. The Co^{2+} transition was also visibly obvious but only occurred in DMSO. The next goal is to physically incorporate these sensor molecules into a polymer backbone (Figure 5) and to investigate the stability of these complexes over time in air, over heat, and in the presence of corrosive materials. Radiation testing will also be a major characterization required for the safeguards application space, and the R&D in progress has been designed to utilize robust materials. More specifically, thermoset (cross-linked) materials are being prepared instead of thermoplastic materials, which can melt/degrade much quickly over time. The molecular structure of the thermoset materials will also aid in mitigating radiation damage.

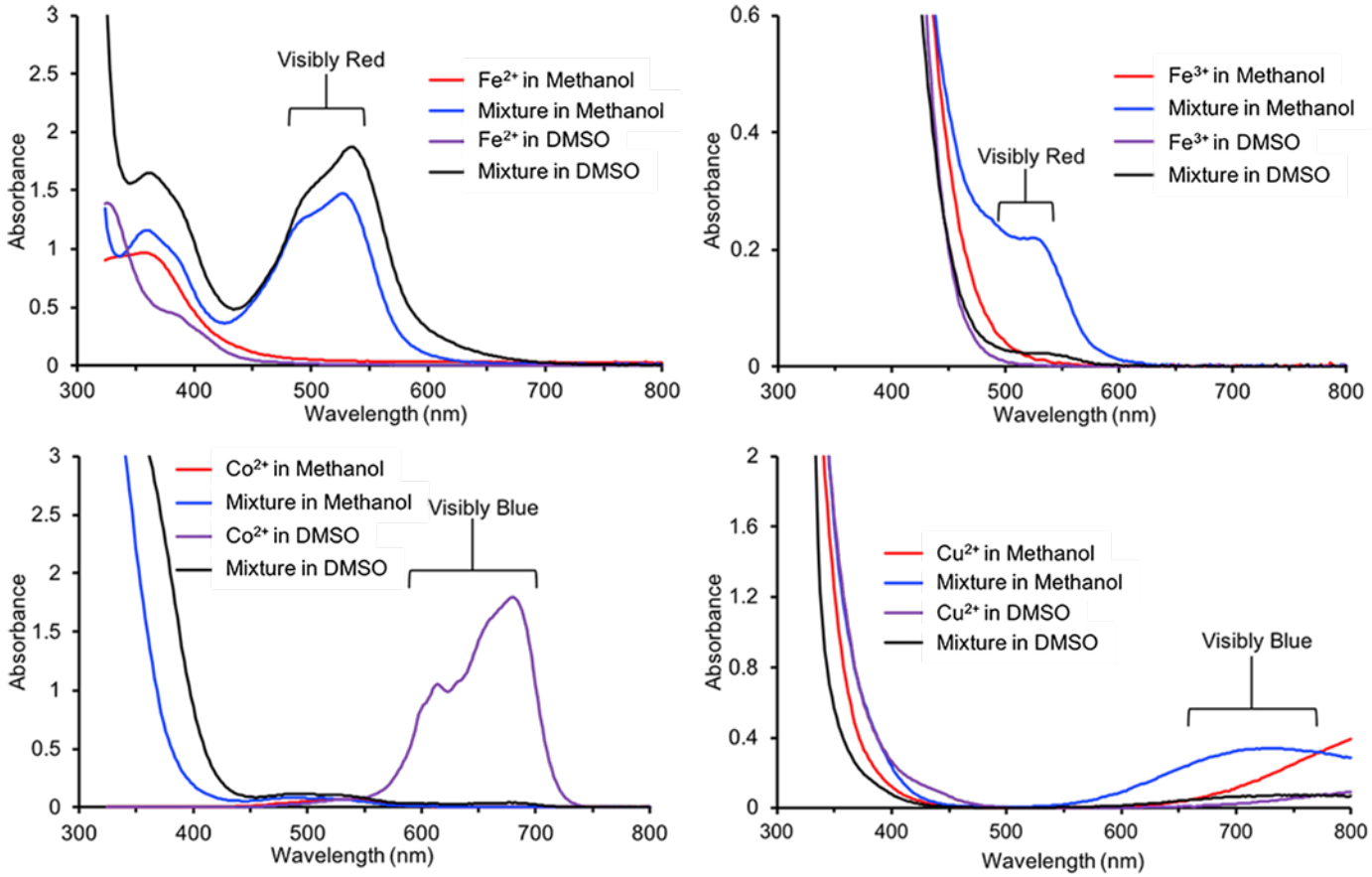

Figure 4: UV-Visible absorbance spectroscopy of Fe^{2+} (top left), Fe^{3+} (top right), Co^{2+} (bottom left), and Cu^{2+} (bottom right) before and after addition of the sensor. The visible colors of the most intense peaks are labeled.

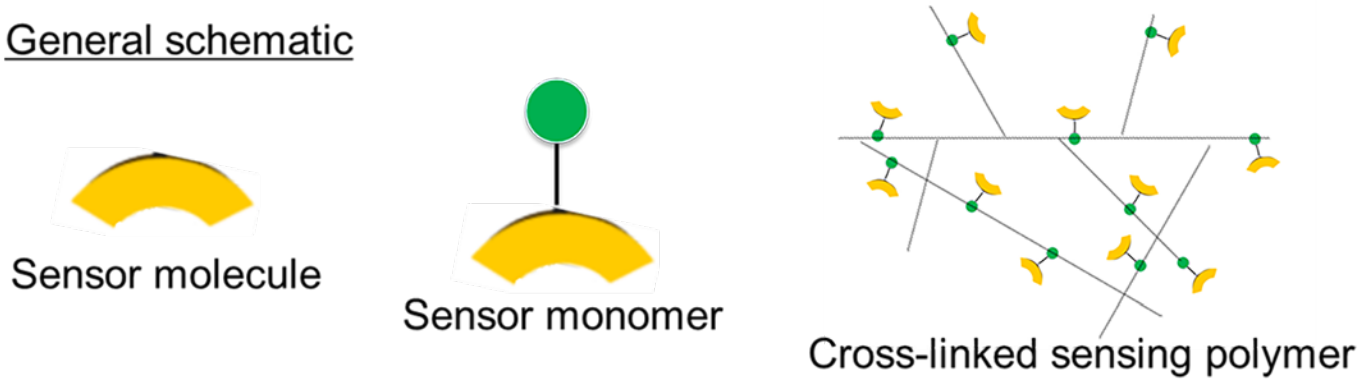

Figure 5: General schematic of incorporation of organic sensor into polymeric material. Both UV-curable and heat-curable materials will be prepared and evaluated.

3. Development of microspheres

A variety of wet chemistry microsphere synthetic methods have been developed in the literature in which capsule formation is carried out in liquid medium, starting from a solution, a liquid-in-liquid emulsion, or a solid-in-liquid suspension.[4] Template materials are often employed to direct the size and shape of the products during synthesis. One templating strategy involves the use of "soft" templates that are sensitive to synthesis parameters such as temperature, pH, solvent polarity, etc. and have been demonstrated to form hollow nano- and microstructures composed of SiO_2, carbons, polymers, metals, metal oxides, etc.

Our efforts focus on the use of emulsion templates. Emulsions are defined as two immiscible liquids (usually hydrophobic and hydrophilic pairs) where small droplets of one liquid are finely distributed within another continuous liquid phase. Emulsions can be oil-in-water (o/w) or water-in-oil (w/o), and surfactant compounds are often required to assemble at the interface of the two liquids to decrease the interfacial tension and increase thermodynamic stability. Precursor species for the microsphere shell self-assemble (often with the aid of co-surfactants) at the interface of the droplets and the continuous phase and the shell can subsequently be formed through, for example, polymerization. This method can produce spheres in the nano- to micron-size regime. Cargo species of interest can be incorporated in one step into the microspheres through solubilization within the emulsion droplets.[4,7]

The requirements for the microsphere wall material are primarily structural in nature, serving to mechanically contain the cargo compound. The structural properties of the microsphere must be commensurate with the strains expected for the particular application, i.e. they must be sufficiently robust to withstand 'normal' environmental conditions yet able to rupture under tampering conditions. These properties are associated with the intrinsic tensile properties of the wall material itself, as well as the wall thickness and microsphere radius. Based on these criteria, three types of candidate materials were down-selected for investigation and optimization: polymeric, siliceous, and polymer-silica core-shell composites.

Three different polymeric materials were studied: Urea-Formamide (UF), Melamine-Urea-Formamide (MUF), and Poly(methyl methacrylate) (PMMA).[5] The first two materials are copolymers prepared by o/w emulsion polymerization procedures, whereas the third entry comprises a homopolymer microsphere prepared via an evaporation/phase-separation procedure. Microspheres ranging in diameter from 10 – 250 µm were synthesized and filled with the different mobile phase materials such as mineral oil and hexadecane.

Of the three materials studies, UF microspheres performed the best due to several properties: robust synthetic method that afforded the capsules in high yield, a relatively narrow size distribution, uniform particle surface properties, synthetically adjustable sizes across a wide range, and compatibility with all of the tested mobile phase materials. The above combination of desirable attributes was not exhibited by either the MUF copolymer or PMMA microspheres, in spite of other advantages such as higher thermal stability and lower diffusivity in the case of MUF.

The development of a variety of microspheres with different structural properties would provide a flexible selection of materials to coincide with the mechanical characteristics/detection sensitivity of the corresponding tamper-indicating device design. Siliceous systems were subsequently studied to impart increased mechanical strength into the microsphere walls.

Silica microcapsules were prepared by the acid-catalyzed hydrolysis of tetraethyl orthosilicate (TEOS) in a w/o emulsion.[6] Stirring speed and method during the reaction had a large effect on the microsphere size and purity, as shown in Figure 7 below. Overhead stirring at 1000 rpm with

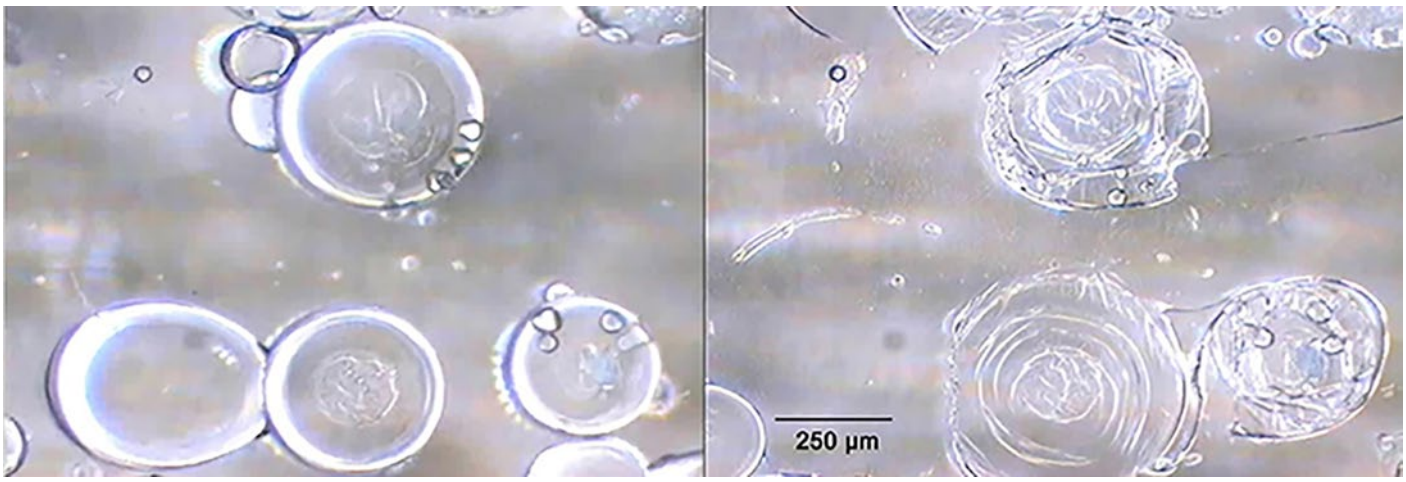

Figure 6: Video microscope screen capture images depicting intact (left) and ruptured (right) mineral oil-filled UF microspheres. The mechanical stimulus was exerted by a micro-manipulator tip pressing on the top plate of a microscope cover slip.

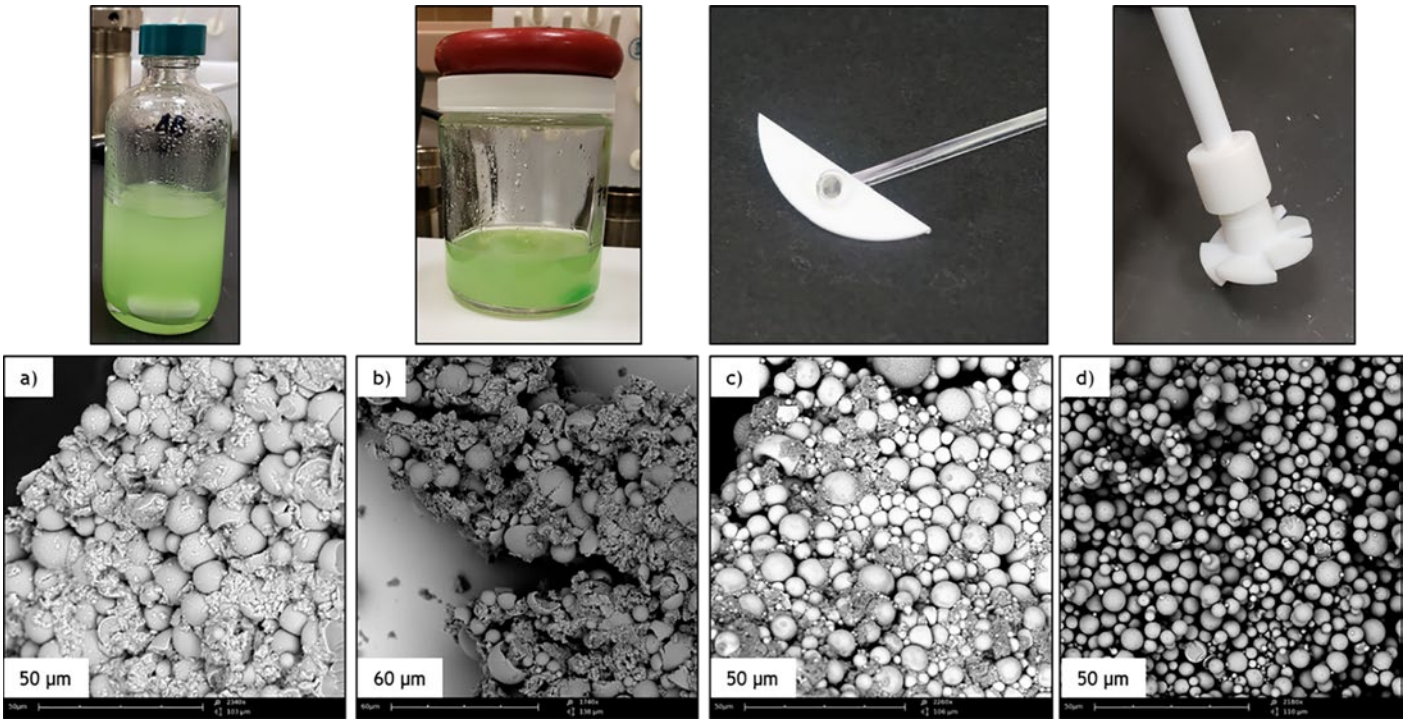

Figure 7: Scanning Electron Micrographs (SEMs) of silica microsphere products a) with magnetic stirring in a narrow glass bottle b) magnetic stirring in a wide glass jar c) overhead stirring in a glass round bottomed flask with a paddle impeller and d) overhead stirring in a plastic bottle with a propeller impeller.

a propeller impeller provided the best shear conditions to produce clean silica microspheres with a roughly trimodal size distribution of 0.5 - 1, 2 - 5, and 10 µm. Cu^{2+} and Fe^{3+} transition metal ions were successfully encapsulated as cargo in the aqueous mobile phase.

Crushing and grinding of these dried microspheres between two glass slides showed very little to no breakage, pointing towards the high mechanical strength of the silica microspheres compared to polymeric. It is well known, however, that silica microspheres contain micro- and mesoporosity,[6] which is undesirable for long term containment of cargo molecules. Our next efforts will focus on combining the low permeability of the polymers with the mechanical strength of the silica to form a core-shell polymer-silica composite microsphere material.

4. Summary and Next Steps

SNL continues to develop a material that results in an obvious, visual response (irreversible color change) upon tamper. The material will be 3D-printed for customizable inspection equipment, or spray-coated for application to facility-owned equipment. The material adds to the TIE toolbox, which is currently limited in options. R&D will continue on transition metals and microspheres, culminating in

the integration of the transition metals and microspheres into 3D-printed and spray-coated prototypes. The prototypes will undergo environmental testing upon fabrication. Future testing for durability and vulnerability will also be conducted.

5. Acknowledgements

The authors would like to acknowledge the U.S. National Nuclear Security Administration (NNSA) Office of Defense Nuclear Nonproliferation R&D Safeguards portfolio for funding and supporting this research.

Sandia National Laboratories is a multi-mission laboratory managed and operated by National Technology and Engineering Solutions of Sandia, LLC, a wholly owned subsidiary of Honeywell International, Inc., for the U.S. Department of Energy's National Nuclear Security Administration under contract DE-NA0003525. SAND2019-2728 R.

6. References

[1] Smartt, H.A., Corbin W., Feng, P.L., Myllenbeck, N., Patel, S. *Tamper-Indicating Enclosures with Visually Obvious Tamper Response*, Proc. of Symposium on International Nuclear Safeguards, Vienna, Austria, 2018.

[2] Balkenende, D. W. R.; Coulibaly, S.; Balog, S.; Simon, Y. C.; Fiore, G. L.; Weder, C. *Mechanochemistry with Metallosupramolecular Polymers*, J. Am. Chem. Soc., **136**, 10493-10498, 2014.

[3] Rowan, S. J.; Beck, J. B. *Metal-ligand induced supramolecular polymerization: A route to responsive materials*. Faraday Discuss., **128**, 43-53, 2005.

[4] Prieto, G., Tüysüz, H., Duyckaerts, N., Knossalla, J., Wang, G.-H., Schüth, F. *Hollow Nano- and Microstructures as Catalysts*, Chem. Rev., **116**, 14056–14119, 2016.

[5] Smartt, H. A., Feng, P. L., Romero, J. A., Gastelum, Z. N. *Tamper-Indicating Enclosures Based on "Bleeding" Microcapsules*, SAND2015-8131.

[6] Wang, J-X, Wang, Z-H, Chen, J-F, Yun, J. *Direct encapsulation of water-soluble drug into silica microcapsules for sustained release applications*, Mater. Res. Bull., **43**, 3374-3381, 2008.

[7] Zhang, Y., Hsu, B.Y.W., Ren, C., Li, X., Wang, J. *Silica-based nanocapsules: synthesis, structure control and biomedical applications*, Chem. Soc. Rev., **44**, 315-335, 2015.

Identification of copper canisters for spent nuclear fuel: the ultrasonic method

Chiara Clementi[1,2], Lorenzo Capineri[2], François Littmann[1]

[1] Nuclear Security Unit, Joint Research Centre, European Commission, Ispra (VA), Italy
[2] Dept. Information Engineering, University of Florence, Florence, Italy
E-mail: chiara.clementi@ec.europa.eu, francois.littmann@ec.europa.eu, lorenzo.capineri@unifi.it

Abstract:

The long-term storage of spent nuclear fuel in geological repositories has introduced the need to develop new safeguards procedures, measures and technologies. For the proposed Swedish disposal process, the Continuity of Knowledge (CoK) of fuel during transport from Oskarshamn and deposition of the same copper canisters at Forsmark is a challenging topic. Several Containment and Surveillance (C/S) measures could be used for this purpose; among them, the identification and authentication of copper canisters could be useful to trace canisters during transport. Ultrasonic techniques are used by authors to acquire unique fingerprints from each container. The ultrasonic amplitude response of a series of chamfers machined in the inner part of the copper lid can be used as a unique signature readable from outside the canister. In addition, canisters can be authenticated by investigating the welding area between the lid and the canister itself. The robustness of this approach is guaranteed by the angular matching between the identification and authentication fingerprints to produce a third unique fingerprint, more reliable than the other two. Several experimental tests are performed to validate the approach and optimize the design of a device for the acquisition of ultrasonic fingerprints. A potential implementation of this device within the Swedish disposal process is also studied. The acquisition of ultrasonic references could be carried out after canisters' final machining at the encapsulation plant and the process could be completely automated. The reduced cost of realization and its ease of use are the main advantages of the method. However, the machining of chamfers on copper lids requires the introduction of further steps in the manufacturing process of containers.

Keywords: ultrasound, identification, authentication, copper canisters.

1. Introduction

The final disposal of spent nuclear fuel in geological repositories introduces the need to revise safeguards approaches for a safe and secure handling of the fuel [1]. In 2011 the Swedish Nuclear Fuel and Waste Management Co. (SKB) submitted an application for the construction of a long-term geological repository in Forsmark (Sweden). The SKB method for final disposal is based on a multi-barrier system: copper canisters with iron inserts are used to host fuel assemblies; the bentonite clay is then used to cover canisters once deposited in tunnels and the bedrock isolates canisters from human-beings and the environment for thousands of years. The spent nuclear fuel coming from nuclear power plants will be stored for a period in pools at the Central Interim Storage Facility (Clab) in Oskarshamn. Then fuel assemblies will be dried and inserted in copper canisters with iron inserts at the encapsulation plant (that will be built next to the Clab). Canisters are big cylinders, about 5 m high and 1 m in diameter with a lid and a tube welded together by Friction Stir Welding (FSW). After the encapsulation of the fuel, copper canisters will be placed in transport casks and temporarily stored before being shipped to the final repository in Forsmark (Figure 1). At this facility, canisters will be reloaded to a deposition machine in the underground central area and then the canisters will be deposited in tunnels, later backfilled and sealed with a concrete plug. A total amount of 6,000 canisters will be deposited underground with an average of one canister per day, over roughly 40 years [2]. The International Atomic Energy Agency (IAEA) model integrated safeguards approach for geological repositories foresee that Containment and Surveillance (C/S) measures should be applied to guarantee Continuity of Knowledge (CoK) of spent nuclear fuel during storage and transport of copper canisters [3].

Figure 1. The spent fuel transfers in the Swedish system for final disposal of spent nuclear fuel.

Since in Sweden the encapsulation plant and the geological repository are not located on the same site safeguards approaches defined by the IAEA should be adapted to ensure CoK throughout the handling chain of the copper canisters. Surveillance systems could be used inside facilities to monitor the flow of spent nuclear fuel, while seals applied on transport casks could guarantee the identity of canisters during the transport from the encapsulation plant to the geological repository. However, in case of failure of one of the two measures, the identification of copper canisters by a unique tag could be adopted to recover CoK. Tagging devices should give a unique identifier to each canister (identification fingerprint) and return evidence of falsification attempts (authentication fingerprint). External engraving of canisters should be avoided because it could trigger a corrosion process. Moreover, according to geometrical features, the minimum copper thickness to assure the stability of canisters' structure is 50 mm. The majority of conventional tagging devices used to identify uniquely nuclear items are analysed in [4] to see to what extent they could be adopted in the case of copper canisters. As a result, even if the identification of canisters could be realized with different methods, such as Reflective Particle Tags (RPT), ultrasonic methods or Tungsten-based Identifiers, the verification of authenticity is complex since it should be accomplished by techniques which analyse intrinsic properties of a canister. The ultrasonic method seems to be the only one able to identify and authenticate copper canisters. A description of this method for copper canisters identification and authentication is reported in the paper, discussing advantages and disadvantages for a potential implementation in the Swedish system for final disposal.

2. The ultrasonic method

Ultrasound constitutes pressure-waves which can propagate across a specimen and are reflected whenever a discontinuity is encountered, i.e. a boundary between means of different acoustic impedances. At the interface between air and copper, for example, since the acoustic impedance mismatch is large, a couplant, such as water, is necessary to allow the transmission of the ultrasonic beam in copper. Canisters for spent nuclear fuel are made of copper to provide safety during handling and emplacement of the fuel in the repository and also to ensure isolation from the biosphere for thousands of years. Ultrasonic non-destructive testing is used to check the integrity of copper canisters and also the quality of the weld between lid and tube after the encapsulation of the fuel. However, the investigation of canisters by ultrasound could also be adopted for the acquisition of a unique identifier from each container. Ultrasonic techniques for reading bolt seals with artificial cavities applied on nuclear casks deposited in underwater and dry storages have been used in the nuclear field for twenty years. In the case of copper canisters for spent nuclear fuel, the ultrasonic method for the identification and authentication of each container is based on the acquisition of two fingerprints by ultrasound.

The identification signature is created by machining a series of chamfers machined in the inner surface of the canister's lid where the copper thickness is greater than 50 mm. Chamfers are arranged around the lid circumference creating a unique code for each canister, readable by rotating a transducer as placed in Figure 2. The ultrasonic probe is kept inclined, in order to maintain the probe perpendicular to chamfer surfaces to obtain reflections according to Snell's law. Whenever a chamfer is detected, an echo is received by the probe and values of amplitude and time of flight are collected. By a 360° rotation of the probe around the lid circumference, a unique code, strictly related to chamfers' position, can be acquired. In particular, the ultrasonic amplitude response of the chamfers represents an identification fingerprint for each copper canister. Acquiring this signature can be accomplished by immersion testing with water and the probe could be rotated automatically with a motor remotely controlled.

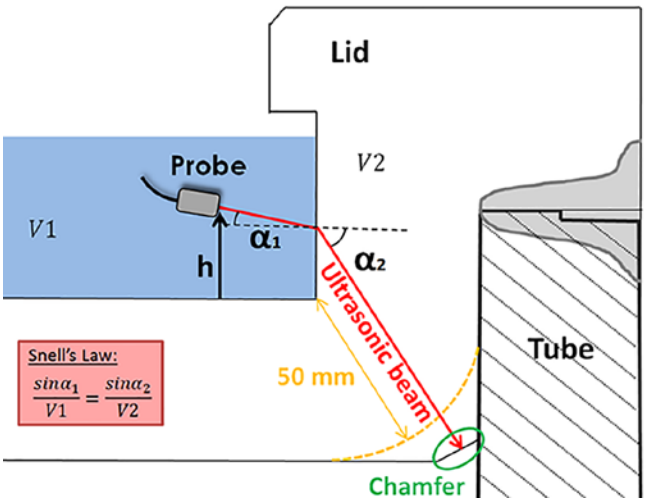

Figure 2: Ultrasonic investigation of chamfer (circled in green) machined in the inner part of the copper canisters' lid. V1 and V2 are the velocities of sound in water and copper respectively while α_1 and α_2 are the angles of incidence and transmission of the ultrasonic beam (red arrow).

The geometry of chamfers should be defined, on the one hand, to maximize the signal-to-noise ratio of the ultrasonic investigation and, on the other, to not affect the copper canisters' geometry too much. For this purpose, simulations and experimental tests on a laboratory mock-up have been carried out. As reported in [5] the acquisition of chamfers' amplitude response was carried out on a ¼ scaled version of the copper lid with chamfers arranged around the circumference. The immersion test with an inclined probe, rotating 360° around the mock-up, confirmed the possibility of acquisition of an ultrasonic amplitude echo, whose variation is correlated to chamfers position.

Afterwards, results of simulations with CIVA software [6], revealed that the best compromise to meet all the requirements is a 10 mm wide chamfer with an inclination of 55°. This solution involves removing only 4.3 g of copper out of the full-sized 708 kg lid. Moreover, this chamfer length will ensure a good signal-to-noise ratio in the ultrasonic inspection also when varying the probe inclination, and in case of temperature variations in the water used for the immersion test. Temperature changes, in fact, affect the velocity of sound in medium and as a result, the ultrasonic investigation itself. While in copper these variations are negligible, in water the velocity of sound fluctuates from 1403 m/s at 0°C up to a maximum of 1555 m/s at 74°C with a percent variation of about 11% [7]. According to the Swedish design criteria, the maximum temperature of the canisters' outer surface is around 100°C. The CIVA simulations show that 10 mm wide chamfers can be clearly distinguished from the rest of the lid even in varying temperatures as shown in Figure 3. The echo amplitude of the chamfer 10 mm wide (green curve) is higher than without chamfers (blue curve). Therefore, in a range of temperatures between 5°C and 100°C, a chamfer 10 mm wide can be detected with a good margin: as shown in Figure 3 the amplitude acceptance threshold at 0.04 (red line) is 10 times bigger than the maximum amplitude without chamfers. In case of inspection with water temperatures below 7°C, chamfers can be discriminated as well, but the signal-to-noise ratio is lower than in the case of inspections with higher water temperature.

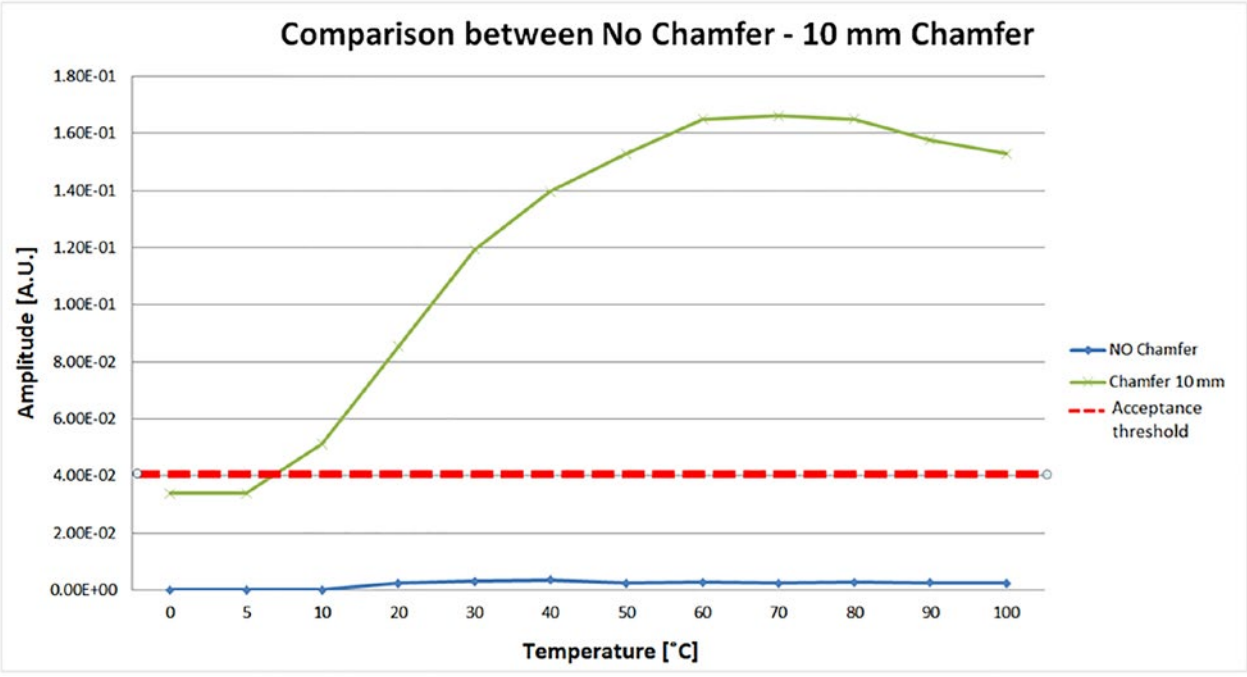

Figure 3: Simulation of the ultrasonic amplitude response acquired by the investigation of lid with (green curve) and without (blue curve) a chamfer 10 mm wide, considering a temperature variation from 0°C to 100°C. The red curve represents the acceptance threshold above which a chamfer 10 mm wide is well discriminated from the case with no chamfer.

The angular extension of chamfers is another important parameter which can impact on canister's geometry. The unique reflection realized by chamfers arranged around the lid circumference should be optimized in order to reduce the amount of copper to be removed. As a consequence, the early idea of a binary code with at least 13 chamfers and a reference for the identification of about 6,000 containers has been replaced with another coding. The new solution (Figure 4) splits the lid circumference into four imaginary sections 27° wide representing thousands, hundreds, tens and units. Each division is in turn divided into nine slots, which may or may not host a chamfer inclined 55°, 10 mm wide and with an angular extension of 3°. In this way, depending on which slot of each section is occupied by the chamfer, it is possible to give a unique ID number to a canister with only four chamfers plus the reference.

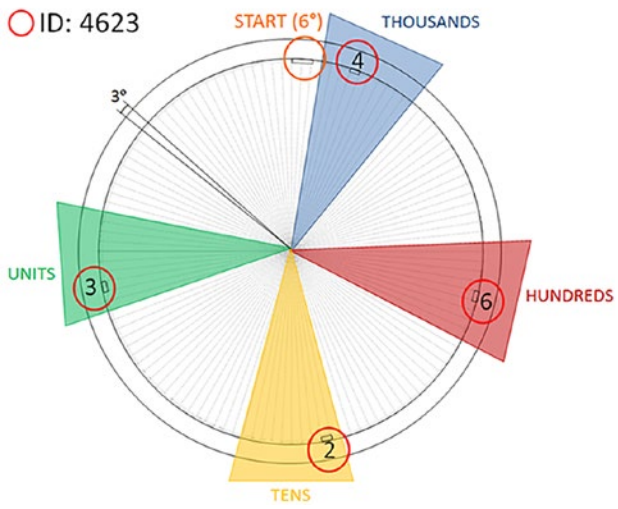

Figure 4: Proposed coding for chamfers to uniquely identify a copper canister (ID 4623).

To conclude, the identification of canisters is could be realized by chamfers machined on the lids inner surface, readable from outside by an ultrasonic probe. Nevertheless, the code created by chamfers could be duplicated and then another solution should be implemented to verify attempts of falsification. For this purpose, taking advantage of the ultrasonic transducer already implemented in the identification concept, a method to verify the canister's authenticity is developed.

In contrast to the identification fingerprint, the authentication signature is an intrinsic property of each copper canister. After the fuel assemblies have been encapsulated, the copper lid is welded onto the tube by Friction Stir Welding (FSW). A rotating tool penetrates between the two surfaces, heats the material and creates a joint [8]. According to the geometry design, two faces of the lid lean against the tube: at the end of the welding process, only one of them is welded to the tube and the other represents a gap between the lid and the tube. This discontinuity can be detected by an ultrasonic transducer as placed in Figure 5.

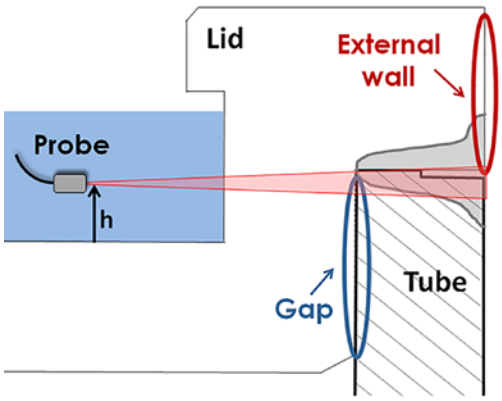

Figure 5: Ultrasonic investigation of the welding area between lid and tube of a copper canister. The probe is kept at a fixed height "h".

The ultrasonic amplitude response changes according to the variations of the gap height all around the lid circumference. Preliminary studies on copper flanges, i.e. slices of a copper lid already welded onto the tube, demonstrates the feasibility of the method: ultrasonic echoes from the internal gap and external wall surfaces have been acquired with a good signal-to-noise ratio using a 10 MHz immersion transducer [9]. Afterwards, experimental tests are carried out on full scale welded lids at the SKB's Canister Laboratory in Oskarshamn (Sweden). For this purpose, an ad hoc acquisition system prototype was designed. The reader, i.e. the device used to read authentication fingerprints, is made up by three steel arms, a motor devoted to the probe movement and a rotating bar to keep the transducer perpendicular to surfaces to be investigated. Signals are transmitted and received by an electronic module which is connected to another board for the control of the motor and power supply. Results of investigations are then processed and displayed on a computer [10]. The set-up of measurements for the investigation of welded copper lid is shown in Figure 6. Several measurements have been carried out, changing the position of the reader above the lid and the probe height in order to verify the repeatability of measurements and inspect a wide area of the welded region. Two time windows are used to acquire the maximum amplitude echo between the internal gap and the external wall.

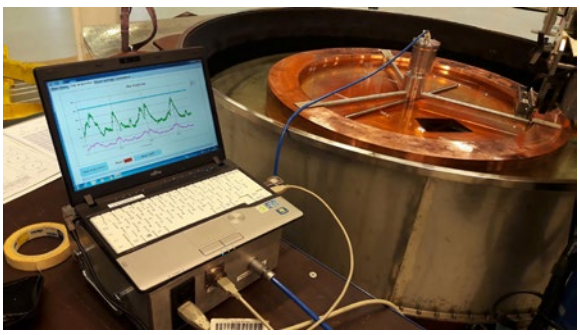

Figure 6: Set-up of measurements on copper samples: the reader for the scanning of the welding area is centred on the lid and signals are transmitted/received to/from the ultrasonic transducer by a control box connected to a computer for the processing and display of acquisitions.

After a complete rotation of the probe, the ultrasonic amplitude responses are collected and analysed. In Figure 7 is a display of the ultrasonic amplitude response of the internal gap (in blue) and the external wall (in red) on rotation angle of the probe. The two curves are quite fluctuating and present interesting peculiarities which can be unique to each container. However, the uniqueness of the welding area should be verified undertaking a statistical analysis of a consistent number of samples.

The ultrasonic method is based on the acquisition of ultrasonic-amplitude responses of chamfers (identification) and welded regions (authentication). While the first can discriminate each canister from another, the second helps to verify the authenticity of each canister. However, duplication of both fingerprints could make it difficult to ascertain the authenticity of a given canister. Therefore, we introduce a third fingerprint to our method to increase the reliability. The new fingerprint is simply realized connecting the intersection points between identification and authentication fingerprints. In this way, as shown in Figure 8, if the angular matching between the two fingerprints (blue line for the identification and yellow line for the authentication) is not the same as in the reference, it is possible to detect anomalies and demonstrate potential counterfeit canisters. A patent has been filed for both the identification and authentication approaches [11].

3. Potential implementation in the Swedish system

The adoption of the ultrasonic system could be extremely important in the case of failures of the other two main C/S measures: the monitoring devices and seals applied on transport casks. The encapsulation plant and the geological repository could be considered as black boxes where additional C/S measures are not necessary. However, during transport of copper canisters between the two sites, the use of dual C/S measures is recommended. Therefore, the implementation of an additional system to identify and uniquely authenticate each canister could be considered as a useful way to recover CoK in case of losses and not as a routine measure. The introduction of a unique identifier should also be combined with other techniques to verify the integrity of the canister and the fuel inside. This section describes how the ultrasonic method could be included within the Swedish system for final disposal.

The identification and authentication fingerprints, to be used as references, could be acquired at the encapsulation plant, stored in a database and then verified with other measured fingerprints, only in case of necessity. In general, performing verification measurements to assess the fuel and the canisters' integrity at the geological repository is not desirable, but since this should not be a periodic procedure, it could be useful to recover CoK using ultrasonic methods in case of the failure of other C/S measures. Ultrasonic fingerprints could be acquired at the encapsulation plant and a reference could be stored for each container. At the geological repository, these fingerprints could be verified in case of necessity and acquired responses could then be compared with references. At the encapsulation plant, after the encapsulation of the fuel, canisters are welded and ultrasonic and radiographic tests are then performed on each container to verify the quality of the weld. At this stage, reference fingerprints could be acquired. In particular, an ad hoc system could be developed to acquire automatically a reference signature from each

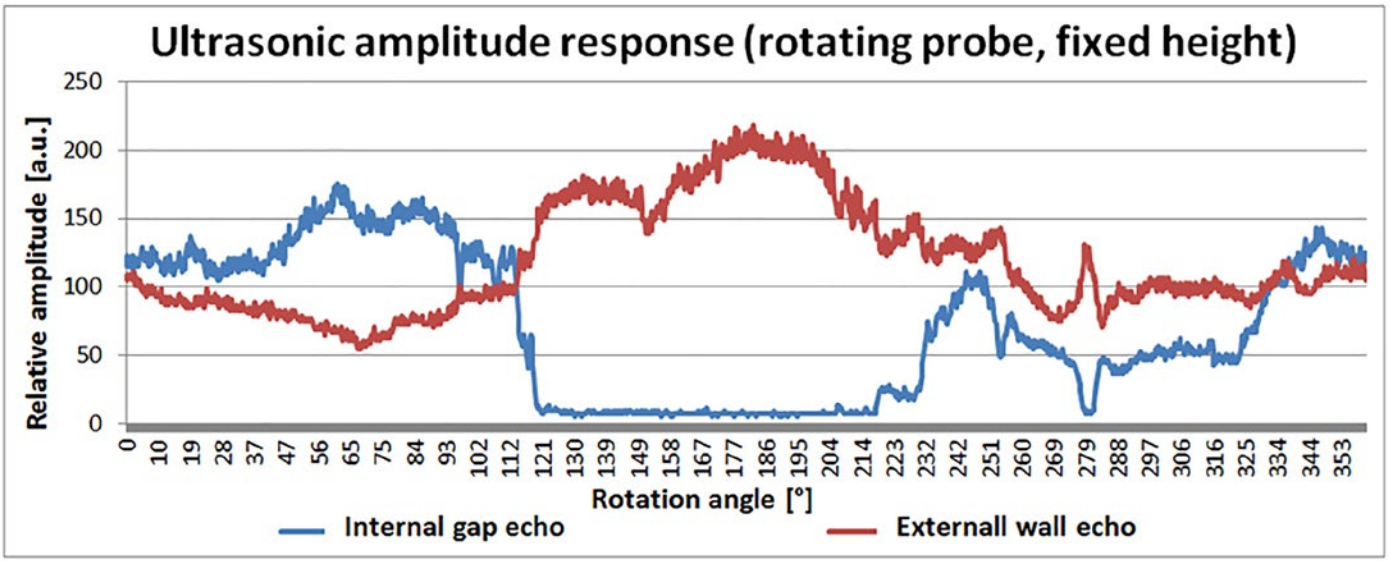

Figure 7: Ultrasonic amplitude response acquired rotating the transducer around the copper sample circumference with fixed height h. The red line is the amplitude response of the external wall while the blue line is the amplitude response of the internal gap.

canister. Ultrasonic measurements could be performed in the same room as the radiographic inspection of welds. A section view of the possible ultrasonic reader placed above a canister is shown in Figure 9. The device can be seen as an optimized version of prototypes already developed for laboratory tests. This new system includes a cylindrical box which hosts a tank for water, plus a motor and a rotating bar which supports two transducers (highlighted in yellow in Figure 9). One transducer is kept perpendicular to the welding area to acquire the authentication fingerprint and the other transducer is inclined according to Snell's law to receive echoes and furthermore to generate the identification code produced by the chamfers. The speed of the motor can be adjusted to optimize the acquisition of

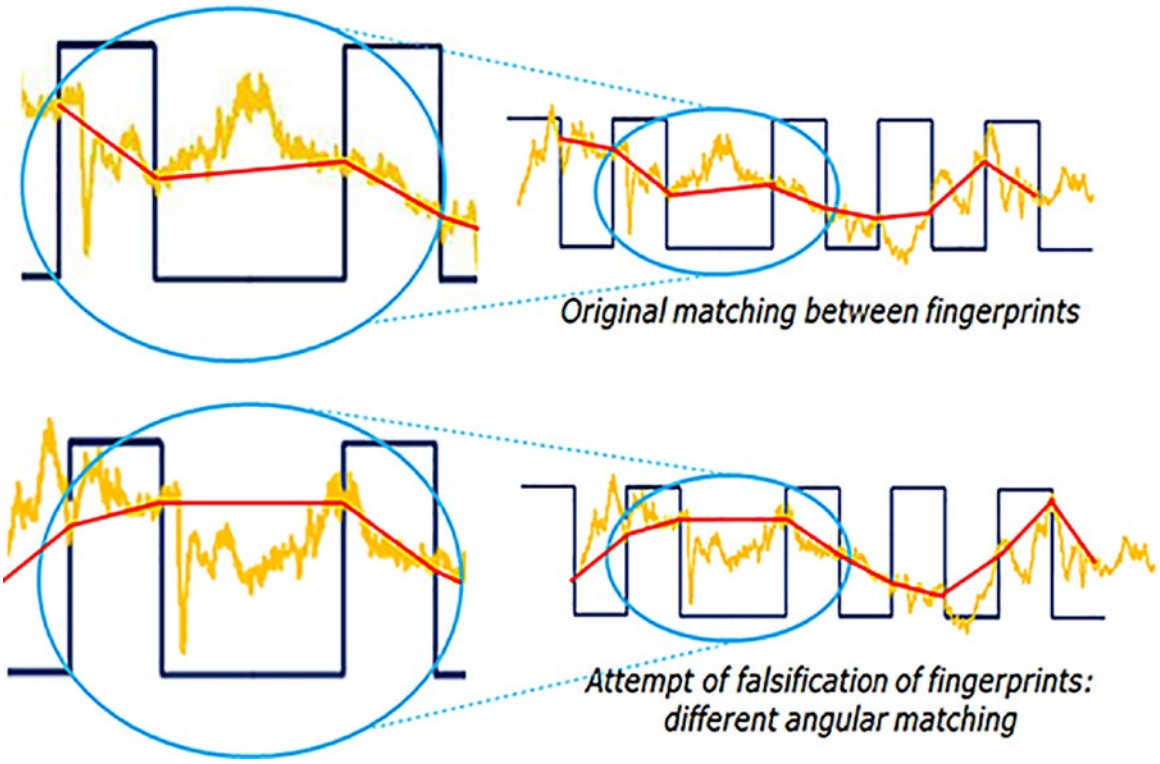

Figure 8: Comparison between a real fingerprint and a copy: the differences in angular matching between the identification (blue curve) and authentication (yellow curve) fingerprints can be detected analysing the trend of the third fingerprint (in red).

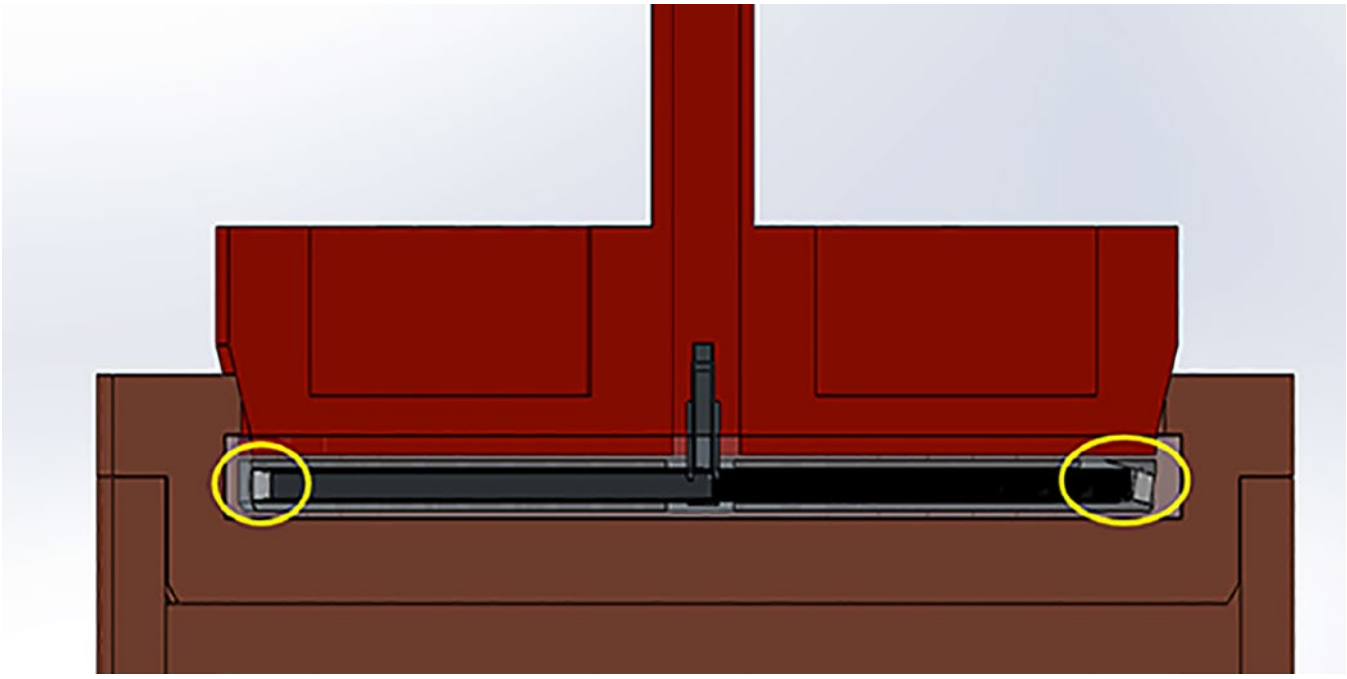

Figure 9: Section view of a CAD design of the ultrasonic reader device placed above a canister. Two probes (highlighted in yellow) rotate around the lid circumference to acquire the identification and the authentication fingerprints.

signals and different inspections can be performed changing the transducer height for the collection of a larger amount of data.

All ultrasonic measurements could be accomplished without the involvement of an operator: the reader system could be put in place by a crane or robotic arm and automatically centred on the lid (Figure 10). Once in place, water can be poured on the external concave of the lid and the ultrasonic immersion testing could be launched. After a complete rotation of both probes, the two curves are registered, stored in a memory card and sent wirelessly to a control station. The processing of signals for the definition of the third fingerprint can be done at the post-processing of data. At the end of the inspection, water will be pumped away from the lid.

All the electronics useful for the control of the motor and the transmission/reception of signals could be developed in an embedded version to fit inside a cabinet which could be placed in the same room as the measurements set-up (far from radiation emitted by the spent fuel inside the canister). All the reading processes could be monitored by surveillance devices and a complete rotation of transducers could be completed in a few minutes. Differently from other identification methods, the ultrasonic method is easy to implement and use, since it works automatically without the need of operators. In addition the cost of signatures' manufacturing is practically included in the canisters production costs. However, the realization of unique configurations of chamfers around copper lids involves the introduction of an additional step within the manufacturing process of canisters.

In the case of verification of fingerprints at the geological repository, a portable version of the same reader could be developed to make an easy verification whenever it is required.

A State might require that canisters be retrieved from a repository as a safety measure [12], as is the case for Sweden. Safeguards approaches have not been pre-determined for any retrieval scenarios. However, having a unique reference for each container could be useful to keep the CoK in case of retrieval, based on the hypothesis that the identification and authentication fingerprints would not be altered at that time, and there is knowledge available to use the ultrasonic methods for the identification of the canisters.

4. Conclusions

The final disposal of spent nuclear fuel introduces new challenges in the field of nuclear safeguards. The transport of copper canisters with spent nuclear fuel from the encapsulation plant to the final repository, as planned in Sweden, requires the implementation of supplementary C/S measures, in addition to dual surveillance and sealing systems, to be used in case of CoK losses. The ultrasonic method for the identification and authentication of copper canister is a potential way to help the recovering of CoK if necessary. However, canister identification should be combined with other techniques to verify the fuel integrity in order to recover the CoK. This method is based on the ultrasonic acquisition of two fingerprints. The ultrasonic amplitude response of a series of chamfers machined around the lid's inner surface could be used to generate an identification fingerprint. In addition, the ultrasonic amplitude response of the welding area between the copper lid and the canister can be used as an intrinsic fingerprint which authenticates each container since the ultrasonic amplitude response is only related to material properties and the welding process. Experimental tests were performed to validate both concepts and our results confirmed expectations. We recommend that future tests be performed on a full-scale copper lid with chamfers already

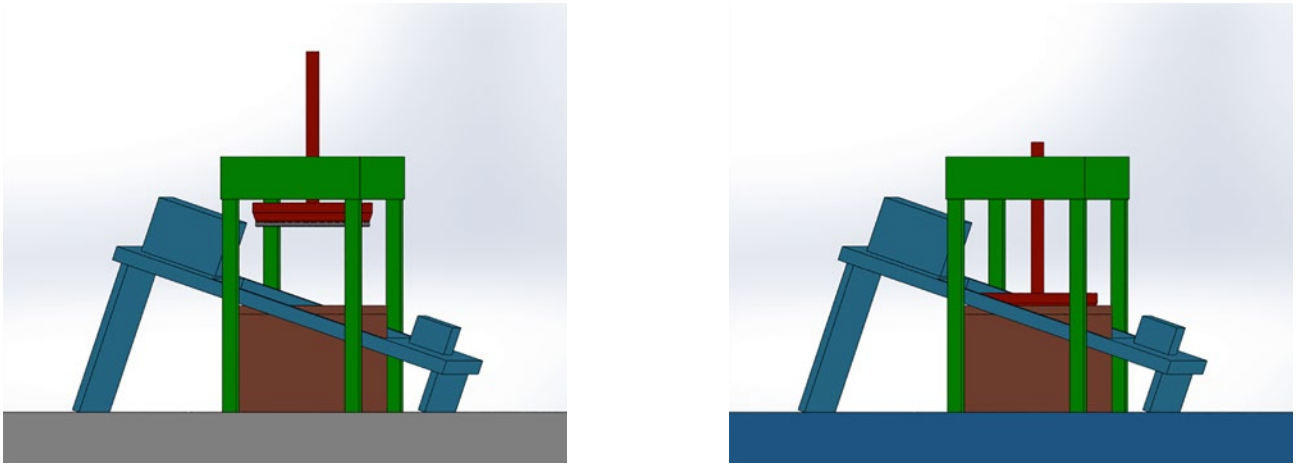

Figure 10: The ultrasonic acquisition of identification and authentication fingerprints could be performed in correspondence of the radiographic station for weld verification (in blue). On the left, the ultrasonic reader (in red) is lifted above the copper canister. On the right, a crane (in green) arranges the device on the canister.

welded to a canister tube in order to validate the third fingerprint described in Section 3. In fact, the angular matching between the identification and authentication signals could realize a third unique signature, increasing the robustness and reliability of the whole method. The design of an ultrasonic reader has been presented and its use has been optimized to avoid the involvement of an operator during the acquisition of fingerprints. The proposed version could be adopted within the encapsulation plant but a second version could be developed for the geological repository, by adapting of the one designed for the encapsulation plant.

5. Acknowledgements

This research has been accomplished by the Seals and Identification Lab (SILab) of the Joint Research Centre of the European Commission in Ispra in collaboration with the Department of Information engineering of the University of Florence. We would like to thank our colleagues from SKB for the copper samples provided to us for tests and all the expertise shared with us.

6. References

[1] af Ekenstam G.; Hildingsson L.; Fagerholm R.; Andersson C.; *Elements of a Swedish Safeguards Policy for a Spent Fuel Disposal System;* ESARDA Bulletin 54; June 2018; pp.36-41.

[2] Hildingsson L.; Andersson C.; Fagerholm R.; *Safeguards Aspects Regarding a Geological Repository in Sweden*; IAEA Safeguards Symposium, Paper CN-220-166; Swedish Radiation Safety Authority: Stockholm; Sweden; 2014.

[3] International Atomic Energy Agency: IAEA; *Model Integrated Safeguards Approach for a Spent Fuel Encapsulation Plant*; SG-PR-1305; ver. 1; 10 June 2010.

[4] Clementi C.; Littmann F.; Capineri L.; *Comparison of Tagging Technologies for Safeguards of Copper Canisters for Nuclear Spent Fuel*; Sensors 2018 18(4) 929; March 2018. Available online (accessed on Sept 28 2018): https://doi.org/10.3390/s18040929.

[5] Clementi C.; Littmann F.; Capineri L.; Andersson C.; Ronneteg U.; *Ultrasonic Identification Methods of Copper Canisters for Final Geological Repository*; ESARDA Bull. N.54; 2017, pp. 75–81.

[6] Ultrasonic Testing with Civa- Extende. Available online (accessed on April 15 2019): http://www.extende.com/ultrasonic-testing-with-civa.

[7] Engineering ToolBox, *Speed of Sound in Water*, 2004. Available online (accessed on Nov 10, 2017): https://www.engineeringtoolbox.com/sound-speed-water-d_598.html.

[8] Stepinski T.; Engholm M.; Olofsson T.; *Inspection of copper canisters for spent nuclear fuel by means of ultrasound Copper characterization*, *FSW monitoring with acoustic emission and ultrasonic imagin*; Uppsala University; Signals and Systems Department of Technical Sciences; Sweden; August 2009.

[9] Clementi C.; Capineri L.; Littmann F.; *Innovative Method to Authenticate Copper Canisters Used for Spent Nuclear Fuel Based on the Ultrasonic Investigation of the Friction Stir Weld*; IEEE Access 2017; Vol. 5; doi:10.1109/ACCESS.2017.2694878.

[10] Clementi C Littmann F.; Capineri L.; *Ultrasonic Investigation of the Welding Area of Copper Canisters for Spent Nuclear Fuel*; ESARDA Bull. N.56; 2018; pp. 19-27.

[11] Littmann F.; *Ultrasonic identification and authentication of containers for hazardous materials*; EP 16166465; April 21; 2016.

[12] Mongello R; Finch R. J.; Baldwin G.; *Safeguards Approaches for Geological Repositories: Status and Gap Analysis*. Available online (accessed on Feb 02 2019): https://www.researchgate.net/publication/280655578_Safeguards_Approaches_for_Geological_Repositories_Status_and_Gap_Analysis.

Highlights of the Quad Multilateral Nuclear Arms Control Research Initiative LETTERPRESS Simulation

Jacob Benz[1], Keir Allen[2], Goran af Ekenstam[3], Styrkaar Hutsveit[4]

[1] Pacific Northwest National Laboratory (PNNL), Richland, WA, USA
[2] UK Atomic Weapons Establishment (AWE), Aldermaston, United Kingdom
[3] Swedish Radiation Safety Authority, Stockholm, Sweden
[4] Norwegian Radiation and Nuclear Safety Authority, Oslo, Norway
Email: Jacob.benz@pnnl.gov, Keir.allen@awe.co.uk; Goran.af.ekenstam@ssm.se, Styrkaar.hustveit@nrpa.no

Abstract

The US, UK, Sweden and Norway have formed the Quad Nuclear Verification Partnership and have been working together as the 'Quad' to ensure non-nuclear weapon states (NNWS) and nuclear weapon states (NWS) collaborate to overcome the challenge of nuclear arms control verification. The Quad aims to complement and inform the work of other multinational initiatives such as the International Partnership for Nuclear Disarmament Verification (IPNDV).

The initial engagement of the Quad was the development and execution of a role-playing, in-field verification simulation, named LETTERPRESS. A benefit of role-playing events is the capacity they have to allow researchers to engage critically with a challenge from multiple perspectives. This paper will introduce LETTERPRESS and the process the Quad followed to develop and execute the multilateral simulation. The paper will highlight the in-play objectives of the verification regime, the site hosting the on-site inspection, and the verification technologies and their roles with respect to the objectives. The paper will include lessons learned from LETTERPRESS and their contribution to a successful monitoring result. The paper will conclude by highlighting the in-play success of a multilateral verification body and the ability of both NNWS and NWS to contribute to the verification process within LETTERPRESS.

Keywords: Quad, LETTERPRESS, multilateral, arms control

1. Introduction to the Quad

The Quad is a multilateral nuclear disarmament verification partnership bringing together representatives from two non-nuclear-weapon states (NNWS), Norway and Sweden, and two nuclear weapon states (NWS), the United States and United Kingdom. The Quad builds upon previous experiences, such as the UK-Norway Initiative [1] and US-UK arms control exercises [2], to collaborate and explore technical and policy solutions to help solve verification and monitoring challenges related to nuclear disarmament. The Quad also aims to complement and inform the work of other multinational initiatives such as the International Partnership for Nuclear Disarmament Verification (IPNDV) [3].

One objective of the Quad is to enhance and extend previous work by the Quad partners and investigate how NWS) and NWS may participate together to demonstrate how multilateral nuclear disarmament verification could work and be implemented in the real world. This objective directly supports Nuclear Nonproliferation Treaty (NPT) Article VI, ***Each of the Parties*** *to the Treaty undertakes to pursue negotiations in good faith on effective measures relating to cessation of the nuclear arms race at an early date and to nuclear disarmament, and on a treaty on general and complete disarmament* ***under strict and effective international control*** [4]. The key section of Article VI impacted by the Quad engagement is highlighted in bold. Complementarily, the engagement also impacts Article I and Article II of the NPT to provide assurance that disarmament activities can include effective international control without revealing or proliferating sensitive weapon design information.

2. Introduction to the LETTERPRESS Simulation

2.1 LETTERPRESS Scope and Objectives

LETTERPRESS was the name of the simulation executed in October 2017 at Royal Airforce (RAF) base Honington in the UK, and represented the first activity undertaken by the Quad. It included approximately 50 representatives from all four countries who acted as planners, i.e. for logistics, simulation execution, support, and simulation evaluation, and players, i.e. host and inspection team members. At a high-level, the exercise examined one on-site inspection activity, as part of a broader treaty regime, at an interim storage facility. The fictitious site where the interim storage facility was located was called Notinghon, and is represented in Figure 1. The in-play objective was to confirm the correctness and completeness of the host declaration, and establish chain of custody (CoC) over treaty accountable items (TAI) destined for dismantlement. There were confirmation measurements to confirm the authenticity of the declared TAI, absence measurements to confirm the absence of undeclared TAIs at declared locations, and CoC measures, i.e. surveillance, tamper indicating devices and enclosures (TIDs/TIEs), and unique identifiers (UIDs) to maintain the integrity of equipment, facilities, and TAIs.

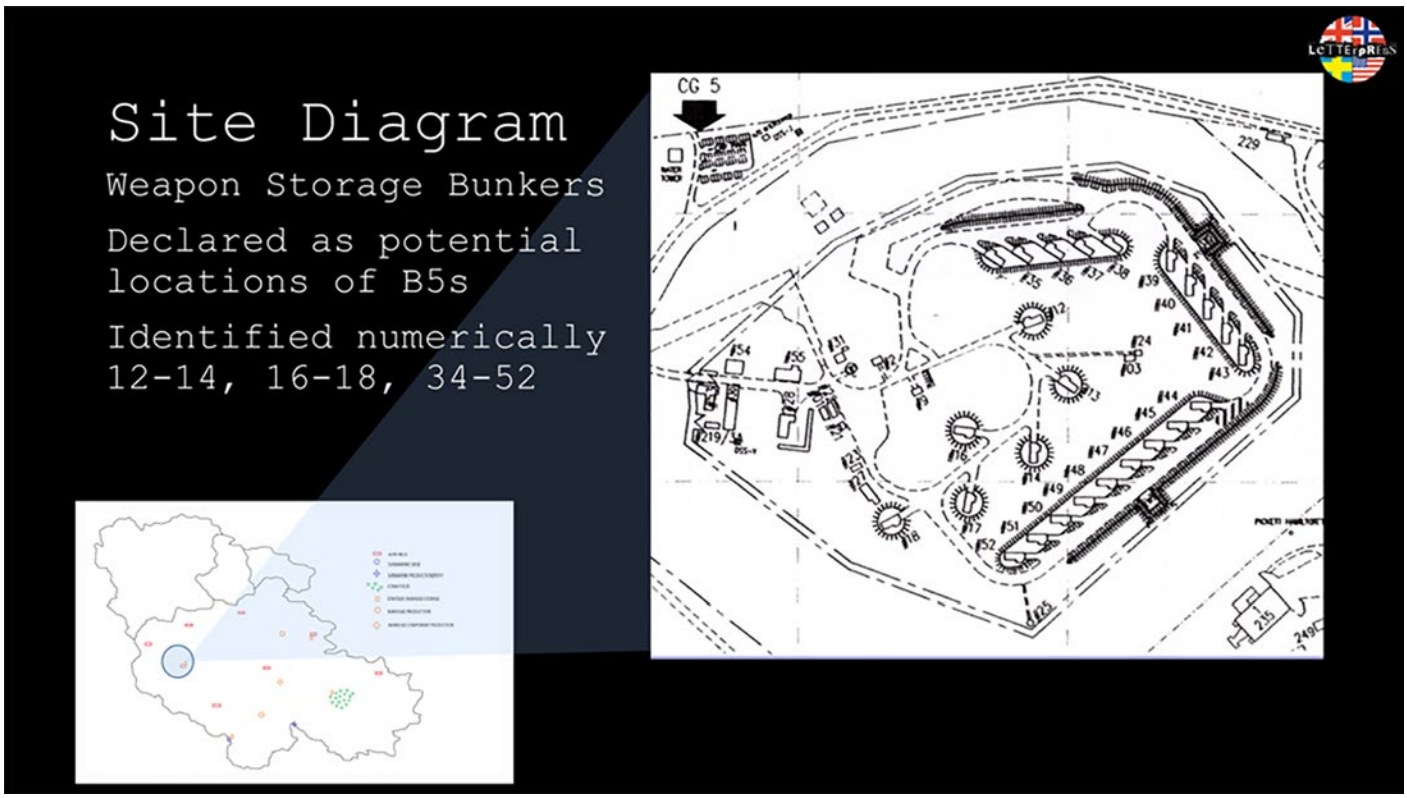

Figure 1: 'Notinghon', the interim storage facility that featured in LETTERPRESS, was just one declared site in the fictitious state. The site contained multiple locations and facilities.

Out of play, the research objectives of LETTERPRESS were to evaluate technical options for collecting and analyzing treaty relevant information and data, and to explore the minimum information necessary for the inspectors to achieve their inspection objectives. Additionally, LETTERPRESS included learning objectives to immerse a diverse set of technical experts from the four countries into a realistic monitoring and verification scenario. Together, the participants would gain a greater appreciation for the challenges present in verification of nuclear arms control/reduction treaties, and to gain experience and knowledge to continue to work together in the future to address these challenges.

3. LETTERPRESS Treaty and Verification Regime

In order to achieve the stated learning objectives, it was important to develop a realistic scenario. Toward that end, the Quad partners pulled from previous and current treaties and agreements, specifically New START, and leveraged the expertise of the partners in arms control, nonproliferation and international safeguards. The following formed the foundation of the verification regime.

3.1 LETTERPRESS Background and High-Level Declarations

Two NWS agreed to a significant reduction in their respective stockpiles. As part of the significant reduction in nuclear weapons, the two countries agreed to include the two neighboring NNWS to be part of the inspectorate tasked with confirming the technical aspects of the monitoring regime. The 'B5', as called out in the scenario as the Treaty Accountable Item and referred to throughout this paper and shown in Figure 2, was represented by a WE177 weapon case. The WE177 was a historical UK gravity bomb. As part of the agreement to this treaty, the following high-level declarations were made:

a) All B5s will be removed from the active stockpile over the lifetime of the treaty. The operationally deployed B5s will be reduced over time through the dismantlement process.
b) B5s selected to enter the dismantlement process will be declared and transported from their respective operational bases to the interim storage site where they will be stored until ready for dismantlement at the just-in-time dismantlement facility.
c) B5s remaining operationally deployed may require refurbishment over the lifetime of the treaty. These items will be transported from their respective operational bases to the interim storage site where they will be stored until ready for refurbishment.

New START is a current nuclear arms control treaty between the US and Russia which limits each party's strategic delivery vehicles and warheads with an inspection protocol detailing the content, structure, and requirements for providing notifications and declarations of treaty

Figure 2: A B5 bomb sits outside its container during the LETTERPRESS simulation. Inspectors (in white) and host personnel discuss the next step in the verification procedure.

accountable items to each treaty partner [5]. Leveraging New START type notifications and declarations, a number of assumptions were made for LETTERPRESS with respect to the protocol and agreement. These included:

a) Per the agreed protocol, there is an agreed number of inspections allowed per year at the interim storage site and the dismantlement facility.
b) The host country will provide post-departure and post-arrival notifications of inter-site movement to all treaty partners no later than five days after the movement is complete.
c) The host country will notify the treaty partners of its intent to send a batch of treaty accountable items, previously declared for dismantlement, from interim storage to the dismantlement facility.
d) The host country will provide only post-departure and post-arrival notifications of movement for B5s requiring refurbishment.
e) The inspecting party may request to initiate an on-site inspection after any number of notifications of movement, or an intent to send items to the dismantlement facility have been provided.

This last assumption served as the impetus for the LETTERPRESS exercise.

At a high-level, the verification activities simulated in LETTERPRESS were the following:

1. Upon arrival on-site, the inspectors confirmed CoC over a storage bunker serving as treaty monitored storage for all B5s declared for dismantlement and which were initialized into the monitoring regime. They also confirmed CoC over a bunker where they performed agreed measurements and stored equipment.
2. Upon establishing CoC over the storage bunkers, the inspectors declared that they were ready to accept and initialize the B5(s) into the regime.
3. A confirmation measurement was performed on each declared B5 (*to address the 'correctness' element of the protocol and confirm the declared treaty accountable item attributes*).

- An agreed UID was initialized and confirmed for each B5.
- An agreed confirmation measurement was performed on each B5. It was radiation-based and confirmed an agreed set of attributes and compared against a trusted template. The trusted template was generated by performing a reference measurement on an active stockpile B5 declared on-site. Subsequent measurements were compared against that reference template.

4. As agreed in the protocol, the inspectors exercised their right to perform monitoring of items and activities at other declared locations at the site. Therefore, the inspectors requested to inspect a random storage bunker declared as empty.
5. The inspectors performed an absence measurement on the container(s) to confirm lack of a radiation (neutron) signature and noted visual observations (*to address the 'completeness' of the element of the protocol*).
6. Inspectors performed the following CoC measures on the selected B5(s) transported to the dismantlement facility.
   - The inspectors confirmed the UID of each B5 selected for transport to the dismantlement facility.
   - The inspectors installed agreed TIDs to secure the B5 and container during transport.
7. Upon arrival at the dismantlement facility, the inspectors confirmed the authenticity and integrity of the CoC measures and performed a reconfirmation measurement.
   - The host presented each B5 which was transported from the interim storage site to the dismantlement facility.
   - Inspectors reconfirmed the UID of each B5.
   - Inspectors performed confirmation measurements for each B5. The agreed confirmation measurements were radiation-based and confirmed an agreed set of attributes and compare against a trusted template (*agreed to in the protocol*).

Once confirmation measurements were complete and successfully passed/matched, the item(s) were released by the inspectors and processed through dismantlement. *At this point, LETTERPRESS was complete.*

3.2 Rights, Responsibilities and Protocol

LETTERPRESS simulated an on-site inspection, where the role of the inspection team was to carry out an inspection at Notinghon to verify that the declaration made about the status and location of a number of B5 nuclear bombs was 'correct' and 'complete'. The role of the host team was to help facilitate the inspection team in their mission on site, while also ensuring the site security and national security are not compromised. Together these formed the overarching obligations of the inspection and host teams respectively and the biggest challenge in the development and execution of a robust verification regime: how can the inspection team collect sufficient data to confirm correctness and completeness while the host team protects sensitive, classified, or information otherwise outside of the treaty agreement?

Within LETTERPRESS, the completeness objective was simulated by allowing the inspection team to randomly select a facility bunker and perform an absence measurement to confirm the absence of a B5 to provide confidence that undeclared weapons are not stockpiled or deployed on-site. This activity is captured in Figure 3. This seemingly simple activity raised a number of questions and posed many challenges that, while not solved in LETTERPRESS, helped the Quad partners to better understand the techniques and challenges in this area.

A few simple examples of challenges are highlighted in the context of managed access, the host process to control site access and protect information. These include, defining the criteria for selecting inspection locations, how to lockdown the site, and the immediacy of allowing inspections versus protecting facility operations that cannot be stopped immediately. These examples reinforce the high-level LETTERPRESS objective to explore the minimum information necessary for the inspectors to achieve their inspection objectives. The project team worked hard to create a balance to simulate the realistic facility and on-site inspection constraints at a nuclear weapon facility and the flexibility to evaluate technologies and complete monitoring activities to explore what and how much information give inspectors adequate confidence towards their inspection objectives.

Within LETTERPRESS, the correctness objective was simulated through attribute and template measurements on declared B5s, both active stockpile and those declared for dismantlement. The confirmation technologies used included the UK-Norway Initiative Information Barrier (UKNI IB) with a high-purity germanium (HPGe) detector and the Trusted Radiation Identification System (TRIS). The use of TRIS to generate a trusted reference is shown in Figure 4. To facilitate these measurements, the treaty required the declaration of certain details about the basic design and stockpile characteristics of the B5. In the end, the declarations stated that all B5s contained plutonium below a threshold ratio of Pu-240 to Pu-239, and all B5s exhibited a very similar radiological profile. Together these declarations met the technical needs for the UKNI IB and TRIS respectively, and allowed the Quad to evaluate the correctness objective.

Figure 3: Radiation detection Equipment (RDE) is used to measure the local neutron count rate within a storage bunker that had been declared not to contain any B5 bombs as part of the absence verification procedure on a randomly selected location.

Figure 4: The Trusted Radiation Identification System (TRIS) is used to ensure the radiation profile of a B5 bomb is similar to a 'template' profile of another B5, collected earlier.

In the TRIS concept of operations, the initial trusted template would be generated on the first measured active stockpile B5 and use that template to compare all other B5s; if the template matched then it was declared a B5 and was initialized into the regime. From a policy perspective, this raised a number of interesting issues. First, it required the declaration of additional information about the B5 design and overall stockpile, e.g. the similarity of all B5s. If the profile of the B5s was not consistent throughout the stockpile, then the weapon owner could be forced to declare sub-populations upfront, or ensure the profile was sufficiently broad to cover all differences between B5s. The monitoring of how those sub-populations are used over time could impact operational security, while an overly broad profile could impact inspector confidence in the correctness of the initial declaration. Additionally, a template by itself does not directly relate to a weapon system. Since the spectrum from a template is never seen, it must initially be combined with an alternate method to gain confidence that the spectrum is truly from a declared weapon, e.g. using agreed attributes of a declared weapon. Lastly, the trusted template now needs to be protected and controlled throughout the timeframe of the treaty. This creates additional CoC requirements, e.g. key management and dual containment, from the inspector perspective and information and physical security requirements for the host.

In total, there are technical and policy challenges which exist in the use of TRIS, and templates in general. However, the huge benefit of templates is that, assuming a trusted template, the inspector can have high confidence in the authenticity of all other weapons declared to be of the same type, that match the reference template.

In the context of exploring the minimal amount of information necessary for inspectors to achieve their objectives, and in this case for the host to ensure protection of sensitive information, these discussions and the ultimate simulation of TRIS as a warhead confirmation tool proved valuable.

LETTERPRESS also focused on CoC, the process to maintain confidence in the integrity of inspection facilities, treaty accountable items, i.e. B5s, and inspection equipment. Issues that were explored included how to maintain confidence in the above between inspection visits, while on-site performing confirmation measurements and intra-site movements, and inter-site movements from Notinghon to the dismantlement facility. Technologies trialed during LETTERPRESS included an applied UID using the reflective particle tag (RPT) and an intrinsic UID produced using the eddy current tagging (ECT) system. In addition, the Chain of Custody Item Monitor (CoCIM) active loop seal and passive adhesive seals were applied to maintain control over monitored areas. Video cameras were notional.

Figure 5: An applied Unique Identifier (UID) Tag is applied to the container of the B5 to ensure the individual item can be accounted for and tracked throughout the treaty lifetime.

As an interesting note, during the planning process, there was significant discussion regarding the use of TRIS and the potential impact on the quality and quantity of information that must be included in the declaration. One of the early ideas was to utilize TRIS as a CoC tool. In this way, a template would be generated on a B5 declared for dismantlement prior to it leaving Notinghon. Upon arrival at the dismantlement facility, the template would be reconfirmed, and the inspectors would have confidence in the integrity of the B5 through transport and prior to it entering the dismantlement process. This process would be repeated for every B5 declared for dismantlement. With this concept of operations, there is no need to generate and store, for a long period of time, a trusted template because it was only valid through the transportation process. Additionally, there was no need to declare any information about the B5, e.g. the similarity of all B5 radiological profiles, to utilize TRIS because each B5 would have its own unique template. Discussions regarding the use of TRIS as either a CoC tool or warhead confirmation tool proved valuable to the team and highlighted a number of lessons learned surrounding the impact of technology on policy. As mentioned earlier, ultimately the decision was made to utilize TRIS as a warhead confirmation tool in LETTERPRESS.

In LETTERPRESS, the combination of declarations and CoC allowed the inspectors the opportunity to track declared items over time and between locations, and to know when monitored areas were accessed outside of inspector's presence. There were two techniques trialed to review data and ensure data security. The first was through physical security, and the second through cryptographic security. In the former, data from digital cameras used to confirm CoC seals was collected on secure digital memory cards (SD cards), stored in a tamper-indicating enclosure (TIE), and transported outside of the secure area under inspector visual observation and host control, as prescribed by applied host managed access. Upon receipt in the inspection station, the data was uploaded and manually reviewed. In the latter case, data was protected by cryptographic keys on the CoCIM, used to secure doors to monitored areas, and TRIS, as a confirmation tool. In each case, the integrity of the seal and template could be verified in-situ. The importance of data review for CoC and for maintaining overall confidence in the regime was made very clear throughout LETTERPRESS. However, the difficulty and time-consuming nature of physical security and manual review of data was also made very clear. And contrary to the comments on physical security and manual review, the immediate confirmation of cryptographic data was highlighted as a huge benefit to the inspectors.

At the end of LETTERPRESS, the importance and frustration of CoC was mentioned nearly unanimously by the players. In the context of the amount of information necessary for inspectors to achieve their objectives, this was a significant lesson. The LETTERPRESS team explored the balance between how much data is enough to have confidence but not overwhelm the inspectors and syphon precious time and resources away from the inspection to data review.

4. Lessons Learned

The impact of the lessons learned, and the experience gained will last well beyond LETTERPRESS. In conclusion, a few of the high-level and impactful lessons learned are provided here.

- The inspection objectives of confirming correctness and completeness are complementary. In the context of useful information and achieving inspection objectives, the combination of correctness and completeness may provide greater overall confidence while minimizing the amount of information required by the inspector or released by the host. Thinking of these as a system helped to identify key control points and allowed all parties to better understand the impact of any one action, decision, or activity on the host and inspector, and in the context of minimization of information.
- The technologies were instrumental in the success of LETTERPRESS. The implementation of the technologies within their defined roles were selected to trial various techniques and capabilities of interest to the Quad partners. Each technology also highlighted potential opportunities and challenges regarding its use in a verification regime similar to LETTERPRESS. One aspect that was left out of LETTERPRESS was equipment authentication. This was recognized as a key part of technology deployment but was not on the critical path with respect to Quad learning objectives for LETTERPRESS.
- The implementation of managed access within LETTERPRESS highlighted the challenges of performing verification activities at a treaty partner nuclear weapon facility. Host operation of all equipment and data, and the use of personal protective equipment (PPE) for inspectors, in conjunction with continuous escorting, within monitored areas highlight the scope of managed access in LETTERPRESS. These examples were implemented within LETTERPRESS to evaluate the impact of managed access and information protection without the need to focus ont guards, gates and guns. Output from LETTERPRESS made it clear that managed access has a big impact on both inspector and host in positive and negative ways.
- LETTERPRESS highlighted technical and policy implications stemming from decisions made during the exercise/simulation regime development effort. Technical solutions require certain information to be successful. This information may directly impact policy decisions regarding the quality and quantity of information that may need

to be released regarding a country's nuclear stockpile and weapon characteristics. The regime development process must be considered from a system point of view to capture the cost-benefit analysis and achieve the desired balance between verification and information protection.

5. References

[1] UKNI Collaboration; *The United Kingdom – Norway Initiative on the Verification of Nuclear Warhead Dismantlement;* UKNI Presentation, NPT PrepCom; Vienna, May 2012. https://assets.publishing.service.gov.uk/government/uploads/system/uploads/attachment_data/file/28425/20120503_npt_prepcom_presentation.pdf.

[2] NNSA Office of Nonproliferation and Arms Control, UK Atomic Weapons Establishment; *Joint U.S. – U.K. Report on Technical Cooperation for Arms Control;* https://www.energy.gov/sites/prod/files/2017/10/f37/Joint_USUK_Report_FINAL%5B1%5D.PDF; May 2015.

[3] Hinderstein, C; *International Partnership for Nuclear Disarmament Verification: A foundation for future arms reductions*; Bulletin of the Atomic Scientists 74(5), 2018.

[4] Treaty on the Non-Proliferation of Nuclear Weapons (NPT), https://www.un.org/disarmament/wmd/nuclear/npt/text. Accessed May 1, 2019.

[5] U.S. Department of State; *New START;* https://www.state.gov/t/avc/newstart/; Accessed May 1, 2019.

KJ-BB-19-058-EN-N